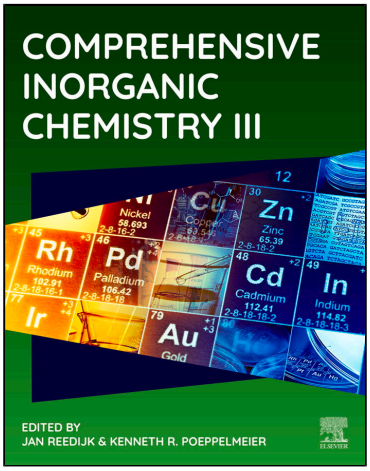

Li, G.; Pidko, E. A. Metal containing nanoclusters in zeolites. In *Heterogeneous Inorganic Catalysis;* van Santen, R. A.; Hensen, E.; in Comprehensive Inorganic Chemistry III; Reedijk, J., Poeppelmeier, K. R., Eds.; Vol. 6, pp 112– 147. Oxford: Elsevier. ©2023 Elsevier Ltd. ISBN 9780128231531. DOI: B978-0-12-823144-9.00022-4.
ISBN: 9780128231449

6.06 Metal containing nanoclusters in zeolites

Guanna Li[a,b] **and Evgeny A. Pidko**[c], [a] Biobased Chemistry and Technology, Wageningen University & Research, Wageningen, The Netherlands; [b] Laboratory of Organic Chemistry, Wageningen University & Research, Wageningen, The Netherlands; and [c] Inorganic Systems Engineering group, Department of Chemical Engineering, Faculty of Applied Sciences, Delft University of Technology, Delft, The Netherlands

6.06.1	**Introduction**	**112**
6.06.2	**Synthesis**	**113**
6.06.2.1	Encapsulation of nanoclusters in zeolite	113
6.06.2.2	Isolated single metal atom sites in zeolites	117
6.06.3	**Advanced characterization techniques for zeolite encapsulated metal species**	**120**
6.06.3.1	Electron microscopy	121
6.06.3.2	X-ray absorption spectroscopy	122
6.06.3.3	Vibrational spectroscopy	126
6.06.3.4	Solid-state nuclear magnetic resonance	129
6.06.4	**Catalytic applications**	**131**
6.06.4.1	C1 molecules conversion	131
6.06.4.2	Active site cooperation and multifunctionality in confined space	132
6.06.4.3	Confined space for selectivity control	135
6.06.5	**Computational modeling**	**136**
6.06.5.1	Structure prediction by operando thermodynamic analysis	136
6.06.5.2	Reactivity scaling relationship and beyond	136
6.06.5.3	Micro-kinetic modeling and dynamics	139
6.06.6	**Conclusion and perspective**	**141**
Acknowledgment		**141**
References		**141**

Abstract

The molecular-sized void space of the zeolitic micropores is perfect matrices to encapsulate and stabilize multicomponent and multifunctional complexes that can be used as active sites for a wide range of important catalytic transformations. In this article, we discuss and analyze the key developments of the last decade in the catalytic chemistry of metal-containing nanoclusters confined in zeolite micropores. We will present a concise summary of the recent developments in the tailored synthesis strategies, the advanced in-situ and operando characterization techniques, the enhanced performances of zeolite stabilized nanoclusters in various catalytic processes, and the application of computational modeling approaches for addressing the puzzle of catalyst-reactivity relationships. The article will be concluded with a brief discussion on the perspective for future developments anticipated for this field.

6.06.1 Introduction

Zeolites are a versatile class of inorganic microporous materials with a wide range of research and industrial applications in catalysis, ion-exchange, adsorption, and separation technology. In modern catalysis, zeolites represent one of the most important groups of robust supports and solid catalysts for a wide range of industrial catalytic processes, due to their unique physiochemical properties that persist under harsh reaction conditions (acidic or basic system, high temperature, and pressure) and the high flexibility of finely tunable functionalities by the target-driven design of their textural and chemical characteristics. The widespread application and the central position of zeolites in the field of heterogeneous catalysis attribute not only to their microporous structures contributing to the unique shape selectivity but also to the possibility of introducing and manipulating the active components confined within the micropores contributing thus with the nanoconfinement, cooperativity and unique electronic effects as the additional reactivity gears to tailor the activity and selectivity of the resulting composite catalysts.[1] The molecular-sized void space of the zeolitic micropores are particularly suitable to encapsulate and stabilize multicomponent and multifunctional complexes[2,3] that can be used as the active sites for a wide range of important catalytic transformations such as selective biomass conversion,[4,5] valorization of natural gas[6–8] and CO_2[9] recycling as well as petrochemical conversion[10] and selective catalytic reduction of NO_x.[11,12]

In this article, we discuss and analyze the key developments of the last decade in the catalytic chemistry of metal-containing nanoclusters confined in zeolite micropores. We will present a concise summary of the recent developments in the tailored synthesis

Comprehensive Inorganic Chemistry III, Third Edition, 2023, 112–147

strategies, the advanced in-situ and operando characterization techniques, the enhanced performances of zeolite stabilized nanoclusters in various catalytic processes, and the application of computational modeling approaches for addressing the puzzle of catalyst-performance relationships. The article will be concluded with a brief discussion on the perspective for future developments anticipated for this field.

6.06.2 Synthesis

Zeolites are three-dimensional microporous crystalline materials assembled by corned-shared tetrahedral TO_4 building blocks, with T atoms usually being Si or Al. A large variety of zeolite structures can be synthesized by tuning the synthesis parameters such as the composition of the precursors, the types of the structure-directing agents, or the crystallization conditions. The micropores of the resulting solids can be used to encapsulate isolated metal sites, nanoclusters, and nanoparticles in local micro-environments with nanoconfinement effects.[13] The size of the encapsulated species is one of the crucial factors governing their distinct chemical properties and catalytic performance (Fig. 1). A reduction of the size usually contributes to a higher reactivity due to the increase of the fraction of the coordination-unsaturated metal sites in smaller metal entities. Furthermore, due to the quantum size effects, subtle changes in the size or geometry of a molecular- or nanosized cluster can give rise to substantial changes in their physicochemical characteristics and, accordingly, their catalytic reactivity.[14–17] Therefore, much effort has been put into the improved control over the formation of cluster species inside the zeolite micropores. Below, we review the state-of-the-art synthesis strategies for encapsulating metal-containing nanoclusters and even single atom sites inside the zeolite matrices.

6.06.2.1 Encapsulation of nanoclusters in zeolite

Small metal particles often show high activity in many types of reactions due to the coordination-unsaturated metal centers, high facet exposure, and large surface-to-volume ratios. However, one of the biggest challenges is the low stability of ultra-small metal clusters and particles. Due to the high surface energy, they tend to aggregate into big nanoparticles (>5 nm) when dispersed on open surfaces, resulting in decreased catalytic activity.[18,19] The formation and stabilization of the metal nanoparticles inside the zeolite microspores is one of the practical solutions to circumvent such aggregation process. Furthermore, the zeolite encapsulation strategy allows the tailored formation of multifunctional reactive environments with uniquely tunable catalytic properties. The rigid and robust zeolite framework provides the unique stabilizing micro-environment that not only prevents sintering of the metal nanoclusters but also defines their size, shape, and electronic properties.[20–22]

Post synthetic protocols such as ion-exchange, impregnation, and chemical vapor deposition have been widely applied to encapsulate metal clusters within large pores of the zeolite crystals. The ion-exchange method is one of the most widely used approaches to incorporate metal species into the zeolites with controlled exchange numbers. In this method, the proton or alkali metal cations compensating the framework charge imbalance induced by lattice Al sites in the parent material are being replaced by other metal species through the ion-exchange reaction in an aqueous solution. However, in practice, these conventional techniques often give rise to heterogeneous metal speciation with the metal being deposited both in the micropores and on the external surface of the zeolite crystals. Post-synthetic reduction or calcination treatments are usually used to mobilize the deposited species and facilitate their diffusion to the extraframework sites inside the zeolite channels. Such common strategies have been widely used in zeolite chemistry and catalysis to prepare materials containing extraframework species such as Ga, Fe, Mo, etc. By redox treatment, the

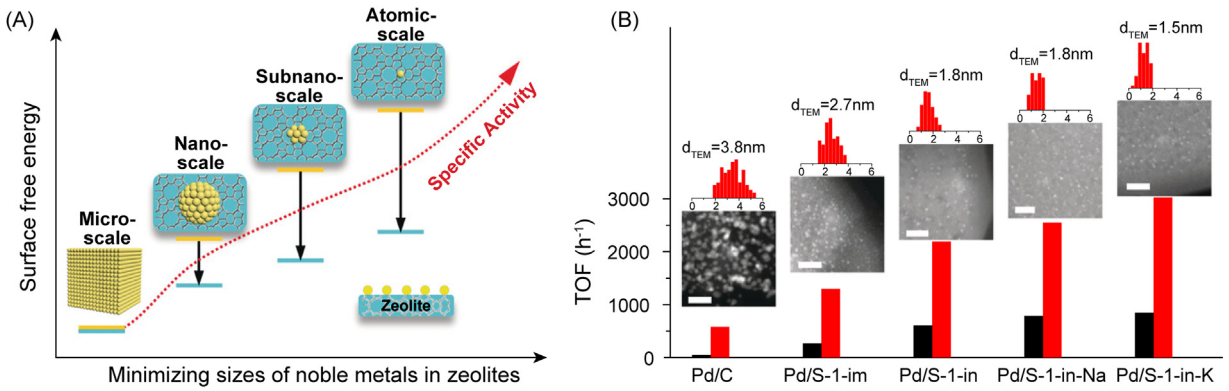

Fig. 1 Noble metal particle size effect in zeolite catalysis. (A) The change of surface free energy and specific activity with the size of noble metal particles on the zeolite support; (B) The comparison of TOF values of H_2 formation upon the dehydrogenation of formic acid–sodium formate (1:1) at 25 °C (black) and 50 °C (red) with Pd nanoparticles of different average size on either carbon (Pd/C) or S-1 zeolite (Pd/S-1) (im = impregnation, in = in situ encapsulation). Insets present the TEM images and corresponding size distributions of Pd clusters (scale bars: 20 nm). Adopted with permission from Wu, S.-M.; Yang, X.-Y.; Janiak, C. Confinement Effects in Zeolite-Confined Noble Metals. *Angew. Chem. Int. Ed.* **2019**, *58*(36), 12340–12354. Copyright 2019, Wiley.

transition metal species can give rise to various oxide, sulfide, and carbide clusters. Integrated strategies for engineering such metal-oxo, metal-sulfide, and metal-carbide nanoclusters in zeolite matrices have been recently reviewed by Kosinov et al. in Ref. 23. However, for small-pore zeolites, these methods often show low efficiency because of the limited accessibility of the narrowed channels by the solvated or gaseous metal precursors. Moreover, the ion-exchange and impregnation in aqueous solutions may give rise to heterogenous particle size distribution and poor catalytic activity. In the text below we will rather focus on alternative and modified strategies that allow for improved control of cluster speciation.

Several new strategies combining the conventional ion-exchange or impregnation approaches with more advanced synthetic methodologies have been introduced for the synthesis of complex inorganic architectures confined in the zeolite pores. Zhang et al. combined the ion-exchange with the layer reassembling process to encapsulate metal nanoclusters in zeolites.[24] The flexible distance of the layered zeolite intermediates offers opportunities for the direct introduction of metal precursors during the zeolite synthesis. This approach has been used to selectively introduce Pd particles in the FER zeolite matrix. First, FER layers were swelled into their layered precursors with the aid of cetyltrimethylammonium (CTA^+) surfactant. Then, the CTA^+ cations were exchanged by Pd precursors. The topotactic transformation from the layered precursor to the 3-dimensional FER framework resulted in the effective encapsulation of the metal species, which were transformed to well-defined Pd clusters of ca. 1.4 nm by subsequent calcination and reduction treatments. Román-Leshkov and co-workers combined ion-exchange with selective demetalation to prepare bimetallic nanoclusters within the micropores of MFI zeolite.[25] Zn-containing MFI zeolite (Zn-MFI) was firstly synthesized by the hydrothermal method. Then Pd^{2+} ions were introduced into the pores by ion-exchange to form Pd@Zn-MFI, taking the advantages of the charge imbalance of the Zn-containing framework. Finally, by temperature-programmed calcination and reduction treatments, the $PdZn_x$ bimetallic nanoclusters were generated within the MFI channels by alloying of Pd with Zn ions extracted from the framework. The procedure yielded bimetallic $PdZn_x$ nanoclusters of ca. 1 nm highly active in selective hydrogenation of halogenated nitroarenes. Moliner et al. complemented the incipient wetness impregnation with the atom-trapping technique (**Scheme 1**) to prepare

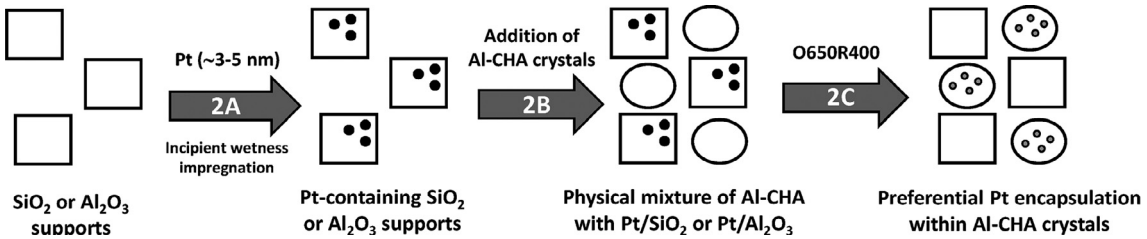

Scheme 1 Atom-trapping methodology when the Al—CHA is mixed with a Pt-containing SiO_2 or Al_2O_3 support. Reproduced with permission from Moliner, M.; Gabay, J.; Kliewer, C.; Serna, P.; Corma, A., Trapping of Metal Atoms and Metal Clusters by Chabazite under Severe Redox Stress. *ACS Catal.* **2018**, *8*(10), 9520–9528. Copyright 2018, American Chemical Society.

a series of sintering-resistant Pt, Pd, and bimetallic Pt—Pd nanoparticles inside non-reducible Al-containing CHA zeolite. The method involves the selective transfer of weakly bound MO_x precursors from open SiO_2 or Al_2O_3 supports into the zeolite channels upon treatment at 650 °C in the O_2 atmosphere. The high affinity of Al-containing CHA zeolite to trap and stabilize noble single-metal atoms and metal clusters is the driving force for this process.[26]

The direct encapsulation of metal precursors during the hydrothermal zeolite synthesis is a promising strategy for the modification of small-pore zeolites and to improve the particle size distribution. In this method, the zeolite framework is assembled around the metal precursors. Unfortunately, this promising methodology fails often when applied to common transition metal precursors, because of their rapid precipitation asynchronous with the slow hydrothermal zeolite crystallization under the highly basic synthesis conditions. To overcome this problem, Iglesia and co-workers developed a general and versatile synthetic strategy using bifunctional organosilane ligands that enabled encapsulation of different metal clusters (Pt, Pd, Ir, Rh, and Ag) within the small pores of NaA zeolite. Modification of this zeolite type could not be achieved by the post-synthetic approaches. The authors have shown that the bifunctional mercaptosilane protecting ligands prevent the metal precursors from the precipitation and promote the condensation of silicate structures around the ligated precursors (**Fig. 2**A).[27] This strategy was further expanded to other small-pore zeolites such as SOD and GIS.[28] Furthermore, the same group developed a robust low-temperature hydrothermal direct synthesis of MFI zeolites modified with uniform 1.3–1.7 nm Pt, Ru, and Rh nanoparticles via interzeolite transformation. In this method, the large-pore zeolites of BEA and FAU containing metal nanoparticles within their microporous voids are synthesized by the direct hydrothermal routes. Subsequent recrystallization of such parent zeolite precursors yields the modified MFI daughter material with a higher framework density without the loss of encapsulation (**Fig. 2**B). The interzeolite transformation involves the nucleation and crystallization of the MFI without using any organic structure-directing agents, which represents a potentially more economical and environmentally favorable route compared to the conventional procedures.[29] These methods require that the zeolite synthesis and encapsulation are carried out simultaneously under mild template-free crystallization conditions. As a result, they are normally used for the encapsulation of metal clusters into zeolites with a relatively low Si to Al ratio (Si/Al < 3) resulting in low hydrothermal stability of the resulting composites.

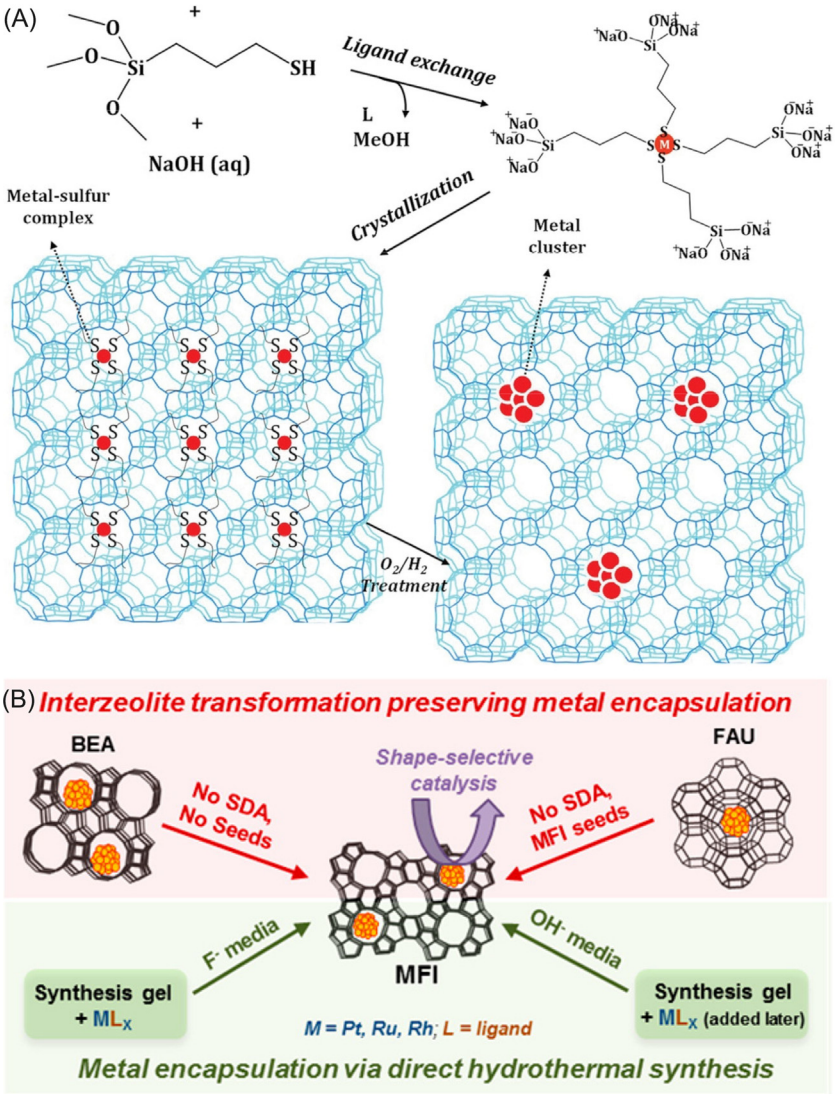

Fig. 2 (A) Schematic process for mercaptosilane-assisted metal encapsulation during zeolite crystallization. (B) Encapsulation of metal clusters within MFI by exchanging cationic metal precursors into a parent zeolite (BEA, FAU) and transforming these zeolites into daughter structures of higher framework density (MFI) under hydrothermal conditions. (A) Reproduced with permission from Choi, M.; Wu, Z.; Iglesia, E. Mercaptosilane-Assisted Synthesis of Metal Clusters within Zeolites and Catalytic Consequences of Encapsulation. *J. Am. Chem. Soc.* **2010**, *132*(26), 9129–9137. Copyright 2010, American Chemical Society. (B) Reproduced with permission from Goel, S.; Zones, S. I.; Iglesia, E. Encapsulation of Metal Clusters within MFI Via Interzeolite Transformations and Direct Hydrothermal Syntheses and Catalytic Consequences of their Confinement. *J. Am. Chem. Soc.* **2014**, *136*(43), 15280–15290. Copyright 2014, American Chemical Society.

To overcome this limit of low hydrothermal stability, new strategies were developed to encapsulate noble metals into high-silica zeolite matrices. Corma and co-workers reported a method for incorporating Pt metal clusters and single atoms in thermally stable high-silica zeolites. Purely siliceous layered MWW zeolite precursors were first prepared via the conventional hydrothermal route and expanded by the organic surfactant of hexadecyltrimethylammonium ($CTMAC^+OH^-$). Then, the sub-nanometer Pt species were introduced into the interlayer space. At the next step, the removal of the organic compounds and the formation of the 3D zeolite structure upon high-temperature calcination 540 °C yielded sub-nanometer-sized Pt clusters encapsulated in zeolite cages of the 3D MCM-22 (**Fig. 3**A and B).[30] More recently, the same group reported another approach to regioselectively encapsulate sub-nanometer Pt species into purely siliceous MFI zeolite by a one-pot synthesis strategy. The location of the Pt nanocluster was specified by limiting the access of the Pt species to the sinusoidal channels with the intersectional void occupied by the tetrapropylammonium hydroxide (TPA^+OH^-) template molecules.[31] A similar direct encapsulation approach was also employed to highly selectively deposit Ir clusters into the 10 membered rings connecting the two neighboring 12 membered ring supercages of the MWW zeolite.[32] Xu and co-workers developed a cationic polymer-assisted synthesis allowing the encapsulation of Pt nanoparticles into the micropores of both siliceous and aluminosilicate MFI zeolites.[33] Their method was based on the use of polydiallydimethylammonium chloride template, which limits the mobility of $PtCl_6^{2-}$ precursors and at the same time promotes the

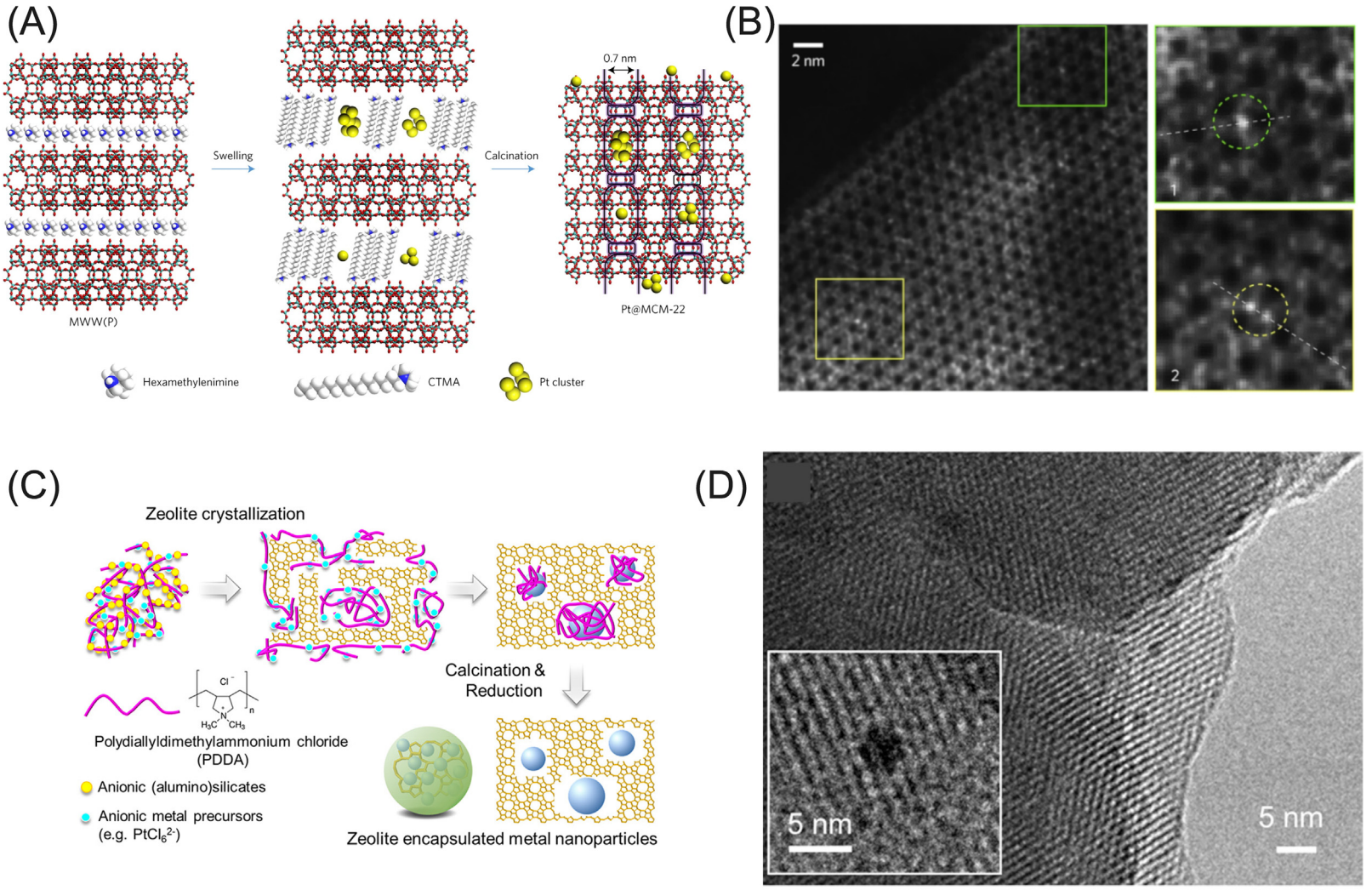

Fig. 3 (A) Encapsulation of Pt nanoclusters during the transformation of a 2D MWW zeolite precursors into daughter 3D MCM-22 structure. (B) HAADF-HRSTEM image of Pt@MCM-22. (C) Cationic polymer-assisted synthetic strategy to encapsulate Pt nanoclusters into MFI zeolite. (D) High-resolution TEM image of Pt@HZSM-5. (B) Reproduced with permission from Liu, L.; Diaz, U.; Arenal, R.; Agostini, G.; Concepcion, P.; Corma, A. Generation of Subnanometric Platinum with High Stability during Transformation of a 2D Zeolite into 3D. *Nat. Mater.* **2017**, *16*(1), 132–138. Copyright 2017, Springer Nature. (D) Reproduced with permission from Cho, H. J.; Kim, D.; Li, J.; Su, D.; Xu, B. Zeolite-Encapsulated Pt Nanoparticles for Tandem Catalysis. *J. Am. Chem. Soc.* **2018**, *140*(41), 13514–13520. Copyright 2018, American Chemical Society.

encapsulation of metal precursors during zeolite crystallization in an alkaline environment. The driving force for the selective encapsulation is the electrostatic interactions with both the anionic metal precursor and the silicate or aluminosilicate building blocks of the zeolites in the synthesis gel (Fig. 3C and D).

Yu et al. developed a facile and direct hydrothermal approach and prepared ultrasmall Pd nanoclusters with a uniform particle size ca. 1.8 nm well dispersed at the channel intersections of the MFI structure. The nanoclusters were encapsulated by in-situ confinement within nanosized silicalite-1 (S-1) zeolite using $[Pd\text{-}(NH_2CH_2CH_2NH_2)_2]Cl_2$ as a metal precursor and TPA^+OH^- as a template. The preferential localization of the TPA^+ template ions in the middle of the straight channel resulted in the selective deposition of the Pd nanoclusters at the intersection sites. Such a selective encapsulation of nanoparticles resulted in their enhanced resistance to sintering and stability toward high-temperature redox and hydrothermal treatments.[34] Later, the same group also successfully synthesized ultra-small bimetallic $Pd{-}M(OH)_2$ (M = Ni, Co) clusters encapsulated within purely siliceous zeolites with superior thermal stability and high activity for formic acid dehydrogenation.[35] Subnanometer bimetallic PtZn cluster was also confined into the micropores of S-1 zeolite by the similar direct hydrothermal crystallization. The introduction of Zn remarkably improved the stability of confined Pt clusters. The resulting PtZn@S-1 catalyst exhibited excellent activity and selectivity in the propane dehydrogenation reaction.[36] Zhu et al. reported the ultrafast in-situ encapsulation of metal nanoclusters into MFI zeolite during its crystallization. With this method, Pt@Sn-MFI materials were synthesized within just 5 min. The ultrafast route for zeolite synthesis allows circumventing the mismatch in the time-scales of the precipitation of metal nanoclusters and the crystallization of zeolite matrix (Fig. 4).[37]

Xiao's group developed another generic solvent-free strategy by mixing, grinding, and heating solid raw materials to synthesize bimetallic AuPd nanoparticles within the micropore of S-1 zeolite showing a very high efficiency of noble metal utilization. This method is viewed as a greener and more environmentally benign alternative to the conventional hydrothermal methods as it simultaneously eliminates the need of the organic templates and water solvent during the synthesis as well as the subsequent high-temperature calcination step commonly required to remove the template molecules from the zeolite pores. (Fig. 5A).[38] The metal nanoparticles are immobilized onto amorphous silica, which is then crystallized into a zeolite framework in the solid phase. The efficiency and yield of the zeolite product are remarkably enhanced by such a simple synthesis protocol.[39–42] It is shown that more than 96% of gold and palladium could be successfully loaded into the zeolite, which is much higher than the 36% encapsulation efficiency obtained in the hydrothermal process. Catalytic test revealed a high activity, selectivity, and stability of Au-Pd@S-1 catalyst in the aerobic oxidation of bioethanol even in the presence of 90% water.[43] This solvent-free method was later expanded to the encapsulation of monometallic Pd nanoparticles in S-1. The thus formed Pd@S-1 material catalyzes furfural hydrodeoxygenation with furan selectivity of 99% at 91% conversion, which is superior to the values obtained with the conventionally prepared supported Pd/S-1 catalyst.[44]

The same group reported a seed-directed organic template-free synthesis route toward Pd@BEA materials. The Pd nanoparticles supported on BEA zeolite nanocrystals function as zeolite seeds in the synthesis gel for the growth of new BEA zeolite crystals so that the Pd nanoparticles were encapsulated inside the extended BEA zeolite structure (Pd@BEA).[45,46] The crystallization process effectively controls the size and stability of the metal nanoclusters. During the synthesis, an amorphous aluminosilicate gel covers and protects the metal nanoparticles deposited on the zeolite seeds. This results in a crystalline zeolite sheath that prevents sintering and stabilizes the nanoparticles even during catalytic operation under severe conditions (Fig. 5B–J).[47] The sizes of the metal nanoparticles in the final metal@zeolite catalysts can be adjusted by fine tuning the particle size in the initial seed precursor. Such a method was generalized to synthesize a variety of transition metal-loaded silica and aluminosilicate zeolite catalysts such as Pd@S-1, Pt@BEA, Pt@MOR, Rh@BEA, Rh@MOR, Ag@BEA, Ag@MOR, and Pt@Fe-BEA.[46,47] An analogous seed-directed solvent-free method was also employed for the encapsulation of Au nanoclusters in TS-1 zeolite. The encapsulated Au nanoparticles are anchored at the framework Ti sites resulting in the Au–Ti synergy.[48]

6.06.2.2 Isolated single metal atom sites in zeolites

Single metal atom catalysis has been emerging as a new frontier in catalysis science and technology since 2011.[49–51] Theoretically, isolated single-atom site (SAS) catalysts have the maximum atom-utilization efficiency and offer uniquely tunable catalytic properties combining the benefits of both heterogeneous and homogeneous catalysis. Therefore, the selective generation of SASs with high activity and stability is of great importance from the academic and industrial points of view.[52] Besides, SASs can be used as the ideal model systems for the investigation of the structure-activity relationships of various practical catalytic systems.[7,53,54] Stabilization of the active phase in the single-atom state and prevention of their agglomeration is one of the key challenges in the field.[55] The aggregation of the active metal sites into bulk-like clusters or leaching into reaction solution decrease the recyclability and catalytic performance of such catalysts. Among different support materials, zeolites were identified as promising nano-containers for the stabilization of SASs. An important advantage over alternative support materials is the unique shape selectivity and defined multifunctional reaction environment provided by the zeolite channels encapsulating SASs.[56]

Pioneering works by Gates and co-workers have introduced the view on the zeolite framework as a macro-ligand providing defined donor sites with defined steric constraints and variable basicity capable of coordinating and stabilizing various transition metal species. Well-defined transition metal species have been incorporated into large-pore FAU-type Y zeolite via the formal ligand exchange reaction of the $M(L)_2(acac)_x$ (M = Rh,[57,58] Ru,[59] Ir,[60,61] Au,[62] L = CO, C_2H_4, CH_3, acac = acetylacetonate, and x = 1 or 2) precursors with the zeolite Brønsted acid sites.

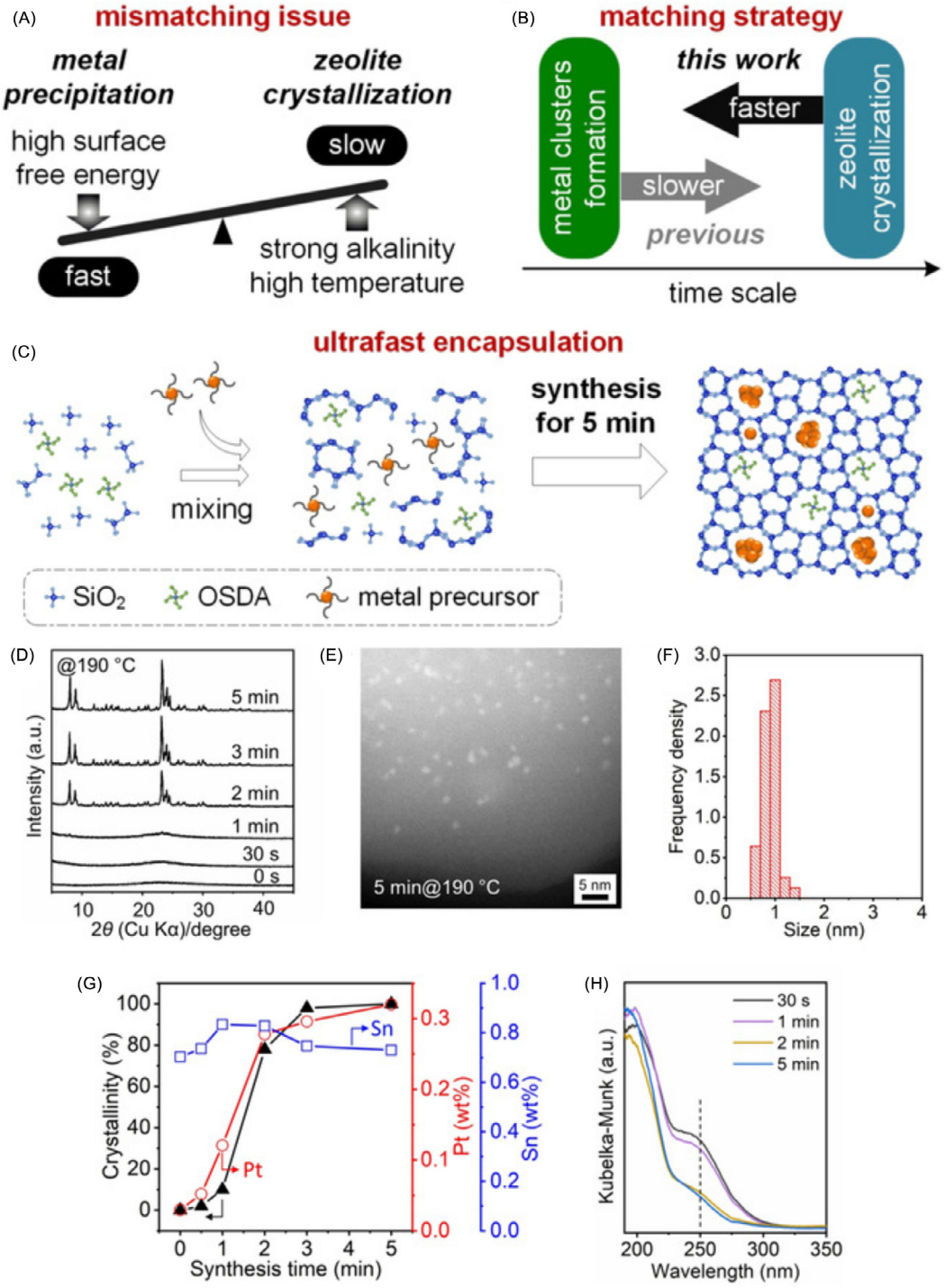

Fig. 4 (A) The mismatching between metal precipitation and zeolite crystallization. (B) The strategies for making metal precipitation and zeolite crystallization to match in time scale. (C) Scheme of the proposed ultrafast encapsulation. (D) X-ray diffraction patterns of the Pt@Sn-ZSM-5 samples synthesized at 190 °C for different times. (E) and (F) HAADF-STEM image and corresponding Pt/Sn particle size distribution of the Pt@Sn-ZSM-5 zeolite synthesized at 190 °C for 5 min. (G) Relative crystallinity and compositional evolution of the Pt@Sn-ZSM-5 samples synthesized over different periods. (H) UV–Vis spectra of the Pt@Sn-ZSM-5 samples synthesized over different times. Reproduced with permission from Zhu, J.; Osuga, R.; Ishikawa, R.; Shibata, N.; Ikuhara, Y.; Kondo, J. N.; Ogura, M.; Yu, J. H.; Wakihara, T.; Liu, Z. D.; Okubo, T. Ultrafast Encapsulation of Metal Nanoclusters into MFI Zeolite in the Course of its Crystallization: Catalytic Application for Propane Dehydrogenation. *Angew. Chem. Int. Ed.* **2020**, *59*, 19669–19674. Copyright 2020, Wiley.

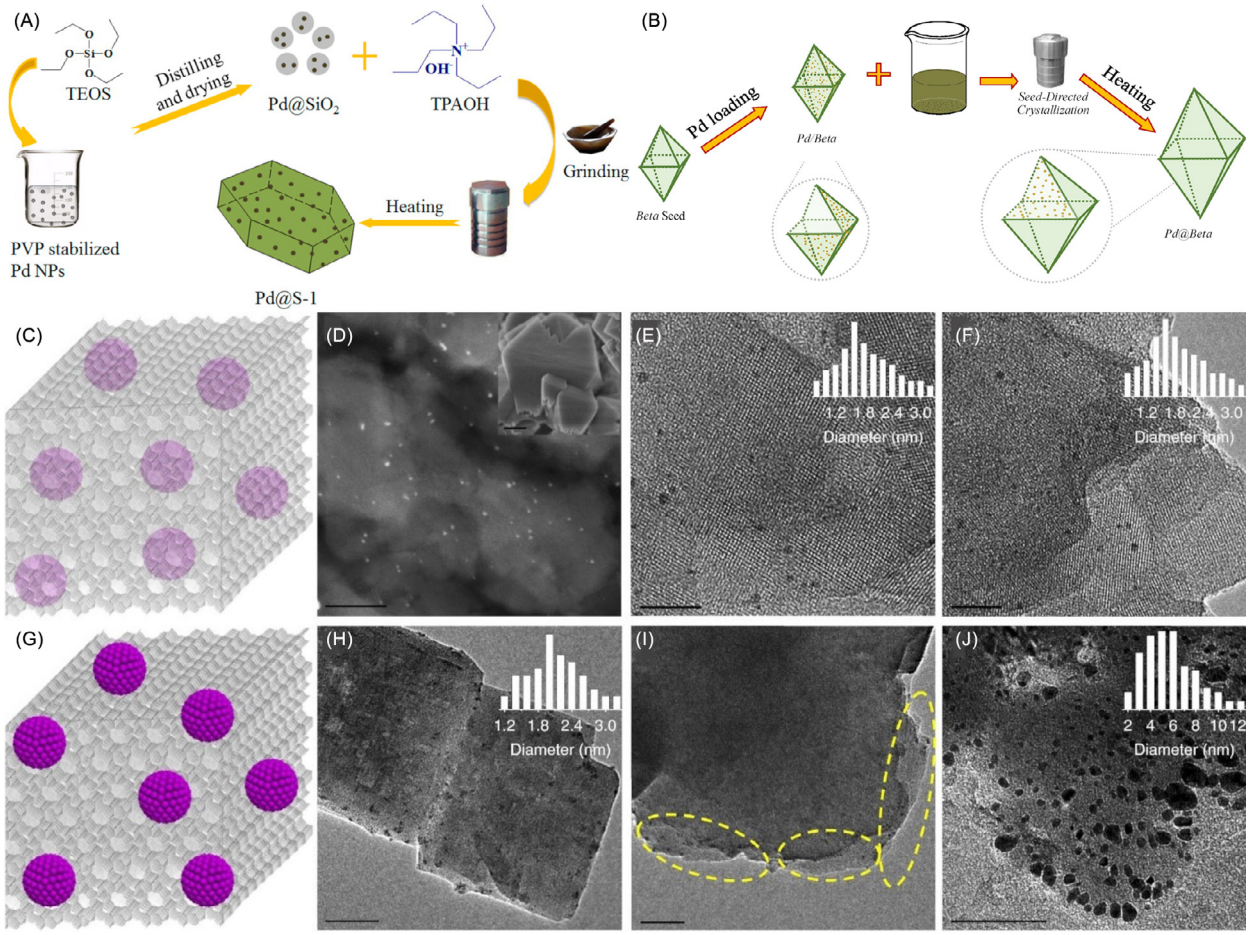

Fig. 5 (A) Synthesis of Pd@S-1 by solvent-free procedure. (B) Synthesis of Pd@Beta via the seed-directed route. (C) Proposed model, (D) STEM image, (E) HR-TEM, (F) tomographic image of Pt@BEA, (G) proposed model, (H) HR-TEM tomographic image of Pt@BEA after calcination at 600 °C for 240 min, (I) TEM tomographic image of Pt/BEA. (J) TEM image of Pt/BEA after calcination at 600 °C for 240 min. (A) Reproduced with permission from Wang, C.; Wang, L.; Zhang, J.; Wang, H.; Lewis, J. P.; Xiao, F.-S. Product Selectivity Controlled by Zeolite Crystals in Biomass Hydrogenation over a Palladium Catalyst. *J. Am. Chem. Soc.* **2016**, *138*(25), 7880–7883. Copyright 2016, American Chemical Society. (H) Reproduced with permission from Zhang, J.; Wang, L.; Zhang, B. S.; Zhao, H. S.; Kolb, U.; Zhu, Y. H.; Liu, L. M.; Han, Y.; Wang, G. X.; Wang, C. T.; Su, D. S.; Gates, B. C.; Xiao, F. S. Sinter-Resistant Metal Nanoparticle Catalysts Achieved by Immobilization Within Zeolite Crystals Via Seed-Directed Growth. *Nat. Catal.* **2018**, *1*(7), 540–546. Copyright 2018, Springer Nature.

More conventional catalyst synthesis methods such as aqueous ion-exchange and incipient wetness impregnation can also be used to introduce isolated SASs in zeolite matrices. For instance, Fe, Cu, Ni, Zn, Ga can be selectively exchanged into the six-membered rings of Beta, SSZ-13, CHA, and ZSM-5 zeolites.[6,63–66] Pt@LTL, Rh@ZSM-5, and InH_2@CHA zeolites with confined single metal sites were also fabricated by ion-exchange followed by oxidation or reduction treatment, which show significant reactivity for CO oxidation, methane transformation, and nonoxidative dehydrogenation of ethane, respectively.[67–69] The ion-exchange method is intrinsically limited by the ion-exchange capacity of the zeolite host and the solubility of the metal precursors. The impregnation appears therefore a more versatile technique for encapsulating metals in the zeolite matrices. Shan and co-workers employed incipient wetness impregnation (IWI) to synthesize isolated Rh sites in the zeolite of ZSM-5.[7] A similar approach was used for the selective synthesis of Pt(II)−$O(OH)_x$ single site in LTL and isolated WO_4 species entrapped in USY zeolite.[70,71] Yang and co-workers synthesized single site Au−$O(OH)_x$−(Na/K) mononuclear species inside the LTL zeolite by IWI followed by high-temperature calcination treatment.[72] The presence of alkali cations enhanced the stability of the supported Au species similar to the mechanism observed for other single-atom-type catalyst systems.[73,74] Such alkali-stabilized single Au sites exhibited catalytic activities similar to the more conventional ceria and titania-supported single-atom gold catalysts.

In analogy to nanoparticle encapsulation described in the previous section, the direct in situ immobilization of single metal atom sites during the zeolite synthesis has also been reported. Li and co-workers developed a general strategy to prepare zeolite Y-based catalysts containing such SASs as Pt, Pd, Ru, Rh, Co, Ni, and Cu.[75] Transition metal ethanediamine (EDA) complexes could be selectively dispersed among the β-cages of zeolite Y during the crystallization process. Subsequent thermal reduction treatment decomposes the confined M-EDA precursors and anchors the metal sites at the 6-membered rings making them accessible to reagents from the zeolite supercages (Fig. 6A).

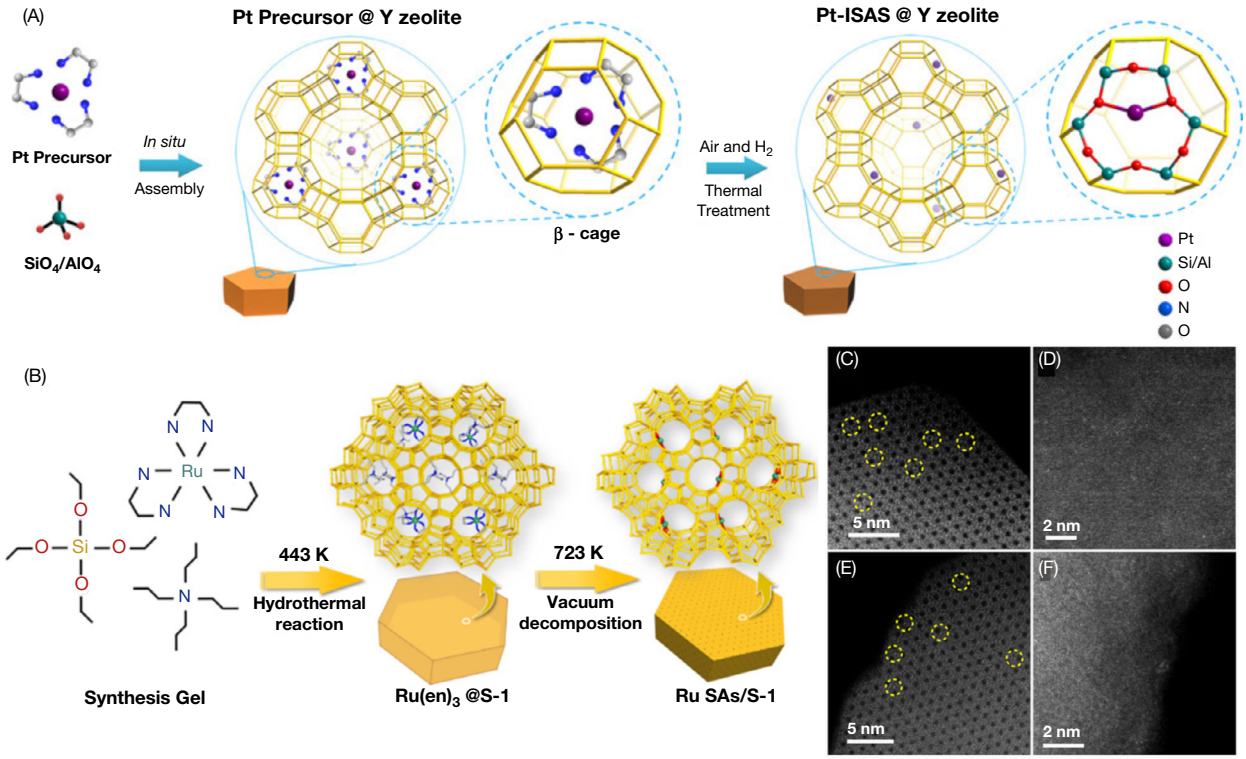

Fig. 6 (A) In situ separation and confinement of a platinum precursor in a β-cage of Y zeolite followed by thermal treatment. (B) Synthesis procedure of Ru single atom in S-1. (C and D) AC HAADF-STEM images of Ru SASs/S-1. (E and F) AC HAADF-STEM images of Ru SASs/S-1-used. Reproduced with permission from Liu, Y.; Li, Z.; Yu, Q.; Chen, Y.; Chai, Z.; Zhao, G.; Liu, S.; Cheong, W.-C.; Pan, Y.; Zhang, Q.; Gu, L.; Zheng, L.; Wang, Y.; Lu, Y.; Wang, D.; Chen, C.; Peng, Q.; Liu, Y.; Liu, L.; Chen, J.; Li, Y. A General Strategy for Fabricating Isolated Single Metal Atomic Site Catalysts in Y Zeolite. *J. Am. Chem. Soc.* **2019**, *141*(23), 9305–9311; Qiu, J. Z.; Hu, J. B.; Lan, J. G.; Wang, L. F.; Fu, G. Y.; Xiao, R. J.; Ge, B. H.; Jiang, J. X. Pure Siliceous Zeolite-Supported Ru Single-Atom Active Sites for Ammonia Synthesis. *Chem. Mater.* **2019**, *31*(22), 9413–9421. Copyright 2019, American Chemical Society.

Yu and co-workers encapsulated single Rh atoms within S-1 and aluminosilicate ZSM-5 zeolites by using one-pot hydrothermal synthesis followed by ligand-protected direct hydrogen reduction.[76] Purely siliceous S-1 supported Ru SASs were also successfully synthesized by the one-pot hydrothermal method. The mononuclear $[Ru(NH_2CH_2CH_2NH_2)_3]Cl_3$ metal precursor was successfully confined within the S-1 under hydrothermal zeolite synthesis conditions at 443 K. Subsequent vacuum treatment at 723 K for 12 h resulted in the removal of the organic structure-directing agents and ligands to generate Ru SASs inside the zeolite pores (Fig. 6B–F). The applicability of this methodology for the functionalization of other zeolite topologies with various noble metal SASs has been proposed.[77]

6.06.3 Advanced characterization techniques for zeolite encapsulated metal species

To confirm the successful encapsulation and the well-defined characteristics of the clusters and single-atom sites inside the zeolite pores, their comprehensive characterization is necessary. Most standard bulk characterization techniques fail to address the complexity of the metal-zeolite composite materials because of the relatively low metal concentration and intrinsic heterogeneity of the solid materials. To overcome the limitations of the individual techniques, the complementary use of several characterization tools such as electron microscopy, X-ray absorption spectroscopy, nuclear magnetic resonance (NMR), vibrational and UV–Vis spectroscopies aided by computational modeling is often practiced to identify the size, distribution, structure, and electronic properties of such active metal centers encapsulated inside zeolite materials. Such structural insights are also required to understand the mechanism of catalytic transformations by such materials and support the rational design and optimization of the zeolite-based catalysts. However, due to the structural flexibility, nanoclusters and single atom metal species can exhibit significant structural changes when interacting with reactants, complicating thus the determination of the active site structure under the catalyst working conditions. The combination of comprehensive ex-situ, in-situ, and operando characterization techniques provides insights into the physiochemical properties of metal-zeolite composites and helps to elucidate the structure-reactivity relationships to guide the engineering of superior zeolite catalyst.[78]

6.06.3.1 Electron microscopy

To determine the location and structure of the confined metal nanoparticles, high-angle annular dark-field (HAADF) scanning transmission electron microscopy (STEM) is typically used, which provides a high resolution and contrast between the heavy metal guest atoms and the light atoms of the zeolite framework. Gates and co-workers have pioneered the application of a damage-reduced aberration-corrected scanning transmission electron microscopy (STEM) in combination with infrared and extended X-ray absorption fine structure (EXAFS) spectroscopies to unravel the locations of the single metal atoms and small metal nanoclusters, such as Ir, Au, La, Os, Rh, inside zeolite micropores.[79–81] For instance, they identified the location and structure of hexairidium clusters confined in the NaY supercages by atomic-resolution (HAADF) aberration-corrected STEM with a high signal-to-noise ratio. The diameter of the cluster was precisely measured and the preferred locations of the Ir_6 cluster were identified (25%) (Fig. 7).[82]

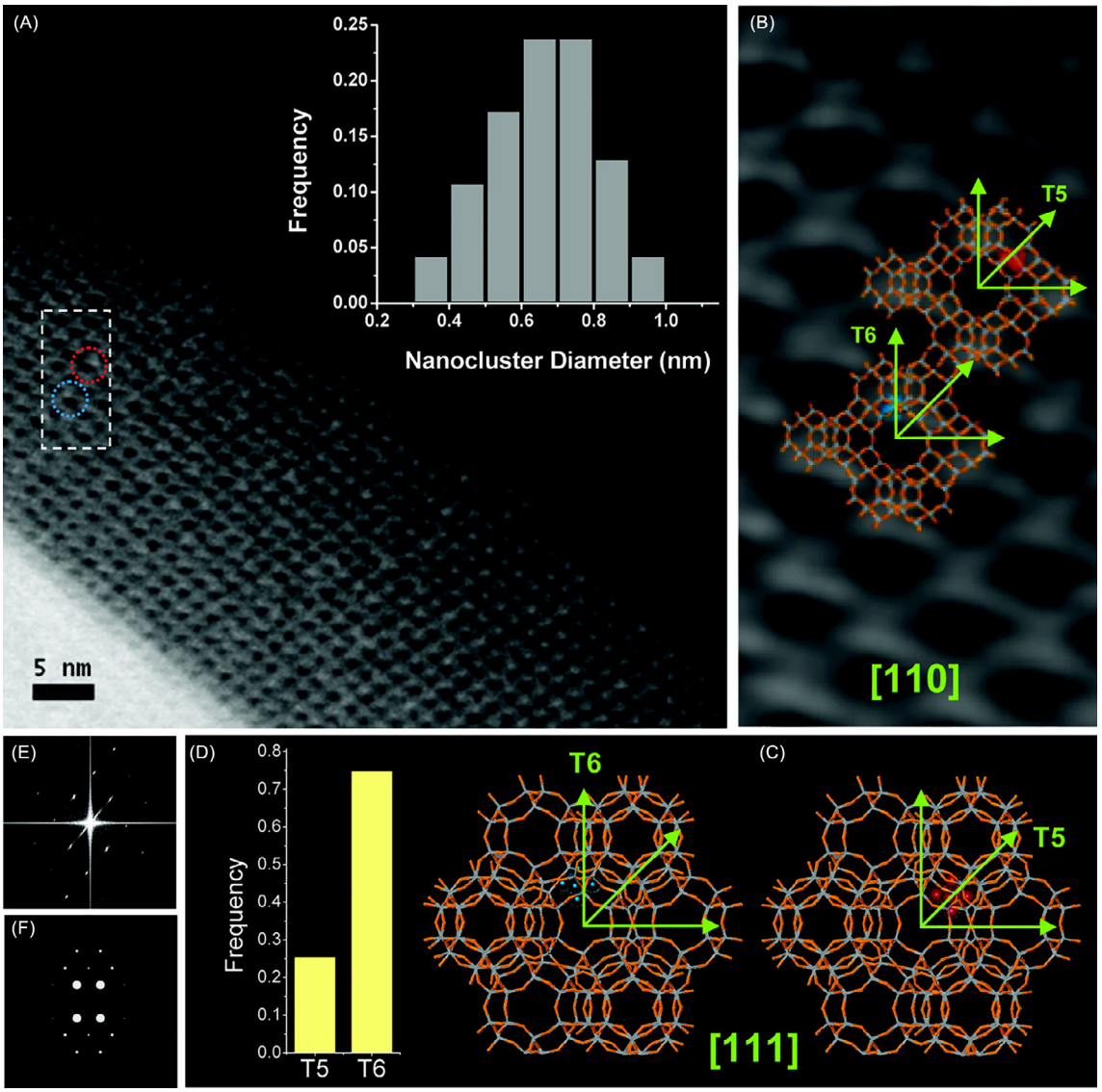

Fig. 7 (A) Unprocessed aberration-corrected HAADF-STEM image of zeolite NaY containing 10 wt% iridium after decarbonylation of clusters, showing the zeolite framework in the (110) direction, and a histogram showing the distribution of the nanocluster diameters. (B) A magnified view of the dashed-rectangular area in (A) containing the two Ir_6 clusters encircled. A cluster at a T5 site is represented in red, and a cluster at a T6 site is represented in blue. Simulations of the FAU in the (110) projection are superimposed on the experimental image indicating Ir_6 clusters. The arrows indicate the relative orientations of the T5 and T6 sites with respect to the (110) direction of the zeolite crystal. (C) Simulated FAU models in the (111) projection corresponding to the location of the two Ir_6 clusters shown in (B). (D) Frequencies of Ir_6 clusters located in T5 and T6 sites. (E) Fast Fourier transform of the experimental image shown in (A). (F) Theoretical diffraction pattern of zeolite NaY in the (110) direction. Reproduced with permission from Aydin, C.; Lu, J.; Shirai, M.; Browning, N. D.; Gates, B. C. Ir-6 Clusters Compartmentalized in the Supercages of Zeolite NaY: Direct Imaging of a Catalyst with Aberration-Corrected Scanning Transmission Electron Microscopy. *ACS Catal.* **2011**, 1(11), 1613–1620. Copyright 2011, American Chemical Society.

Furthermore, the aggregation of the isolated Ir atoms into nanoclusters in the 14-ring channels of zeolite SSZ-13 was also tracked and directly visualized. The authors proposed the autocatalytic agglomeration and sintering mechanism based on the electron microscopy data (Fig. 7).[83] The location of the mononuclear gold complexes in the zeolite pores was also confirmed by the same technique. These gold species were identified to be the catalytic active sites for CO oxidation at 298 K and 1 bar.[62] The presence of oxygen-bridged La pairs with La−La distance of ca. 3.84 Å in zeolite Y cages was observed consistent with the proposal based on X-ray photoelectron spectroscopy[81] and earlier periodic DFT studies.[84]

STEM was also used to identify the location and structure of other metal clusters such as Ag, Cd, and Zn in different zeolites.[85–89] Both light alkali cations and ion-exchanged rare earth metals (Eu, Tb, and Gd) could be unambiguously detected by aberration-corrected STEM with atomic resolution, providing unique information about the structure and location of both metal and zeolite support.[90] Very recently, Mayoral and co-workers reported the atomic-level observations of all framework atoms including heteroatom Fe and extraframework Na cations by spherical aberration-corrected STEM coupled with annular dark field (ADF) and annular bright-field (ABF) image modes, which have brought the sensitivity to single heteroatoms or point defects with extremely low density (Fig. 8).[91] Corma et al. developed a strategy to characterize precisely the location of sub-nanometer Pt and Sn species in MFI zeolite by STEM technique that records simultaneously the high-angle annular dark-field (HAADF) images for heavy metals and integrated differential phase-contrast (iDPC) images for the zeolite framework in the same area.[92,93] By combining with other spectroscopies this approach could provide essential information about the spatial distribution of the metal species encapsulated in zeolites and also reveal the locations of framework Al sites. Such newly developed technique has been successfully applied to in-situ imaging with atomic resolution of the structural changes of the zeolite framework induced by adsorption of aromatic molecules.[94] TEM tomography was also developed to provide 3-dimensional quantitative descriptions of the size, distribution, and interparticle distance of the metal particles within individual zeolite crystals.[19,95,96] For instance, Pt nanoclusters as small as 1 nm can be visualized by electron tomography and image analysis.[19]

6.06.3.2 X-ray absorption spectroscopy

Synchrotron X-ray absorption spectroscopy (XAS) is a powerful and widely used characterization technique to study the structure and electronic properties of zeolite-supported metal catalysts both ex-situ and under catalytic working conditions. There are two spectral regions that carry different kinds of information. The X-ray absorption near-edge structure (XANES) provides an insight into the electronic structure and oxidation state of the metal atoms. The processed data from extended X-ray absorption fine structure (EXAFS) contains information about the local environment of the elements of interest, e.g. the bond distances and coordination numbers of metal centers within the zeolite. The recent developments of in situ/operando XAS techniques were instrumental in unraveling the dynamics and structural flexibility of intrazeolite clusters under realistic conditions of catalytic reactions.

The oxidation state of Cu species during methane oxidation to methanol was characterized by Sushkevich et al. by a combination of in situ XAS and Fourier transform infrared spectroscopy (FTIR) of adsorbed probe molecules over Cu@MOR catalyst (Fig. 9).[97] The activated catalyst was dominated by Cu species with an oxidation state +2 as revealed by XANES. Upon reaction with methane, up to 70% of these Cu^{II} species were gradually reduced to a Cu^{I} state with simultaneous production of the oxygenated surface intermediates. The reaction with methane was followed by the introduction of steam into the reactor to extract the methanol product. This treatment resulted in the decrease of the peak due to Cu^{I} with a concomitant increase of the Cu^{II} signals in the spectrum. The interconversion of Cu^{I} and Cu^{II} species was also confirmed by FTIR using CO and NO as molecular probes.

The speciation of Cu clusters in SSZ-13 zeolite has been intensively studied by XAS.[63,98–101] Cu/SSZ-13 has been industrialized for the selective catalytic reduction (SCR) of NO_x with NH_3. However, the nature and composition of Cu species are still not fully understood. Many spectroscopic studies have been devoted to the problem of the nature and speciation of Cu sites in these catalysts with several excellent reviews on the subject published in recent years.[11,102–104]

The complexity of the structural problem of catalysis by confined transition metal clusters in zeolites can be well illustrated by the recent studies by Paolucci et al.[104] A comprehensive study of the active site speciation and evolution under the catalytic conditions has been carried out by a combination of site-sensitive experimental characterization (ex-situ, in-situ, and operando XAS) and computational modeling (density functional theory (DFT), ab initio free energy and molecular dynamics).[63] Two distinct structures were identified, namely, Cu^{2+} and $(CuOH)^{+}$ charge-balanced by the lattice Al sites of the zeolite framework. It was shown that H_2O solvation at ambient or NH_3 solvation under the SCR reaction condition can liberate the Cu species from the initial binding sites and induce their dynamic behavior and self-organization inside the zeolite pores.[105] It was demonstrated that the isolated Cu ions solvated by NH_3 ($Cu^{I}(NH_3)_2$) can diffuse from one cage to the adjacent cage far away from the charge compensated Al center via the 8-membered ring window. The resulting binuclear complex promotes the O_2 activation. Such dynamic paring process is revisable and the catalytic cycle is closed by the subsequent reduction of Cu^{II} by NO and NH_3 to produce N_2, H_2O, and regenerate $Cu^{I}(NH_3)_2$.[98] A similar Cu site dynamics was observed by Dinh and co-workers during continuous partial oxidation of methane to methanol.[106] Based on the kinetic and in situ spectroscopy studies, the authors proposed the binuclear $(Cu_2O)^{2+}$ clusters, formed by the diffusion of hydrated Cu ions along a proton-paved highway, as the major active site for selective oxidation of methane to methanol. Such active site migration can be blocked by the introduction of NH_3, which strongly binds with both the zeolitic protons and Cu ions. It was found that the optimal conditions for the catalytic reaction and the formation of such transient dimeric Cu moieties combine the high CH_4 and water partial pressures and high density of Brønsted acid sites on the framework of zeolite

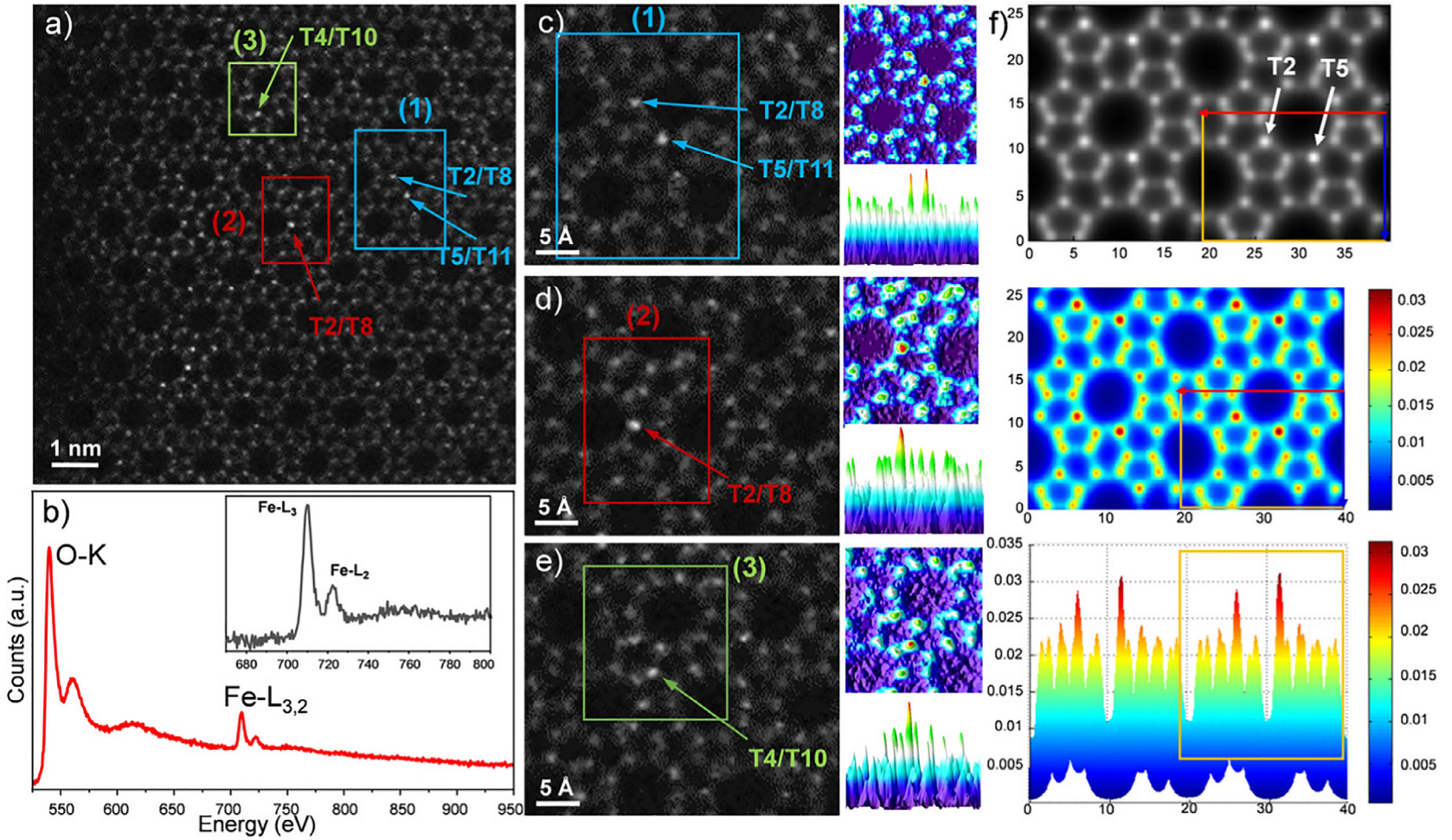

Fig. 8 Cs-corrected STEM ADF images and EEL spectrum of Fe-MFI. (A) High-resolution ADF image. (B) EEL spectrum. (C–E) Enlarged images corresponding to the three regions marked by rectangles in (A) together with surface plots of 2D-intensity distribution map, where bright dots in (A), (C), (D), and (E) are marked by arrows with T-site symbols. (F) Simulated images of Fe-MFI, where two single Fe atoms are located at T2 and T5 sites corresponding to two Fe atoms per unit cell, under the conditions of probe size: 1.0 Å and specimen thickness: 105 Å. Reproduced with permission from Mayoral, A.; Zhang, Q.; Zhou, Y.; Chen, P.; Ma, Y.; Monji, T.; Losch, P.; Schmidt, W.; Schüth, F.; Hirao, H.; Yu, J.; Terasaki, O. Direct Atomic-Level Imaging of Zeolites: Oxygen, Sodium in Na-LTA and Iron in Fe-MFI. *Angew. Chem. Int. Ed.* **2020**, *59*(44), 19510–19517. Copyright 2020, Wiley.

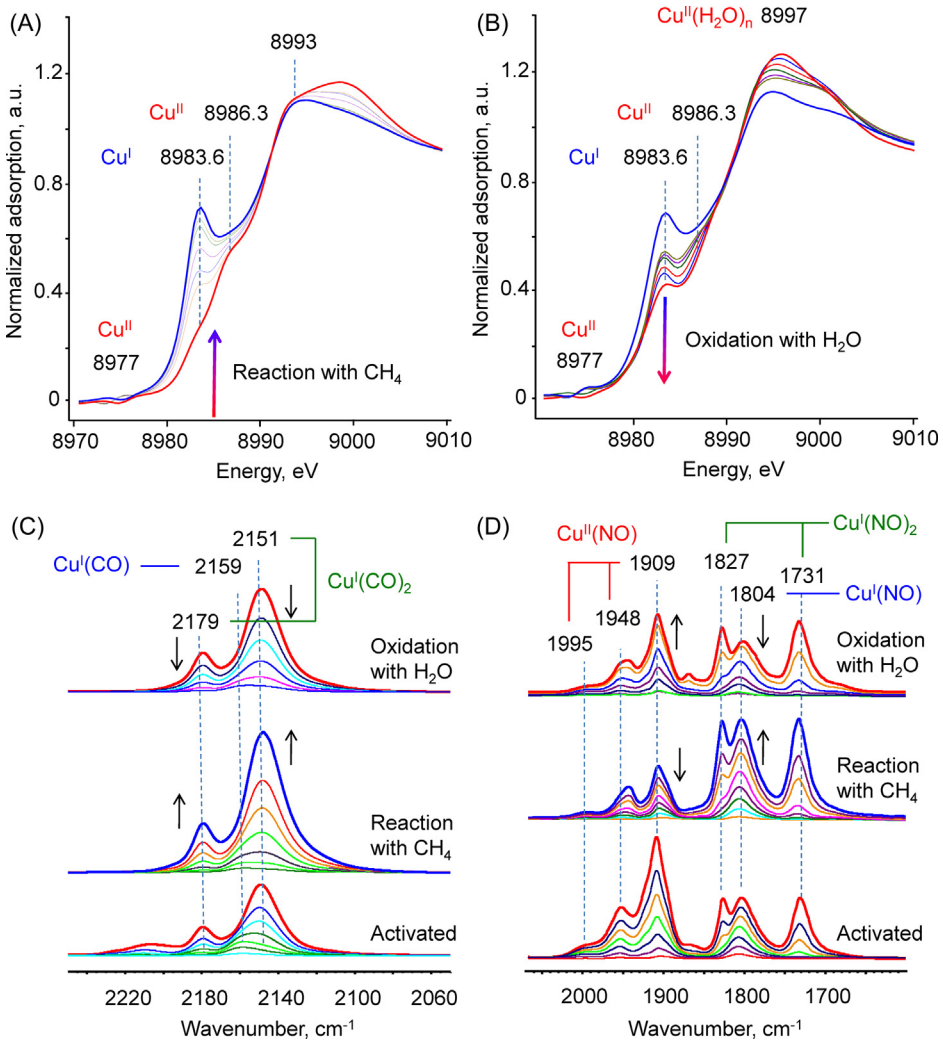

Fig. 9 (A) In situ XANES spectra recorded during the interaction of Cu@MOR (pretreated in helium flow) with methane at 473 K. (B) In situ XANES spectra recorded during the interaction of water vapor with Cu@MOR at 473 K and 1 bar after the methane reaction. (C) FTIR spectra of CO adsorbed at 100 K onto Cu@MOR that was vacuum-activated (bottom), reacted with methane (middle), and reoxidized with water vapor (top). (D) FTIR spectra of NO adsorbed at 100 K onto Cu@MOR that was vacuum-activated (bottom), reacted with methane (middle) and reoxidized with water vapor (top). Reproduced with permission from Sushkevich, V. L.; Palagin, D.; Ranocchiari, M.; van Bokhoven, J. A. Selective Anaerobic Oxidation of Methane Enables Direct Synthesis of Methanol. *Science* **2017**, *356*(6337), 523–527. Copyright 2017, Science.

(Fig. 10). The higher mobility of Cu hydroxide species compared to Cu-oxo species was also proposed by DFT calculations.[107] These observations underscore the fact that reaction conditions can have significant influence on the structure and properties of the active site. Therefore, the true active site catalyzing the reaction should be deduced by taking environment-induced structural reorganization into serious consideration.

The nature of the active sites and the mechanism of methane dehydroaromatization (MDA) by Mo@ZSM-5 zeolite catalysts has been revisited recently based on the data from advanced characterization techniques.[108] The reaction is operated under extremely harsh conditions. Additionally, the fresh catalyst needs to be carburized before the catalytic reaction takes place. Thus, the characterization of the active Mo species in the working catalyst has been a big challenge. Recently, a combination of operando XAS, STEM, and solid-sate NMR shed new light onto this "old" catalyst system.[109] Beale et al. utilized XRD, high energy resolution fluorescence detection (Kα-detected) X-ray absorption near-edge spectroscopy (HERFD-XANES) and X-ray emission spectroscopy (XES) under operando reaction conditions to study the nature of the molybdenum species during the MDA reaction over Mo/H-ZSM-5.[110]

The nature of the Mo species contributing to methane C—H bond activation and the formation of the aromatic products has been a subject of long-term debate in the scientific community. Both MoC_x and MoC_xO_y have been proposed to be active sites because it was not possible to distinguish the elements of carbon and oxygen.[111] By the combination of X-ray emission spectroscopy (XES) with HERFD-XANES, it was possible to unambiguously distinguish Mo-carbide and Mo-oxocarbide during the course of the reaction. For the first time, evidence was presented that Mo-oxocarbide species are responsible for the formation of C_2H_x/C_3H_x light hydrocarbons, while MoC_3 formed by MoC_xO_y carburization prompts benzene production. It was also proposed that the death of

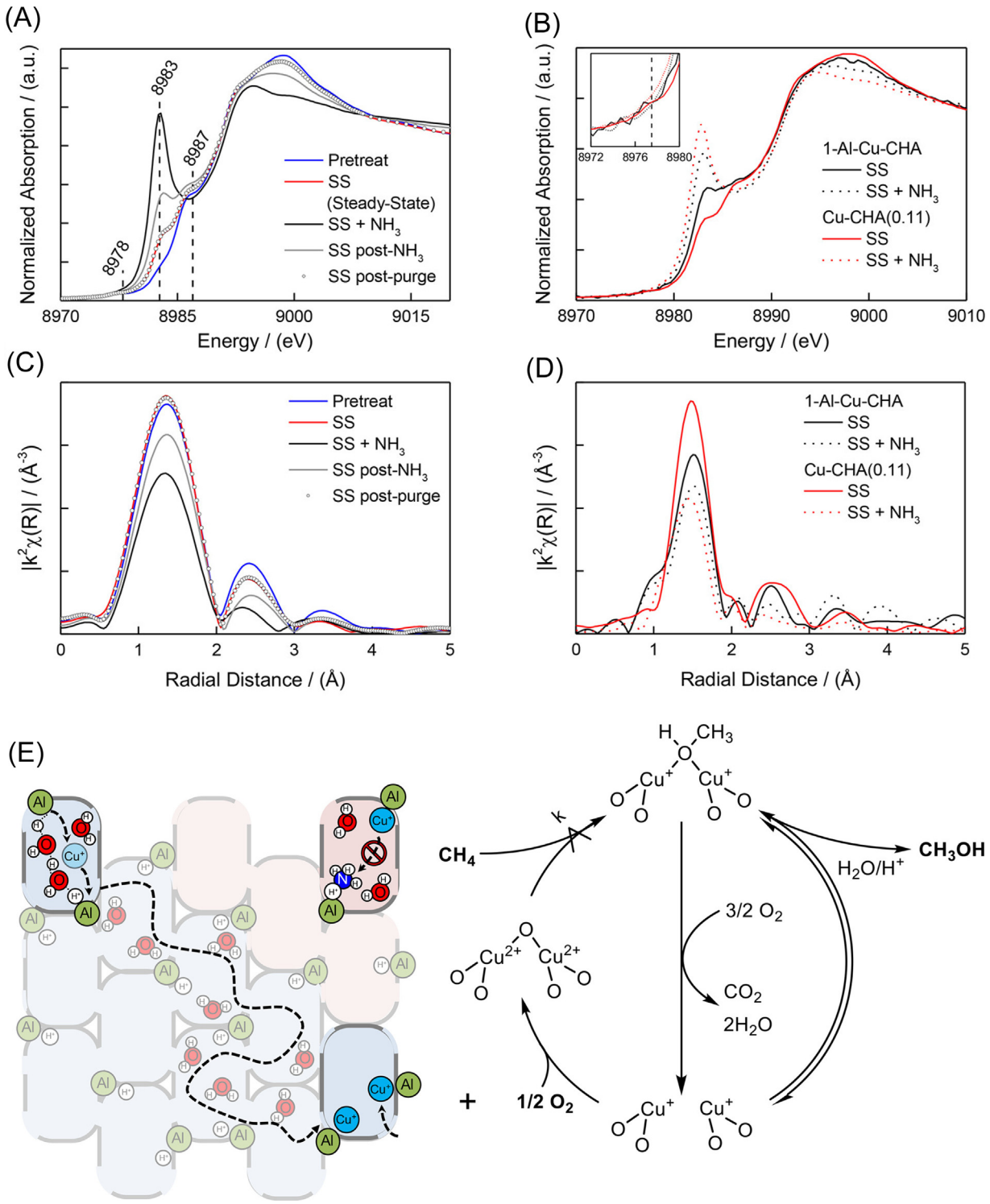

Fig. 10 (A) XANES and (B) EXAFS of Cu–CHA (0.11) and (C) XANES and (D) EXAFS of 1Al–Cu–CHA and Cu–CHA (0.11) under methanol synthesis and NH_3 flows. All spectra were collected at 543 K. The catalyst was pretreated in 1 kPa O_2, bal. He from 298 to 543 K at 5 K min^{-1} (pretreat). At 543 K, the catalyst was exposed to methanol synthesis flows of $P_{CH4} = 18$ kPa, $P_{02} = 0.09$ kPa, $P_{H2O} = 3.14$ kPa, bal. He (SS), an additional NH_3 cofeed of $P_{NH3} = 0.16$ kPa (SS + NH_3), and then the removal of NH_3 (SS post-NH_3). Following NH_3 removal, the catalyst was brought to 673 at 6 K min^{-1} and held in dry He before cooling to 543 K and exposure to methanol synthesis flows (SS post-purge). (E) Depiction of hypothesized H^+/H_2O-aided diffusion of Cu^+ and NH_3 inhibition within SSZ-13 to form Cu dimers relevant to the proposed catalytic methane oxidation cycle. Single O atoms may correspond to framework zeolite O atoms or coordinating H_2O molecules. Reproduced with permission from Dinh, K. T.; Sullivan, M. M.; Narsimhan, K.; Serna, P.; Meyer, R. J.; Dincă, M.; Román-Leshkov, Y. Continuous Partial Oxidation of Methane to

the catalyst is mainly caused by the sintering of MoC_3 and the deposition of large hydrocarbon species on the external surface of the zeolite.[110,112]

Kosinov, Hensen, and coworkers investigated the same reaction and catalyst with a specific focus on the early stages of MoO_x activation/carburization and induction period of benzene formation by operando spectroscopic tools.[109,113–117] They designed a high-resolution pulse reaction method to track the reaction.[113] The nature of the intrazeolite sites in Mo/ZSM-5 catalysts formed at the different stages of the reaction was probed by operando XANES while pulsing methane, high-resolution high-angle annular dark-field scanning transmission electron microscopy (HAADF-STEM) and energy-dispersive X-ray (EDX) elemental map of the catalysts (**Fig. 11**).[116,118] The results of nuclear magnetic resonance (NMR) and electron paramagnetic resonance (EPR) spectroscopy pointed to the crucial role of carbonaceous deposits formed in the course of the reaction for the conversion of methane to aromatic products.[116] Such polyaromatic species were proposed to act as the hydrocarbon pool for benzene production. Vollmer and co-workers applied an alternative CO carburization strategy avoiding the formation of carbonaceous species.[119] The active Mo species can thus be probed directly while eliminating the impact of the aromatic carbon. Based on the results of in situ XANES and ^{13}C NMR spectroscopy, the authors proposed that the active site is composed of two types of Mo oxycarbidic species.

Moliner et al. combined the "average" spectroscopy of in situ quantitative transient EXAFS and "local" microscopy of aberration-corrected HAADF-STEM to investigate the dynamic and reversible interconversion of Pt nanoclusters and single Pt metal atoms encapsulated in a nanocrystalline high-silica CHA zeolite under reduction and oxidation thermal treatments.[120] Pt nanoparticles of around 1 nm were found to be remarkably stable in the presence of H_2 and steam at 650 °C. However, these nanoparticles decomposed into site-isolated Pt single atoms upon switching to O_2 atmosphere during the calcination at 650 °C. Furthermore, such aggregation—decomposition process was found to be reversible enabling the efficient regeneration of the metal-zeolite composite catalysts. For instance, the coke deposited on the active site could be removed by calcination in O_2 and the H_2 treatment re-activated the metal catalytic sites (**Fig. 12**). Further studies on the dynamic interconversion between highly dispersed SAS Pt species, sub-nanometer Pt clusters, and small Pt nanoparticles revealed a general nature of the observed phenomenon that is highly sensitive to the specific reaction conditions, atmosphere, and operating temperature.[121] The development of in-situ and operando characterization is of great importance to provide comprehensive understandings of the dynamic transformation of the catalyst and true active site under catalyst working conditions and thus provide a fundamental basis for the rational design of tailor-made catalysts.[122]

6.06.3.3 Vibrational spectroscopy

The most widely applied vibrational spectroscopies include Raman and IR, which have been intensively used in catalysis to provide a structural fingerprint of the active metal species in zeolites.[123] The speciation of Cu-oxo complexes confined in ZSM-5 zeolite was investigated by resonance Raman spectroscopy by Solomon and co-workers in 2009.[124] The most intensive isotope sensitive vibration at the 456 cm^{-1} was assigned to the symmetric stretch of the oxo group bridging two Cu metal center. The weak band at 870 cm^{-1} was assigned to the antisymmetric Cu-oxo stretch vibration mode (**Fig. 13**). Thus the intrazeolite site responsible for methane activation was exclusively attributed to the binuclear $(Cu_2O)^{2+}$ species, while all other proposed to date binuclear Cu clusters were ruled out. This result is consistent with the observation that methane activation is correlated with the disappearance of the UV–Vis band at 22700 cm^{-1}, that was also attributed to $(Cu_2O)^{2+}$ site.[125] The same group further identified two types of $(Cu_2O)^{2+}$ species located at different positions within mordenite. These species showed similar geometric and electronic properties but distinguishable activity toward methane activation. The subtle structural differences cannot be distinguished from the resonance Raman spectra.[126] However, by using probe molecules with different molecular sizes, it was indicated that the location of the reactive $(Cu_2O)^{2+}$ is very likely to be the 8 membered ring channels and side pockets of the MOR.[127] Besides the assignment of the active Cu-oxo species, resonance Raman was also used to identify the formation mechanism of the $(Cu_2O)^{2+}$ species by oxygen activation with pre-reduced Cu precursors. The characteristic resonance Raman bands at 735 and 269 cm^{-1} were assigned to isotope sensitive O—O and insensitive Cu—C vibrations of an intermediate of μ-(η^2:η^2) peroxo dicopper (II) species $(Cu_2O_2)^{2+}$. The combined results of UV–Vis spectroscopy and O_2 temperature-programmed desorption (O_2-TPD) led to a proposal that the $(Cu_2O)^{2+}$ active site is formed by incorporation of the excessive oxygen into the framework of zeolite with simultaneous oxidation of two Cu^+ spectators into Cu^{2+}.[128] However, this mechanism is still under debate because other types of Cu-peroxo species and radicals were also identified in similar Cu-containing zeolite materials.[129,130]

The nature of the Cr species confined in ZSM-5 was characterized by Gao et al. using in-situ UV–Vis, IR, operando Raman spectroscopy under methane dehydroaromatization reaction condition of 773–1123 K. Both isolated Cr^{6+} dioxo and Cr^{3+} mono-oxo species were identified as the dominant species.[131] The same methods were also used to study the speciation of molybdenum encapsulated in ZSM-5. **Fig. 14**A shows the electronic edge values based on in situ UV–Vis spectra of reference Mo oxide compounds and Mo-oxo species in ZSM-5. It was demonstrated that isolated mononuclear Mo-oxo species were relevant to the state of Mo in ZSM-5. Single metal $Mo(=O)_2^{2+}$ compensated by two Al sites corresponding to a Raman band at 993 cm^{-1} was observed for the ZSM-5 with Si/Al = 15. With increasing the Si/Al ratio, the new bands at 975 and 984 cm^{-1} were assigned to $Mo(=O)_2OH$ and

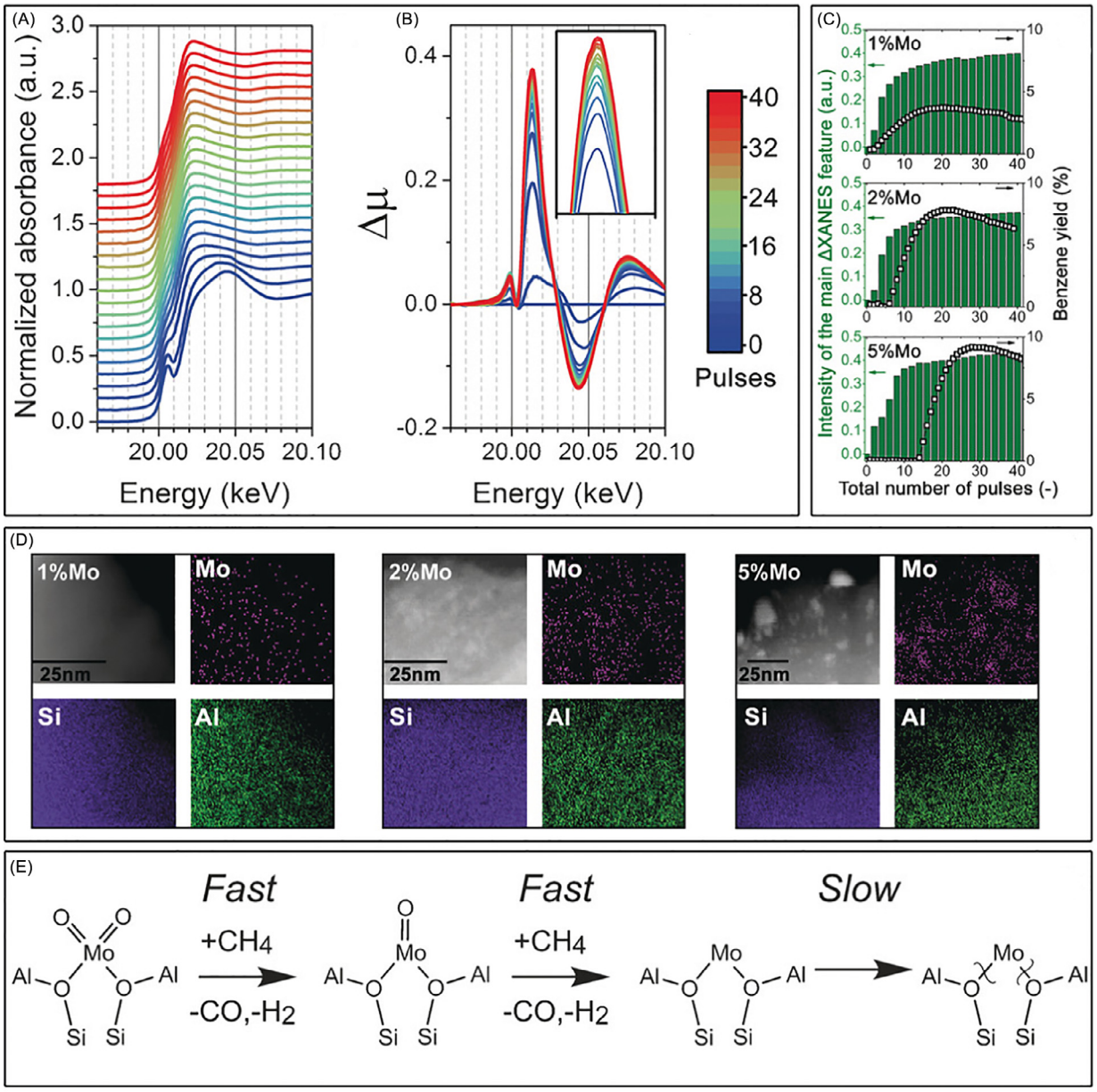

Fig. 11 (A) Operando Mo K-edge XANES spectra and (B) corresponding ΔXANES spectra recorded while pulsing methane at 700 °C over the 2% Mo zeolite catalyst. ΔXANES spectra were obtained using a spectrum recorded before pulsing methane as the background for subtraction. (C) Comparison of the intensity of the main ΔXANES feature at 20.015 keV and the benzene yield values obtained simultaneously by MS analysis for 1% Mo, 2% Mo, and 5% Mo catalysts. (D) HAADF-STEM images and corresponding EDX elemental maps of Mo/ZSM-5 catalysts obtained with the catalysts quenched at the maximum benzene yield. (E) Proposed evolution of the active Mo phase. Reproduced with permission from Kosinov, N.; Wijpkema, A. S. G.; Uslamin, E.; Rohling, R.; Coumans, F. J. A. G.; Mezari, B.; Parastaev, A.; Poryvaev, A. S.; Fedin, M. V.; Pidko, E. A.; Hensen, E. J. M. Confined Carbon Mediating Dehydroaromatization of Methane over Mo/ZSM-5. *Angew. Chem. Int. Ed.* **2018**, *57*(4), 1016–1020. Copyright 2018, Wiley.

$(Si{-}O{-})_2Mo(=O)_2$ species anchored on sites with one Al atom and on the external surface, respectively (Fig. 14B). Importantly, operando Raman spectroscopy indicated that the Mo-oxo sites gradually reduced to oxycarbide or carbide species in the course of methane dehydroaromatization reaction, and they could be restored and even enhanced by the oxidation treatment with oxygen (Fig. 14C and D).[132] The nature of the reactive extraframework Fe confined in zeolite, the so-called α-Fe and the related reaction intermediate of α-O, was for the first time distinguished from the inactive spectators of other iron-containing species by UV–Vis and variable-temperature variable-field magnetic circular dichroism (VTVH-MCD) spectroscopy. The α-Fe was assigned to be a mononuclear high-spin Fe^{2+} site stabilized in the 6-membered ring of zeolite framework in a square planar configuration, while α-O is a mononuclear Fe(IV)=O species generated by α-Fe reacting with N_2O. The exceptionally high reactivity of the α-O

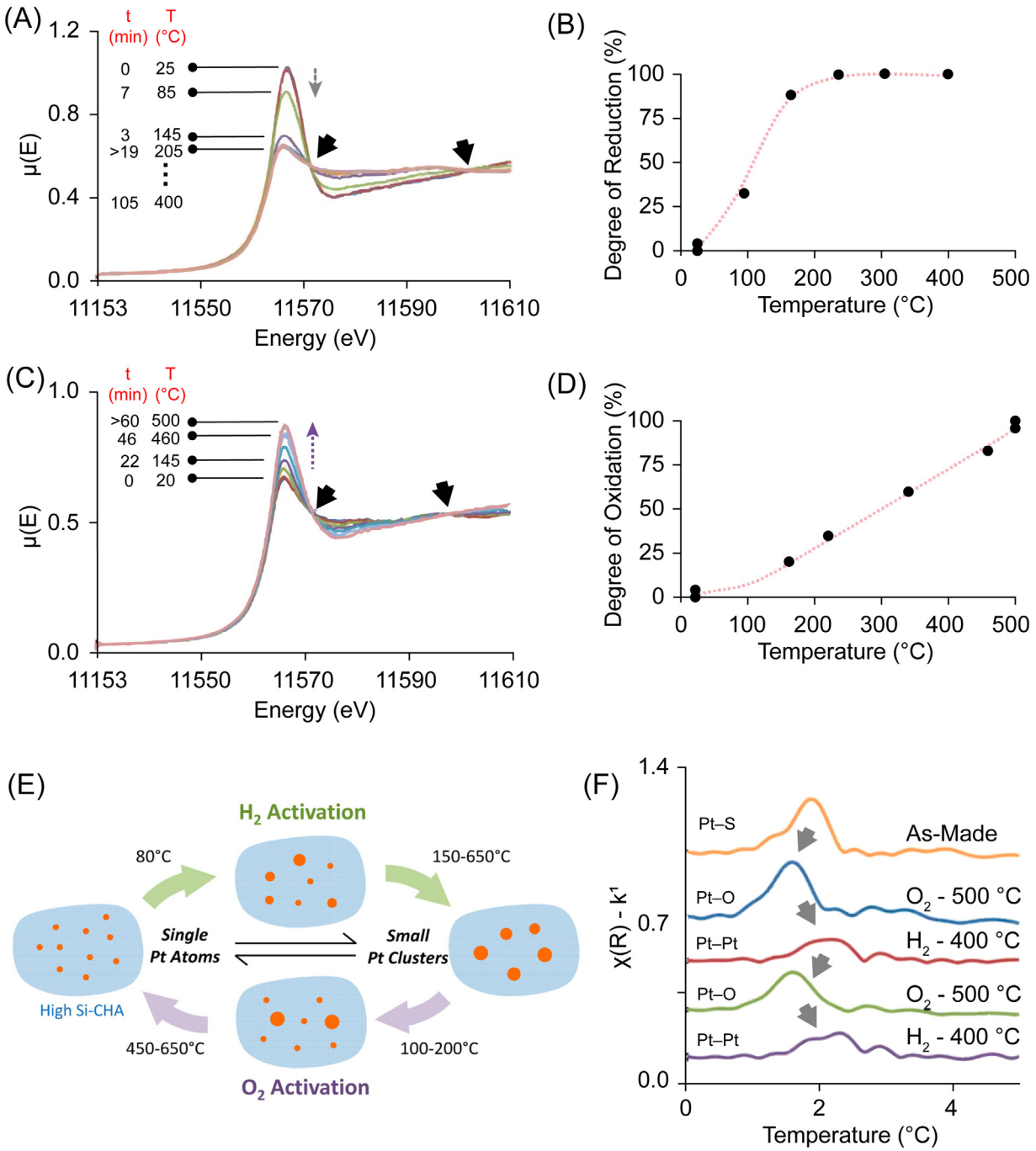

Fig. 12 (A) Time-resolved XANES spectra of Pt—CHA-2 (previously calcined in air at 500 °C) in 4% H_2 as the temperature is ramped from 25 to 400 °C at 10 °C/min; (C) Time-resolved XANES spectra of Pt—CHA-2 (previously reduced in H_2 at 400 °C) in 20% O_2 as the temperature is ramped from 25 to 500 °C at 10 °C/min; (B) and (D) show the degree of reduction and oxidation, respectively, as a function of the temperature. The solid arrows point to the formation of well-defined isosbestic points during the treatments. (E) FT-EXAFS spectra of Pt—CHA-2 after various thermal treatments (the arrows indicate the direction of the sequence and corresponding changes in structural features). (F) Schematic illustration of the revisable transformation. Reproduced with permission from Moliner, M.; Gabay, J. E.; Kliewer, C. E.; Carr, R. T.; Guzman, J.; Casty, G. L.; Serna, P.; Corma, A. Reversible Transformation of Pt Nanoparticles into Single Atoms Inside High-Silica Chabazite Zeolite. *J. Am. Chem. Soc.* **2016**, *138*(48), 15743–15750. Copyright 2016, American Chemical Society.

intermediate toward methane C—H bond activation is due to the geometrical constraints enforced by the zeolite lattice.[6] A mononuclear Cu species anchored to the silanol defect site was also identified by deconvolution of the experimental UV–Vis spectra by simulated excitation signals of different Cu/SSZ-13 models.[133] However, precise assignment of the UV–Vis spectroscopic features to specific Cu structures is precluded, for the broad peaks usually result in the overlap of signals from the heterogeneous mixture of Cu motifs.[134]

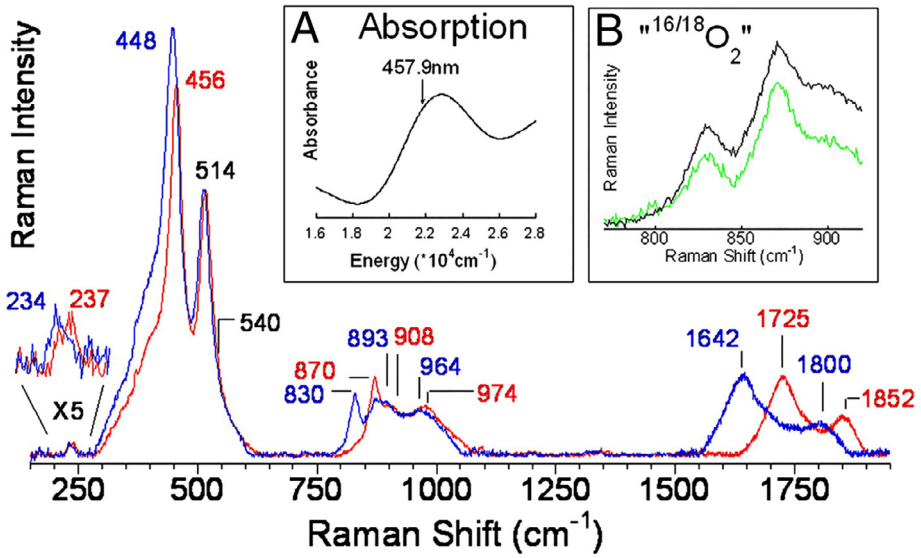

Fig. 13 Resonance Raman spectra ($\lambda_{ex} = 457.9$ nm) of Cu-ZSM-5. $^{16}O_2$ (red), $^{18}O_2$ (blue). Inset A: Absorption spectrum of oxygen-activated Cu-ZSM-5. Inset B: "$^{16,18}O_2$" (green), and 1:1 normalized sum of $^{16}O_2$ and $^{18}O_2$ (black). Reproduced with permission from Woertink, J. S.; Smeets, P. J.; Groothaert, M. H.; Vance, M. A.; Sels, B. F.; Schoonheydt, R. A.; Solomon, E. I. A $[Cu_2O]^{2+}$ Core in Cu-ZSM-5, the Active Site in the Oxidation of Methane to Methanol. *Proc. Natl. Acad. Sci. U.S.A.* **2009**, *106*(45), 18908–18913. Copyright 2009, the United States National Academy of Sciences.

IR spectroscopy is another major and well-established tool for the characterization of zeolite materials.[135] The detailed structure of the Brønsted acid sites and their interaction with Lewis sites can be directly distinguished by the signals of hydroxyl groups. Besides, CO is the most widely used IR probe molecule for characterizing cationic sites in zeolites, while different probe molecules could discriminate different coordination and oxidations state, and often the combined use of distinctly different probes is of importance for achieving a comprehensive understanding of the local environments of zeolite materials.[136] Qualitative as well as quantitative information of the active site and reaction mechanism may be obtained simultaneously attributing to the development of time and space resolved operando IR spectroscopy.[18,137,138]

6.06.3.4 Solid-state nuclear magnetic resonance

NMR is a very powerful characterization tool since it is extremely sensitive to the chemical surrounding of the element investigated. Particularly, solid-state NMR (SSNMR) has emerged as a powerful spectroscopic technique capable of providing atomic-level resolution of the structure of the metal active sites in zeolite micropores, their local environment, and dynamic behavior.[139,140] Detection of the signal of nuclei of interests with low natural abundance becomes possible because of the improvement of the sensitivity of SSNMR due to the advanced instruments and in-situ and operando SSNMR methods recently developed.[141–146] For example, the speciation of such transition metals as Zn, Ga, and Mo have been investigated by SSNMR. To overcome the challenges of the low natural abundance of the NMR active isotopes as well as low gyromagnetic ratios, a 21.1 T ultrahigh field ^{95}Mo NMR spectrometer was used to investigate the nature of the Mo species of ^{95}Mo isotopically enriched Mo/ZSM-5. By comparison of the fresh and carburized catalyst, it was concluded that the carburized Mo species originating from the ion-exchanged Mo species had a good correlation with the aromatics formation rate during catalytic methane dehydroaromatization.[147,148]

The location, concentration, and internuclear distance of the synergetic active sites of metal-modified zeolite catalysts can be quantified by ^{1}H−M rotational-echo saturation-pulse double-resonance (S-RESPDOR) NMR experiment.[140] Deng et al. applied sensitivity enhanced HS-QCPMG (hyperbolic secant-quadrupolar Carr-Purcell-Meiboom-Gill) NMR technique at a high magnetic field of 18.8 T to characterize the nature of Zn species in HZSM-5 for methane C−H bond activation.[149] The signal of ^{67}Zn NMR exacerbated by the low loading of zinc species in HZSM-5 zeolite was improved by 16-fold using HS-QCPMG NMR. It was further improved by using ^{67}Zn (^{67}Zn, 89.6%) enriched precursors in preparation of the ^{67}Zn/HZSM-5 samples. The results indicated that there were two ^{67}Zn signals at 224 and 238 ppm which can be assigned to ion-exchanged Zn^{2+} species located in zeolite channels and highly dispersed ZnO particles, respectively (**Fig. 15**A). Furthermore, it was found that the strong acid site detected by ^{1}H magic angle spinning (MAS) NMR originated from the synergetic interaction between the Zn Lewis acid and the Brønsted acidic proton evidenced by the ^{1}H−^{67}Zn S-RESPDOR NMR data (**Fig. 15**B). The ^{1}H−^{67}Zn internuclear distance between the zeolite Brønsted acidic protons and the Zn^{2+} Lewis acid site was determined to be 2.70–3.34 Å (**Fig. 15**C). The enhanced Brønsted acidity and the reactivity Zn-HZSM-5 for C−H bond activation is a result of such a Lewis-Brønsted acid synergy. The same double-resonance technique was also used to unravel the Lewis-Brønsted acid synergy between acidic protons and Ga species in Ga/ZSM-5 zeolite contributing to its reactivity in the methanol-to-aromatics conversion.[150,151] Two types of Ga species, i.e. GaO^+ ions and GaO_x clusters, were proposed based on the results of the wideband uniform-rate smooth truncation and QCPMG (WURST-QCPMG) ^{71}Ga

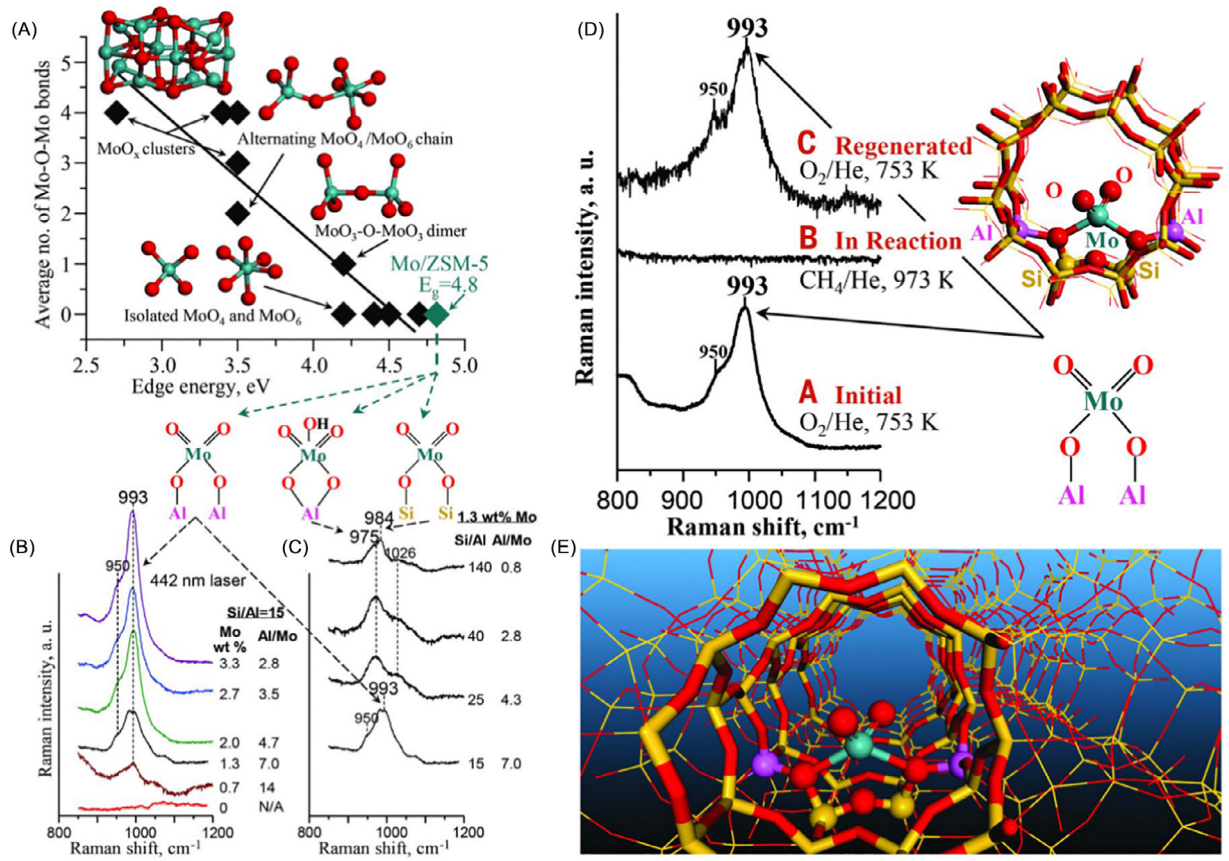

Fig. 14 (A) Electronic edge values based on in situ UV–Vis spectra of reference Mo oxide compounds exhibit a linear correlation with the number of bridging Mo—O—Mo covalent bonds around the central Mo cation. The value of 4.8 eV for 2 wt% Mo/ZSM-5 (Si/Al = 15) corresponds to Mo oxide species with a single Mo atom. (B and C) In situ Raman spectra of Mo/ZSM-5 catalysts under oxygen flow at 773 K as a function of (B) Mo loading for constant Si/Al = 15 and (C) Si/Al ratio for constant 1.3 wt% Mo loading with band assignments to Mo oxide species based on DFT calculations. A. u., arbitrary units. (D) Operando Raman spectra of 2 wt% Mo/ZSM-5 (Si/Al = 15). (E) Proposed initial $Mo(=O)_2^{2+}$ nanostructure anchored on double Al-atom framework sites. Reproduced with permission from Gao, J.; Zheng, Y. T.; Jehng, J. M.; Tang, Y. D.; Wachs, I. E.; Podkolzin, S. G. Identification of Molybdenum Oxide Nanostructures on Zeolites for Natural Gas Conversion. *Science* **2015**, *348*(6235), 686–690. Copyright 2015, Science.

NMR (Fig. 15D). The quantification of the Ga Lewis acid-Brønsted acid pairs was carried out by the $^{1}H-^{71}Ga$ S-RESPDOR NMR (Fig. 15E). The spectroscopy evidenced the localization of such pair sites at the 6-membered ring inside the zeolite channels (Fig. 15F). The presence of such synergistic sites has been correlated with aromatics selectivity.

Extraframework Al (EFAl) species generated upon the dealumination of the zeolite lattice can serve as Lewis acid sites and have significant influences on the catalytic properties of the zeolites. The chemical composition, structure, location, and distribution of EFAl have been intensively studied by various spectroscopic tools including solid-state NMR spectroscopy. The formation, coordination environment, and local structure of EFAl were investigated by one-dimensional single-pulse ^{27}Al MAS NMR and two-dimensional multiple-quantum magic angle spinning (MQ-MAS) NMR.[152,153] Many EFAl species such as $Al(OH)_3$, AlOOH, AlO^+, $Al(OH)_2^+$, and $AlOH^{2+}$ species have been directly identified in dealuminated zeolites by ^{1}H double-quantum MAS NMR (DQ-MAS NMR)[154] and ^{27}Al DQ-MAS NMR.[141] Very recently, the presence of three-coordinate EFAl-Al^{3+} species and their interaction with adjacent Brønsted acid site resulting in the enhanced acidity and catalyst activity has also been confirmed by the SSNMR combined with suitable probe molecules.[155,156] Spatial proximity of three types of EFAl, i.e. $Al(OH)_3$, $Al(OH)_2^+$, and $AlOH^{2+}$, in close association with the framework aluminum was confirmed by two-dimensional ^{27}Al DQ-MAS NMR.[141] The dealumination mechanism of EFAl species in zeolite during the high-temperature activation can be probed in situ by the high field sensitivity-enhanced ^{27}Al DQ-MAS NMR technique. The interaction of the framework aluminum pairs and cationic EFAl species was detected by a combination of multiple-quantum MAS (MQMAS) and two-dimensional double-quantum homonuclear NMR correlation spectroscopy.[157] The structure and location of other extraframwork metal species such as Ag and Ti confined in micropore of zeolites have also been examined by SSNMR.[158,159]

TS-1 has been widely used in industry as a catalyst for the epoxidation of propylene with hydrogen peroxide (H_2O_2). Over the past 40 years, there had been a consensus that the active site was a mononuclear Ti site on the framework of TS-1 zeolite until very

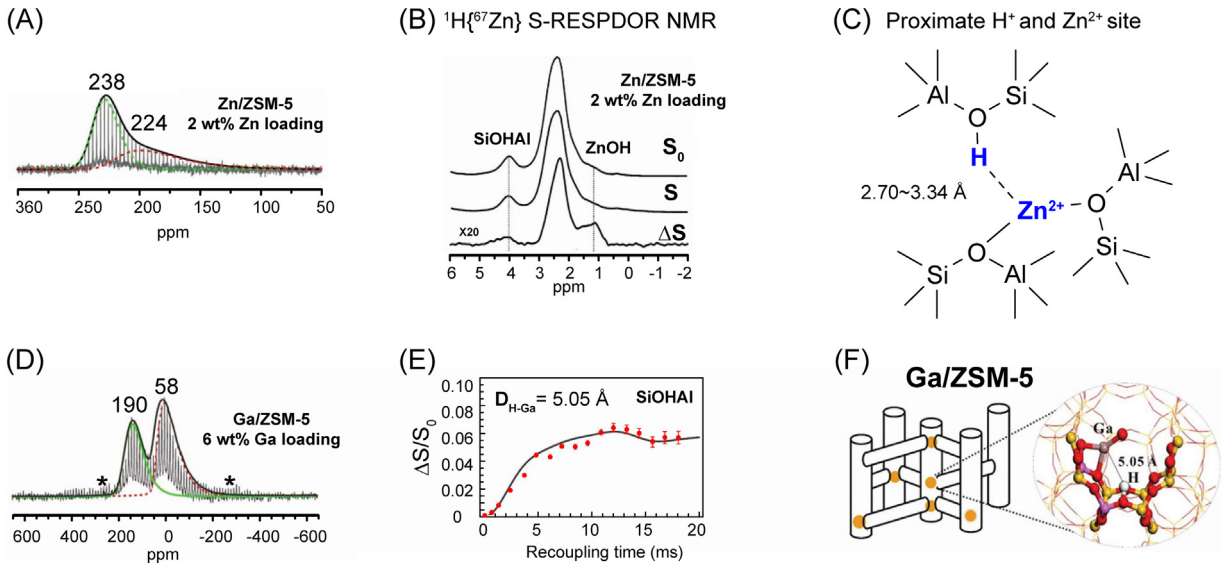

Fig. 15 (A) ^{67}Zn HS-QCPMG NMR spectrum of Zn/ZSM-5, (B) ^{1}H—^{67}Zn S-RESPDOR NMR spectrum, and (C) illustration of spatial interaction between Zn species and Brønsted acid site. (D) ^{71}Ga WURST-QCPMG NMR spectrum of Ga/ZSM-5, (E) ^{1}H—^{71}Ga S-RESPDOR build-up curve of Brønsted acidic proton and (F) model of proximate Ga species and Brønsted acid site in ZSM-5 channel.[140] Reproduced with permission from Li, S.; Lafon, O.; Wang, W.; Wang, Q.; Wang, X.; Li, Y.; Xu, J.; Deng, F., Recent Advances of Solid-State NMR Spectroscopy for Microporous Materials. *Adv. Mater.* **2020**, *32*(44), 2002879. Copyright 2016, Wiley.

recently Gordon et al. proposed a new binuclear Ti site.[160] The catalyst was studied by solid-state ^{17}O NMR in combination with other analytical techniques and computational modeling. It was found that the reaction intermediate detected by ^{17}O NMR is similar to that of the Berkessel–Katsuki catalyst, i.e. a homogeneous titanium catalyst that contains a binuclear Ti active site being able to catalyze the epoxidation reactions as well. This observation together with the simulated NMR spectra and mechanistic computational analysis confirmed that the cooperativity of two Ti sites within such a binuclear cluster embedded inside the zeolite lattice is key to providing the low-energy path for propylene epoxidation. This result is very interesting because binuclear Ti site was proposed earlier to be the active site based on the EXAFS results. However, the conclusion was not accepted by the catalysis community because the interpretation of the EXAFS peak was believed to be wrong.[161] It is thus suggested that the EXAFS data for TS-1 should be re-evaluated, and even further more-advanced characterizations should be carried out to further confirm the presence of the binuclear site. The reactivity of other Ti sites such as framework and extraframework defects as well as small titanium oxide clusters should not be assertively excluded and the composition dependence of TS-1 on the reaction conditions should be further investigated.[162] It proved that ^{17}O NMR is a very powerful technique that can be used to study the nuclearity of metal active sites in zeolites and the virtue of homogeneous catalyst can be realized by heterogenous catalysis.

6.06.4 Catalytic applications

Zeolites have been widely applied as robust catalysts for promoting various types of reactions by introducing nanoclusters and isolated metal sites as active components confined in the micropores. The design and development of bifunctional and multifunctional catalysts by encapsulation of metal-containing species in zeolite have significantly broadened the application of zeolite-based catalysts beyond the Brønsted acid-catalyzed reactions. Encapsulation of metal nanoclusters in zeolites has applications in diverse processes such as catalytic hydrogenation, hydrodeoxygenation, and oxidation reactions.[24,163,164] In the previous sections we were not able to avoid references to specific catalytic applications or mechanistic conclusions relevant to the advanced synthetic and characterization efforts. In this section, we discuss in more detail some selected catalytic applications in an attempt to highlight recent key mechanistic and conceptual discoveries relevant to catalysis by metal-containing clusters encapsulated in zeolite micropores.

6.06.4.1 C1 molecules conversion

Zeolite-supported metal nanoclusters and single-atom sites exhibit promising reactivity for the transformation of C1 molecules into various hydrocarbons and oxygenates.[165] For example, both Fe- and Cu-containing zeolites are active in partial oxidation of methane to methanol at mild conditions.[106,166–169] The activity of Cu@ZSM-5 was attributed by Sels and co-workers to the presence of binuclear $(Cu_2O)^{2+}$ sites in zeolite channels based on the results of in-situ UV–Vis, resonance Raman combined with DFT calculations.[124,128] Later, the trinuclear $(Cu_3O_3)^{2+}$ single site stabilized at the entrance of MOR side pocket was proposed as the alternative highly active methane oxygenation site capable of contributing with up to two out of three mu-oxo ligands in its

structure for the oxidation reaction at elevated pressure.[170,171] Methane conversion by Cu-zeolites is normally carried out in a stepwise process including the high-temperature activation of the Cu species, low-temperature methane oxidation, and methanol extraction with the assistance of water. The heating and cooling procedures limit the practical application of this approach. The first isothermal continuous cyclic process was reported by van Bokhoven's group.[172] The reaction procedure was optimized so that both Cu activation and methane oxidation can be operated at a relatively low temperature with 8 h of 1 bar oxygen and subsequent reaction under 6 bar of methane feeding. Methanol can be obtained directly by on-line water extraction at the same temperature.[172] It was further proposed that the molecular water can serve as an alternative soft oxidant oxidizing the Cu species to active Cu-oxo sites for activation of methane to methanol.[173] In such a scenario, the methanol selectivity over Cu@MOR can reach 97% with 0.202 mol CH_3OH per mole Cu methanol productivity.[97]

An alternative novel concept called "molecular fence" was established by Xiao et al.[174] The idea is to increase the local concentration of H_2O_2 oxidant around the encapsulated AuPd alloy nanoparticles in ZSM-5 zeolite by constructing a hydrophobic external surface around the zeolite. The organic substituent of the silane sheath can prevent the diffusion of H_2O_2 from the zeolite nanoreactor and thus increase the H_2O_2 concentration around the AuPd alloy. Meanwhile, hydrophobic methane molecules can easily access the AuPd active site through the hydrophobic silane sheath, and be oxidized to methanol over the AuPd active site with precisely concentrated on-site generated H_2O_2 oxidant. The catalyst exhibits high activity, excellent selectivity, and good recyclability. Methane conversion can reach 17.3% with methanol selectivity of 92%, corresponding to methanol productivity up to 91.6 millimoles per gram of AuPd per hour (**Fig. 16**).

Conversion of syngas to hydrocarbon by Fe, Co, and Zn-containing zeolites benefits from the bifunctional nature of these catalysts.[165] Water-gas shift reaction with high conversion of CO (70%) can be achieved by Pt nanoclusters encapsulated in NaA zeolite.[175] Catalytic selectivity in CO_2 hydrogenation can be tailored by adjusting the microporous environments. Rh@S-1 catalyst shows high activity for CO_2 conversion and maximized selectivity toward CO without deep hydrogenation. In contrast, the MFI-supported Rh nanoparticles exhibit high methane selectivity under similar conditions, indicating a strong correlation between the microporous environment and the catalyst selectivity.[176] Besides the superior catalytic activity and selectivity, various synthesis and post-synthetic approaches were developed to obtain robust nanoclusters or single-atom site confined in the zeolites with enhanced long-time stability and sintering/coke resistance in a variety of industrial conditions.[47] Bimetallic nanoclusters encapsulate in zeolites were synthesized with excellent stability and reactivity. AuPd@S-1 synthesized by the solvent-free method can convert bioethanol to acetic acid with $>80\%$ conversion and 95% selectivity in the presence of 90% water in the system.[43] The metal utilization rate in such applications reaches 98%. Xiao et al. reported a bimetallic RhMn core-shell nanoparticles RhMn@S-1 that can directly convert CO and H_2 into C_2-oxygenate with superior long-term durability.[177] Selectivity to ethanol of 88% at CO conversion of 42% was achieved.[177] The excellent catalytic performance was attributed to the sintering hindrance of the S-1 zeolite support which contributes to the stabilization of the active Mn-O-Rh^+ species even under reductive atmospheres.

6.06.4.2 Active site cooperation and multifunctionality in confined space

The bifunctionality of zeolite-based catalysts originating from the simultaneous presence of the metal and the Brønsted acid sites in the confined space of the zeolite micropores was found to be critically important for various catalytic reactions. By adjusting the density of each component, the reactivity and selectivity can be fine-tuned to optimize the catalyst performance.[70,163,178] Encapsulation of the isolated WO_4 sites in the immediate proximity with the Brønsted acid sites dramatically enhanced the productivity of propene by cross-metathesis of ethene and trans-2-butene. Such a cooperative catalyst gave rise to a production rate is ca. 7300 times that of the industrial WO_3/SiO_2-based catalyst. No observable side products and coke significantly formed under a wide range of reaction conditions.[70] The synergy between ultrasmall Ru clusters and zeolitic Brønsted acid sites was also found to be crucial for significant enhancement of the hydrogen evolution from ammonia borane hydrolysis. The hydrogen evolution rate was promoted by the formation of bifunctional Ru−H active sites between Ru clusters and adjacent Brønsted acid sites with tunable acidity, which could synergistically activate ammonia borane and water molecules. The TOF values of Ru/SAPO-34 and Ru/FAU are much higher than that of the commercial Ru/C catalyst, and are among the highest overall metal-based heterogeneous catalysts for ammonia borane decomposition reported so far under similar conditions (**Fig. 17**).[179]

Pt nanoclusters were encapsulated in HZSM-5 efficiently by a cationic polymer-assisted synthetic strategy.[33] The catalytic test indicated that Pt@HZSM-5 can promote tandem aldol condensation of furfural with acetone and the subsequent hydrogenation reaction by the synergy of metal and Brønsted acid sites, in contrast to the hydrogenation and decarbonylation of furfural promoted by Pt nanoparticles supported on HZSM-5 under identical conditions. The encapsulated metal clusters were found to be highly thermostable without significant metal sintering or leaching observed during catalyst regeneration. The same group further identified that this selective multistep tandem reaction is favorable only when the encapsulated Pt nanoparticles and Brønsted acid sites are adjacent with each other facilitating the access of the reaction intermediate to the active site of the subsequent reaction and reducing the catalyst deactivation.[180]

Besides the Brønsted acids, the heteroatom of zeolite framework, for instance, Ti sites of TS-1 zeolite can also synergistically interact with encapsulated metal nanoclusters to enhance the catalytic performances. The electron transfer from the Ti site of TS-1 to encapsulated Au nanoparticles weakens the O_2 adsorption and therefore promotes the in-situ formation of H_2O_2 for the vapor phase propylene epoxidation.[48] Atomically dispersed Au species can be stabilized and activated in zeolites by alkali ions (Na^+ and K^+) additives. The catalytic performance for the water-gas shift reaction at a temperature below 200 °C was comparable to the Au species on reduced metal oxide supports.[72] S-1 supported Ru single-atom catalyst shows activity in the catalytic ammonia synthesis

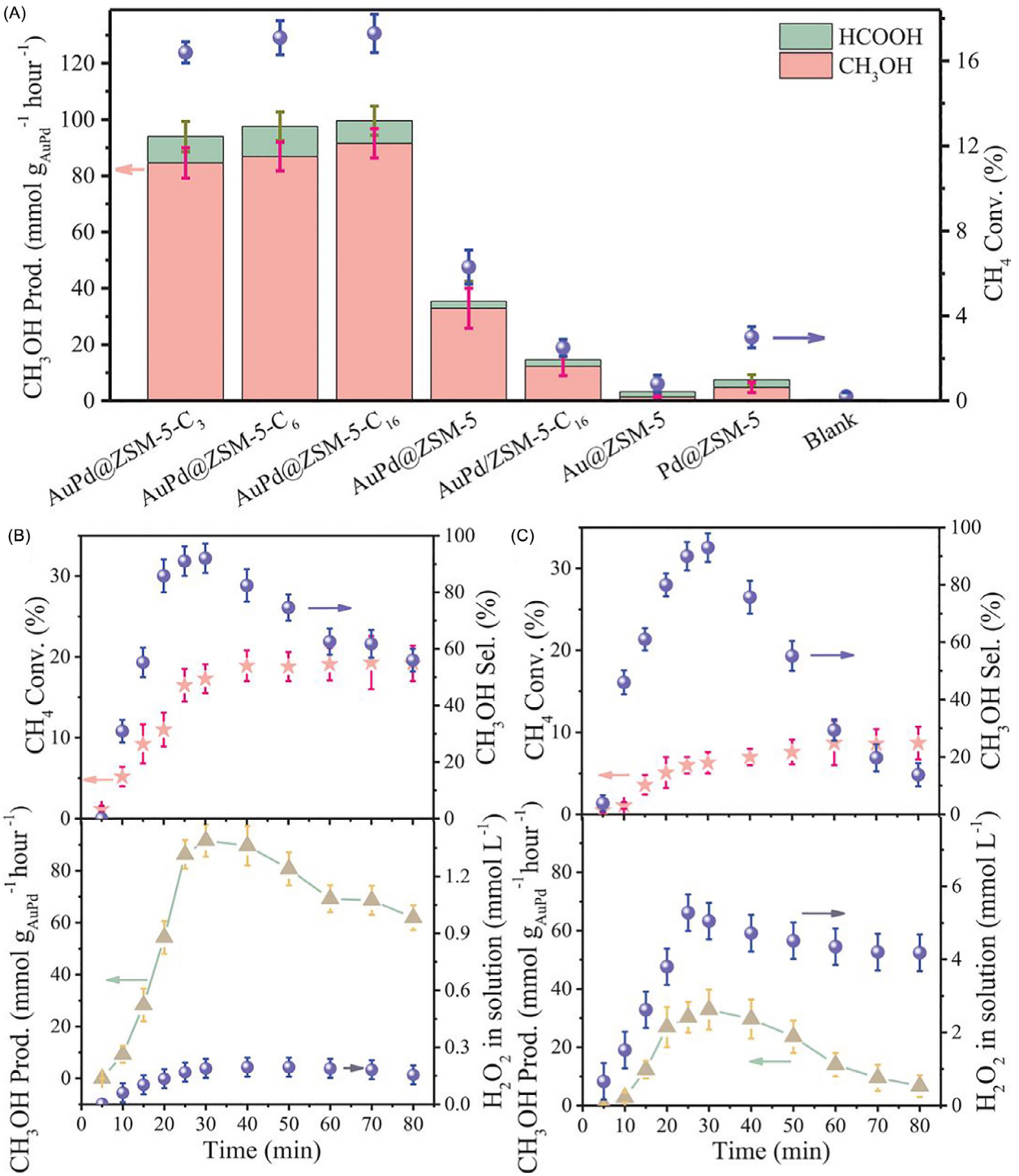

Fig. 16 (A) Data characterizing the oxidation of methane with H_2 and O_2 over various catalysts. Reaction conditions: 10 mL of water, 30 min, 70 °C, 27 mg of catalyst, feed gas at 3.0 MPa with 3.3% H_2/6.6% O_2/1.6% CH_4/61.7% Ar/26.8% He, and 1200 rpm (rpm). (B and C) Dependences of the methane conversion (Conv.), methanol selectivity (Sel.), methanol productivity (Prod.), and H_2O_2 concentration in water solution on reaction time over (B) AuPd@ZSM-5-C_{16} and (C) AuPd@ZSM-5 catalysts. Reaction conditions: 10 mL of water, 70 °C, 27 mg of catalyst, feed gas at 3.0 MPa with 3.3% H_2/6.6% O_2/1.6% CH_4/61.7% Ar/26.8% He, and 1200 rpm. Each reaction was tested eight times to obtain the error bars. Reproduced with permission from Jin, Z.; Wang, L.; Zuidema, E.; Mondal, K.; Zhang, M.; Zhang, J.; Wang, C.; Meng, X.; Yang, H.; Mesters, C.; Xiao, F.-S. Hydrophobic Zeolite Modification for In Situ Peroxide Formation in Methane Oxidation to Methanol. *Science* **2020**, *367*(6474), 193–197. Copyright 2020, Science.

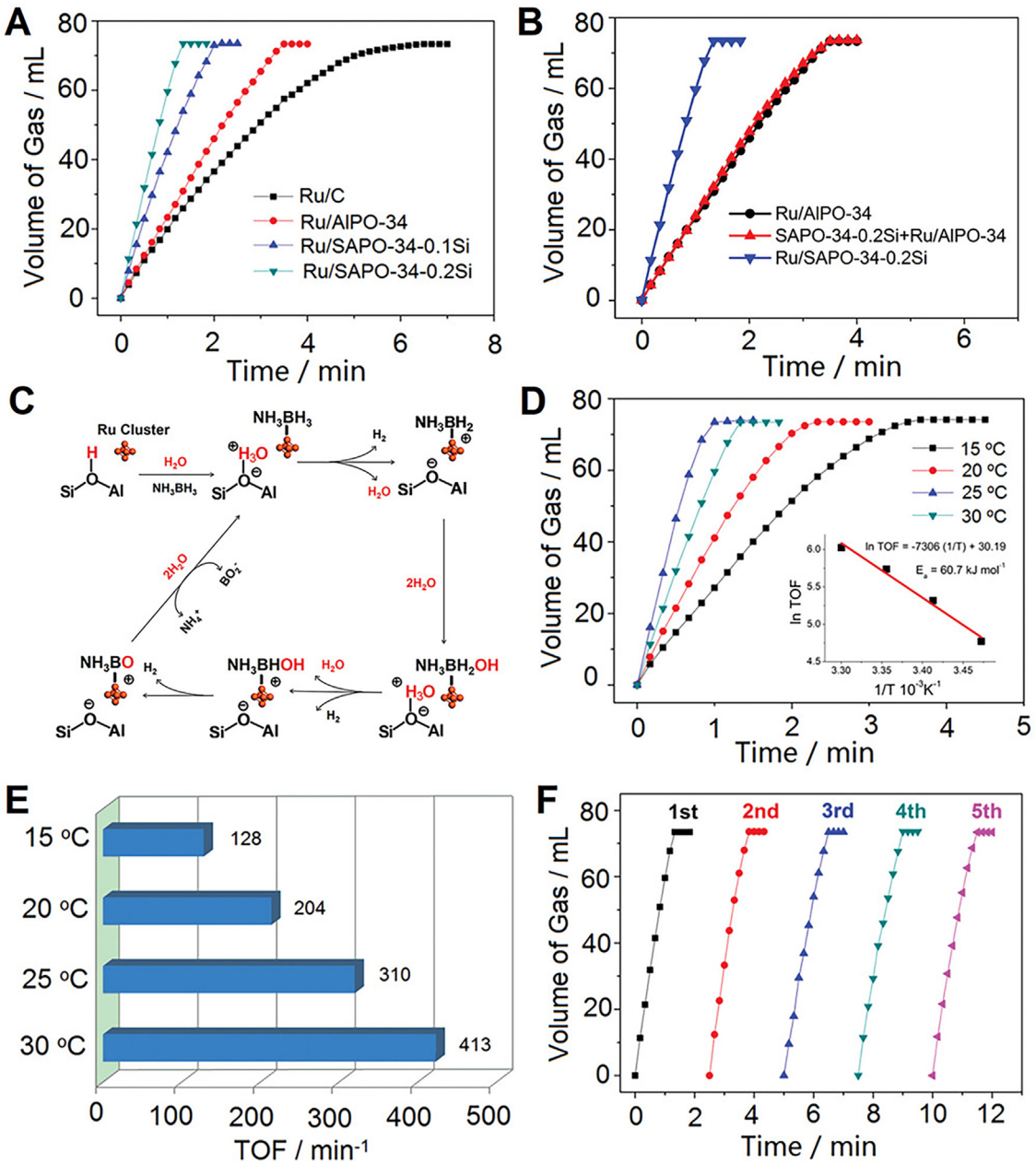

Fig. 17 (A and B) Volume of the H_2 generated from AB (1 M) hydrolysis versus time at 25 °C catalyzed by various catalysts ($n_{Ru}/n_{AB} = 0.007$). (C) The proposed mechanism for NH_3BH_3 hydrolysis over Ru/SAPO-34 catalysts. (D) Volume of the H_2 generated from AB (1 M) hydrolysis versus time and (E) corresponding TOF values at different temperatures catalyzed by Ru/SAPO-34-0.2Si catalyst ($n_{Ru}/n_{AB} = 0.007$), inset of (D): Arrhenius plot (ln TOF versus 1/T). (F) Durability tests for the AB (1 M) hydrolysis at 25 °C over Ru/SAPO-34-0.2Si catalysts ($n_{Ru}/n_{AB} = 0.007$). Reproduced with permission from Sun, Q.; Wang, N.; Bai, R.; Hui, Y.; Zhang, T.; Do, D. A.; Zhang, P.; Song, L.; Miao, S.; Yu, J. Synergetic Effect of Ultrasmall Metal Clusters and Zeolites Promoting Hydrogen Generation. *Adv. Sci.* **2019**, *6*(10), 1802350. Copyright 2019, Wiley.

higher than the most active conventional CsRu/MgO catalyst, and the ammonia synthesis rate can be further improved by 2 orders of magnitude by introducing a Ba promoter.[77] Yu and coworkers discovered that the bimetallic PtZn cluster encapsulated in S-1 has a very high propane dehydrogenation activity with 40.4% propane conversion with 99.3% selectivity to propene even after 13,000 min on stream without co-feeding H_2.[36] However, the performance of mono-metallic Pt@S-1 treated by conventional calcination/reduction process decreases to 19.8% and 2% after 2900 and 340 min on stream due to significant catalyst deactivation. The incorporation of Zn significantly enhances the stability of the subnanometer Pt clusters compared to that of $PtZn/Al_2O_3$ under identical conditions. Similar enhanced catalytic activity and sintering resistance were also observed in other bimetallic zeolite catalyst systems, attributed to the electronic interaction between Pt species and the second metal species in proximity as a stabilizer.[37,181]

Long-term catalyst regeneration and recyclization by the introduction of Cs cations into the system make PtZn@S-1 a promising new catalyst for industrial applications.[36,182]

6.06.4.3 Confined space for selectivity control

Encapsulation of metals into zeolites can selectively hydrogenate one specific functional group presented in one molecule adsorbing on the metal clusters. This represents an effective strategy to control the catalytic selectivity through the unique adsorption conformation with the target functional group on the metal active sites. By encapsulating Pd nanoclusters into zeolites, the multiple-substituted nitroarenes reactants can selectively adsorb to the Pd nanocluster via the nitro group. The unique end-on adsorption conformation constrains the activation of only one adsorbed nitro group with the other one in the molecule intact, giving extraordinary hydrogenation selectivity and stability toward aniline compared to conventional supported Pd catalysts (**Fig. 18**).[46,183] Selective hydrogenation of nitro group was achieved by the uniform bimetallic $PtZn_x$ nanoclusters encapsulated in MFI zeolite as well.[25] Xing et al. prepared Pt nanoparticles encapsulated in Y zeolite and found that the hydrogenation of the benzene ring of acetophenone can be completely suppressed due to the thermodynamically unfavorable end-on adsorption of acetophenone on the encapsulated Pt nanoparticles in Y zeolite.[184] The elusive para regioselectivity of oxidative coupling of toluene C–H bond of aromatics to produce biarylic compounds can be achieved by encapsulation of single Pd sites in Beta zeolite.[185] The selectivity to specific products can also be modulated by encapsulation of nano species into different zeolite frameworks or steering the steric hindrance and electronic property of the metal clusters by surface modification with alkali cation.[186] By fixation of TiO_2 in the micropore, the synergy between the two functionalities of photocatalytic activity of TiO_2 and the hydrophobic property of zeolite micropore

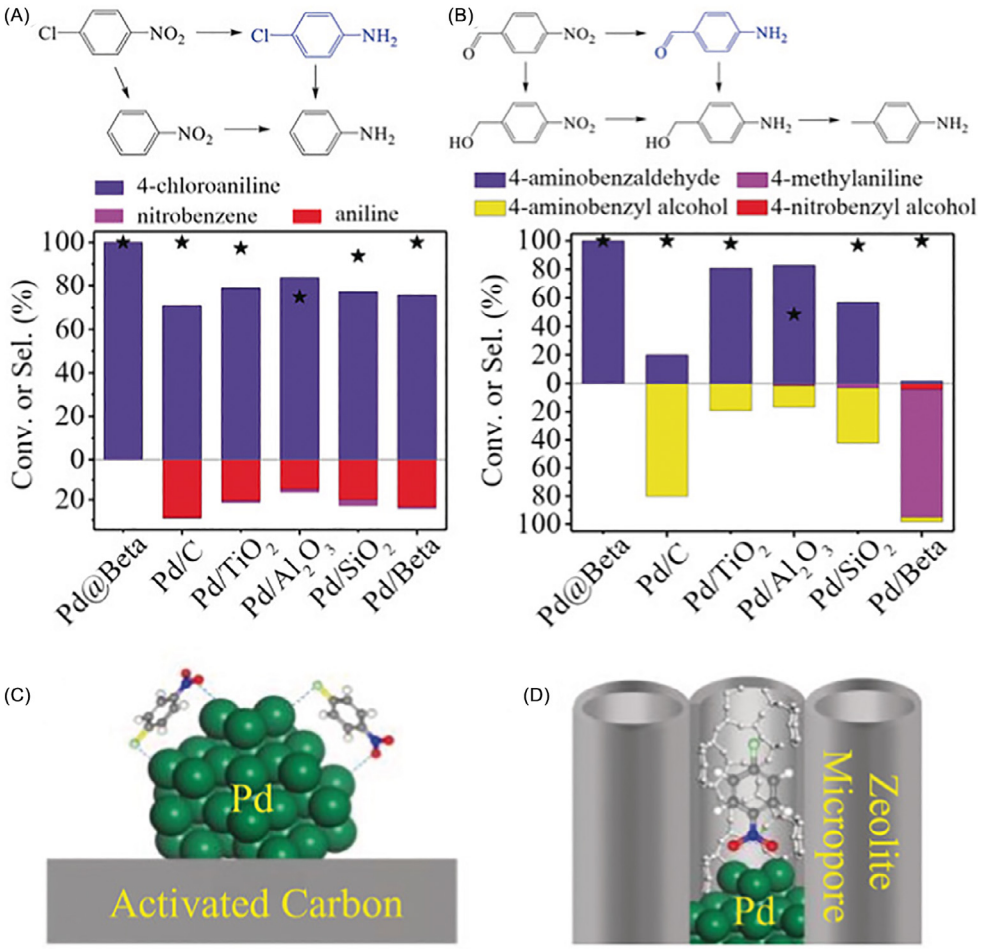

Fig. 18 Substrate conversions (★) and product selectivities (colored columns) for the hydrogenation of (A) 4-nitrochlorobenzene and (B) 4-nitrobenzaldehyde on various catalysts. Reaction conditions: substrate (1 mmol), Pd catalyst (0.2 mol %), toluene (10 mL), H_2 (1 MPa), 110 °C for 45 min (4-nitrochlorobenzene) or 80 °C for 2 h (4-nitrobenzaldehyde). Proposed models for the adsorption of 4-nitrochlorobenzene on (C) Pd/C and (D) Pd@Beta. C gray, Cl light green, H white, N blue, O red, Pd dark green. Reproduced with permission from Zhang, J.; Wang, L.; Shao, Y.; Wang, Y.; Gates, B. C.; Xiao, F.-S. A Pd@Zeolite Catalyst for Nitroarene Hydrogenation with High Product Selectivity by Sterically Controlled Adsorption in the Zeolite Micropores. *Angew. Chem. Int. Ed.* **2017**, *56*(33), 9747–9751. Copyright 2017, Wiley.

enhance the conversion of formaldehyde into CO_2 in a wet atmosphere.[187] In contrast, the hydrophobic nature of zeolite can also be fine-tuned to be hydrophilic by controllable functionalization of silanol groups of the zeolite. This way, the adsorption and diffusion of reactant and intermediates are dramatically influenced and the selectivity to specific products can be achieved.[188]

6.06.5 Computational modeling

In the previous section various state-of-art and advanced characterization tools for addressing the structural and mechanistic challenges of zeolite catalysis have been discussed. Next to the experimental strategies, computational modeling has been proven indispensable in understanding the physical and chemical properties of nanoclusters confined in zeolites. Nowadays computer simulations, particularly electronic structure calculations based on density functional theory, are widely used to address some of the most challenging fundamental questions such as the structure, electronic properties, and location of the nanoclusters, the interaction mechanism between the active site and the adsorbate, and the complex reaction networks underlying their catalytic properties. The development of operando modeling methodologies further narrows the gap between the experiment and the theoretical model and provides more insights into the nature of the active sites and the reaction mechanism under the realistic conditions.[189]

6.06.5.1 Structure prediction by operando thermodynamic analysis

The structure of the metal-containing species confined in zeolites and their specific locations related to the framework Al distribution are the most studied question by DFT simulations. At the early stage, various species such as isolated metal ions, small metal clusters, and metal-(hydro)oxo complexes have been evaluated by static DFT calculation. Usually, specific atomic structures were proposed based on the indirect experimental data, and then different local environments of T-sites and spatial distributions were screened and the most stable binding positions were proposed. In some cases, the spectra such as IR, Raman, and UV–Vis were also predicted and correlation with the experimental data was discussed. However, since these DFT calculations were approximated by in vacuum models at 0 K limit, there is a big gap between modeling and experiment. A growing volume of evidence has been accumulated in recent years that such oversimplified models can substantially deviate from the true reactive configurations formed and operating under the conditions of the catalytic reactions. A pragmatic solution to addressing the condition-dependencies of catalyst speciation is provided by the ab initio thermodynamic analysis (aïTA) approach[190] that allows expanding the energetics of different catalyst states and configurations computed in the idealistic vacuum/0 K model to the condition-dependent free energies reflecting the stabilities under the experimentally relevant conditions. In this approach, a simplified thermodynamic model is constructed to account for the impact of the finite temperature and pressure as well as the varying composition of the reactive atmosphere. By including as many as possible potential model structures, their formation Gibbs free energies and the associated condition dependencies can be computed providing thus a comprehensive thermodynamic picture of the active site structure. From this, direct information on the most stable and meta-stable configurations under specific reaction conditions can be predicted and related to the equilibrium stabilities of extra-framework species in zeolites.

Schneider and co-workers for prediction of the structure and oxidation state of Cu ions exchanged in SSZ-13 zeolite under the standard SCR of NO_x with NH_3.[191] It was found that both 4-fold Cu^I and 2-fold Cu^{II} species coordinated with H_2O or OH groups were the most stable complexes under a wide range of SCR conditions. We have extensively applied the aïTA approach to study the nature of active sites and catalytic mechanisms by a wide range of zeolite-based systems such Fe/ZSM-5,[192] Cu/MOR,[170,193] Al/FAU,[194] Mo/ZSM-5,[195] etc. Our most recent computational study on Mo/ZSM-5[195] also included the influence of the chemical potential of reactants and products into consideration to understand the evolution of the reactive ensembles in the course of the catalytic transformations. The formation Gibbs free energy of both mononuclear and binuclear Mo-(oxo)carbides were compared and the most stable Mo-containing species under the reaction atmosphere of CH_4, H_2, and CO were predicted. Besides the thermodynamic stability of these species, the probable formation process was also evaluated and the kinetically most favorable carburization pathways to MoC_x and MoC_xO_y were proposed (Fig. 19A and B).[195]

Although ab initio thermodynamics analysis is very useful for identifying the most relevant species under the catalyst working condition, the structural and compositional database of such analysis is still biased and heavily relied on the chemical knowledge and intuition of the researchers. To include diverse structures and elementary compositions into evaluation, a combination of aïTA with the methods of global optimization methods represent an attractive practical solution.[189,196,197] Very recently, we have explored the utility of genetic algorithm in combination with aïTA to determine the structure of EFAl cations in zeolite mordenite. The global optimization method was used to generate an extensive and comprehensive selection of feasible EFAl configurations with varied compositions, of which the stabilities were directly compared through the aïTA analysis (Fig. 19C).

6.06.5.2 Reactivity scaling relationship and beyond

Electronic structure calculations play nowadays a crucial role in understanding the molecular details and unraveling structure-activity relationships in zeolite catalysis. Computations are routinely used to compute barriers and energetics of the elementary steps in potential reaction pathways taking place over the reactive clusters inside the zeolite pores. The great advances in computational hardware and software of the past decades made it possible to carry out routinely transition state calculations on fully periodic zeolite models using modern computational resources. Nevertheless, the complete mapping of the whole reaction networks on

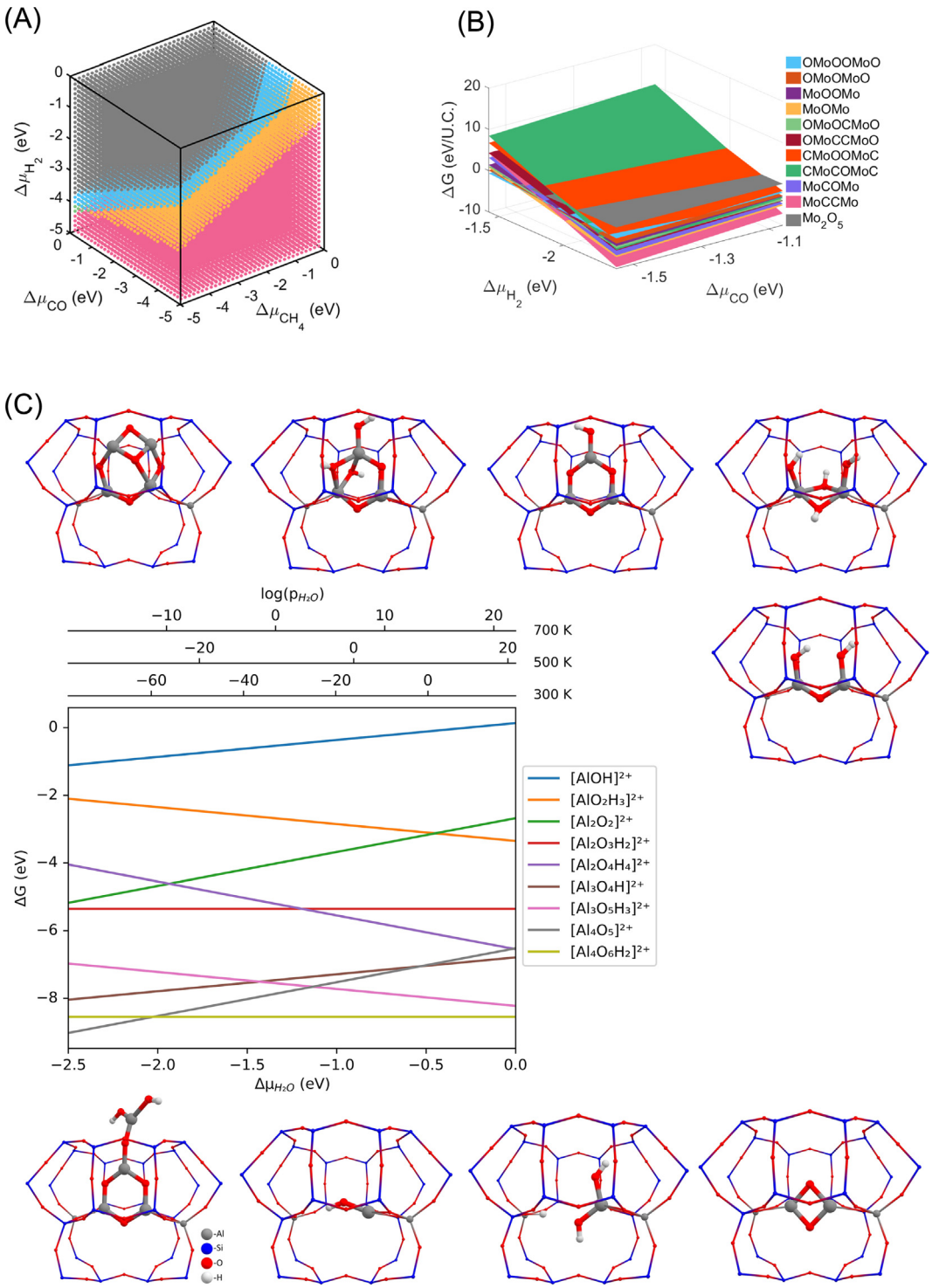

Fig. 19 (A) Most stable $[Mo_2O_xC_y]^{2+}$ species as a function of chemical potentials of μ_{CH4}, μ_{CO}, and μ_{H2}. (B) Gibbs free energy of formation of $[Mo_2O_xC_y]^{2+}$ as a function of μ_{CO} and μ_{H2}. (C) Most stable configurations of extraframework Al-containing species identified by genetic algorithm and the corresponding ab initio thermodynamic stability analysis (unpublished results). (B) Reproduced with permission from Li, G.; Vollmer, I.; Liu, C.; Gascon, J.; Pidko, E. A. Structure and Reactivity of the Mo/ZSM-5 Dehydroaromatization Catalyst: An Operando Computational Study. *ACS Catal.* **2019**, *9*(9), 8731–8737. Copyright 2019, American Chemical Society.

the global potential energy surface is still outside the reach. Furthermore, the large-scale evaluation of the kinetic parameters for an extended set of possible structures using state-of-the-art electronic structure methods can be a very demanding and challenging task. Substantial efforts have been devoted in the last decades to formulate a unifying framework for predicting the activation barriers

using a single universal descriptor without the need of the most demanding step of locating transition state structures for each catalyst candidate. Such a reduction of the kinetic problem to a problem of thermodynamics (because the universal descriptor should be associated with the characteristics of the energy minima or the proposed active sites) is key to enabling high-throughput computational screening and reactivity assessment of the intrazeolite reactive ensembles with different structures and chemical compositions.

This approach has been proved successful in many studies on catalytic reactions on open surfaces of solid catalysts.[198] However, the number of reports utilizing this approach in the field of zeolite catalysis has been quite limited until recently.[199–204] Nørskov et al. discovered that the activation of the methane C–H bond within the pore of zeolites can also be correlated with two-dimensional descriptors of the hydrogen affinity of the active oxygen site (G_H) and the formation energy of such active site (G_f) (Fig. 20A).[204] Furthermore, the one-dimensional reaction rate volcano pot as a function of G_f was believed to be able to predict the reactivity of other types of material (Fig. 20B). The structure-property relationships of Cu exchanged ZSM-5 catalyst under reaction-relevant environments were established by Wang et al. using DFT calculation and operando FTIR spectroscopy.[205] It was found that the fraction of binuclear Cu species and the compression energy describing the interaction between adjacent adsorbates have a quantitative linear correlation with catalytic activities for NO decomposition and methane oxidation to methanol reactions (Fig. 20C–E).

However, Hermans et al. found that for transition metal clusters confined in zeolite, multiple descriptors and reconstruction of the active site induced by the adsorption of the molecule should be taken into explicit consideration to improve the accuracy of prediction.[206] It would be very promising if such a scaling relationship is always valid, however, later detailed studies of the C–H bond activation ability of Fe-containing nanocluster in ZSM-5 observed significant deviations due to variation of the active site location in zeolite and the different oxygen active site involved into the C–H bond activation (Fig. 21).[207] Detailed structural and electronic analysis demonstrated that both the local confinement effect of zeolite framework on the active site and the steric hindrance around the reaction center have substantial influences on the reactivity and the mechanism, and therefore, break the apparent linear scaling relationship between the reactivity and the simplified descriptor. Such reactivity beyond the linear scaling relationship was also observed by Liu et al.[208] They found that the protonation reactivity of the Brønsted acid sites in zeolites deviate from the linear scaling relationships described by either adsorption energy of probing molecule of NH_3 or the intrinsic acidity of

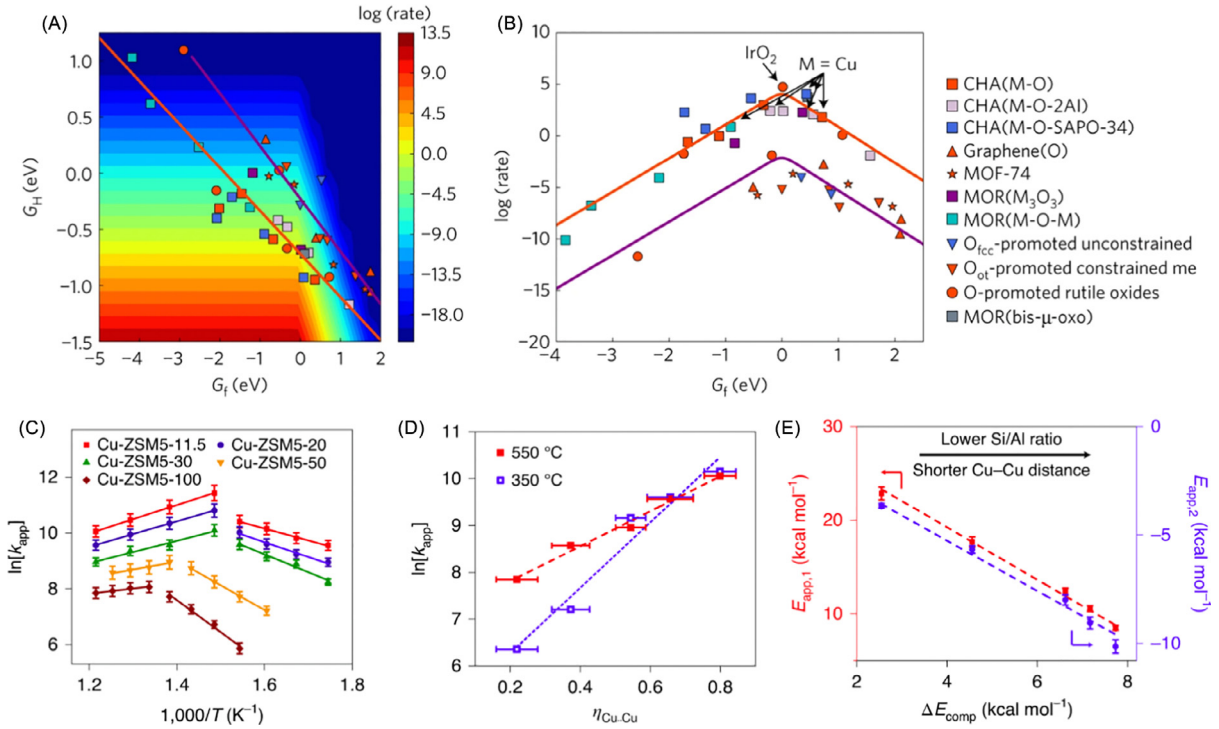

Fig. 20 (A) Two-dimensional volcano plot that includes G_H and G_f as descriptors for all explored materials. (B) One-dimensional volcano plot for the intrinsic rate of methane activation using G_f as a descriptor. An active site formation temperature of 450 °C and a methane activation temperature of 150 °C are used. (C) Arrhenius plots for rate constants versus 1/T. (D) Correlation between ln[k_{app}] at 350 and 550 °C and fractions of Cu dimers. (E) Correlation between apparent activation energies at low (red) and high temperatures (blue) and the compression energy derived from Ono–Kondo analysis. (B) Reproduced with permission from Latimer, A. A.; Kulkarni, A. R.; Aljama, H.; Montoya, J. H.; Yoo, J. S.; Tsai, C.; Abild-Pedersen, F.; Studt, F.; Nørskov, J. K. Understanding Trends in C–H Bond Activation in Heterogeneous Catalysis. *Nat. Mater.* **2016**, *16*, 225. Copyright 2016, Springer Nature. (E) Reproduced with permission from Xie, P.; Pu, T.; Aranovich, G.; Guo, J.; Donohue, M.; Kulkarni, A.; Wang, C. Bridging Adsorption Analytics and Catalytic Kinetics for Metal-Exchanged Zeolites. *Nat. Catal.* **2021**, *4*(2), 144–156. Copyright 2021, Springer Nature.

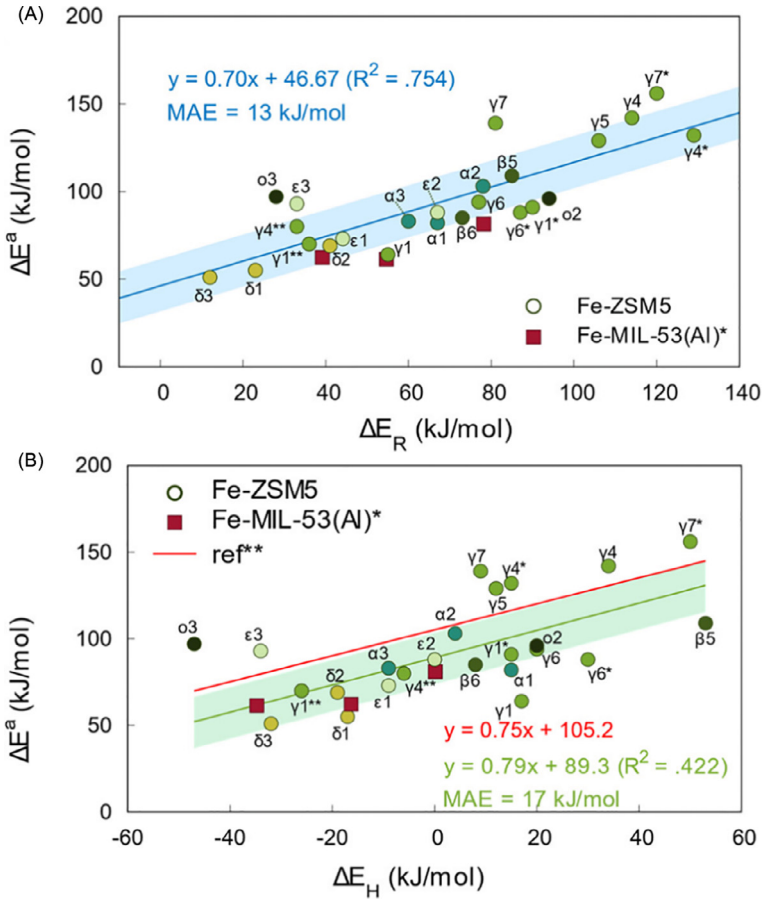

Fig. 21 Relationships between the computed kinetic (ΔE^a) and thermodynamic ((A) ΔE_R and (B) ΔE_H) parameters of methane activation by binuclear Fe sites in ZSM-5 zeolite (circles) and Fe-MIL-53 MOF (squares). The trend lines shown in the graph provide liner fits for the data sets with ±15 kJ/mol shown with shaded areas. Reproduced with permission from Szécsényi, Á.; Khramenkova, E.; Chernyshov, I. Y.; Li, G.; Gascon, J.; Pidko, E. A. Breaking Linear Scaling Relationships with Secondary Interactions in Confined Space: A Case Study of Methane Oxidation by Fe/ZSM-5 Zeolite. *ACS Catal.* **2019**, *9*(10), 9276–9284. Copyright 2019, American Chemical Society.

bond order, which implies that the reactions taking place in the micropore of zeolites are much more complicated and are governed by multiple factors beyond a single descriptor or two-dimensional descriptors. It also indicates that it is promising to explore new tailor-made zeolite catalysts for further activity improvement by circumventing the fundamental limitations of scaling relationships.[209,210]

6.06.5.3 Micro-kinetic modeling and dynamics

The combination of DFT reaction pathway calculation with microkinetic simulations is a widely applied and powerful strategy to investigate the complex reaction mechanism and optimize the catalyst performance. The intrinsic reaction energy and activation barriers calculated by DFT within the in vacuum condition and 0 K approximation can be converted by microkinetic modeling to macroscopic kinetic parameters such as the reaction rate, apparent activation barrier, and the coverage of the surface intermediates in terms of specific reaction conditions. Based on such information, the strategies for further optimization of the catalytic process and improve the catalyst selectivity to desired produced can be delivered.[211,212] For example, the previously discussed reactivity volcano plots by DFT coupled with microkinetic modeling have allowed the rational understanding of the correlation between the kinetic terms of activation barriers and the thermodynamic parameters of adsorption energy of one or more intermediates. DFT coupled with microkinetic modeling was used to study the reactivity of the Mo-containing nanoclusters in ZSM-5 zeolite. The location effect on the reactivity of the active site was evaluated (Fig. 22). It was found that the reactivity of Mo nanocluster toward methane dehydroaromatization reaction is very sensitive to the specific interaction motif with zeolite framework and the different confinement environment. The location of the most reactive site is the six-membered ring in the straight channel of ZSM-5 which has the lowest apparent activation barrier compared to Mo at other locations. More interestingly, it was found that the reaction rate-determining step is also site-dependent. Either the C−C bond coupling or C−H bond dissociation dominants the reaction rate at

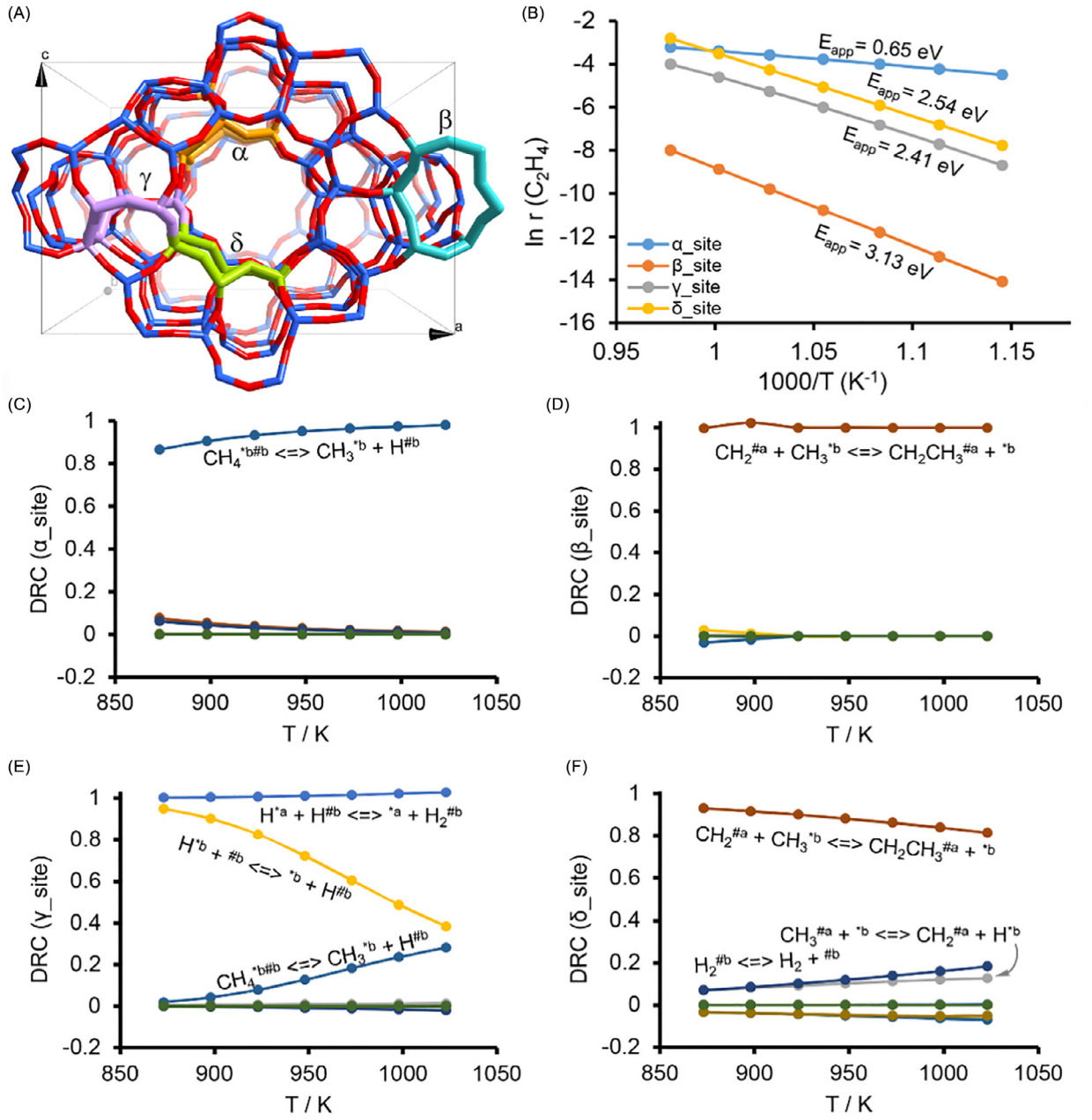

Fig. 22 (A) ZSM-5 framework and selected locations of reactive Mo clusters for MKM investigation. (B) Microkinetic modeling of methane activation over the active site of $[Mo_2C_2]^{2+}$ in ZSM-5. The formation rates r (in mol·s^{-1}) of ethylene as a function of temperature are presented. The apparent activation barriers (E_{app}) indicated in the figures were calculated using the Arrhenius equation. Dual-site microkinetic models were considered. (C–F) Calculated steady degree of rate control (DRC) analysis for methane activation over the $[Mo_2C_2]^{2+}$ site along ethylene pathways. Herein, * and # stand for the C and Mo sites of $[Mo_2C_2]^{2+}$, respectively (unpublished results).

different locations, indicating the heterogeneous nature of the reaction process in zeolite and providing new directions for further catalyst optimization.

Rational catalyst development and catalytic property improvement cannot be realized without fundamental insights into the dynamic nature of catalytic systems. Computational modeling has been intensively used to help assign spectra obtained from the experiment and detect the dynamics of the active site under catalyst working conditions by a combination of operando characterization and ab initio molecular dynamics (AIMD) and biased molecular dynamics. For example, the structural assignment of the condition-dependent Cu and Pd speciation in zeolite by XAS, DFT, and AIMD,[63,213,214] and the dynamic couple of isolated Cu active site into transient binuclear Cu clusters during the SCR of NH_3 discovered by ab initio metadynamics simulations discussed in Section 6.06.3 are good examples in this regards.[98,99] It was identified that the mobility of the active site can be elevated

due to the adsorption of water or NH_3 reactant and thus the reaction center is not limited to a specific framework anchoring site anymore. The Gibbs free energy obtained by ab initio molecular dynamics simulations is of great significance by the inclusion of enthalpic and entropic contributions into the total energy of the system, which are key factors influencing the reactivity and selectivity of zeolite confined reactions.[215–218] For example, it was found that the different reaction rates within MFI and Beta zeolites are a result of the impacts of the confinement and the intermolecular interactions of reaction intermediates, which dominate the intrinsic activation enthalpy and activation entropy of reactions.[219] By the combination of spectroscopic and microscopic characterizations and DFT calculations, an atomic-level quantitative analysis of the hydrothermal stability of isolated Cu^{2+} and $CuOH^+$ species were demonstrated by Song and coworkers. It is found that the Cu^{2+} is highly active and selective under a wide range of reaction temperatures, however, due to the low hydrolysis barrier, $CuOH^+$ gradually aggregated and converted into CuO_x clusters resulting in primary selectivity deterioration.[107]

6.06.6 Conclusion and perspective

The field of metal encapsulated zeolite materials is under fast development. Novel synthesis strategies have been developed to introduce nanocluster, subnanometric species, and single-atom sites into zeolite with good size and distribution control. Identification of the nature of the metal species inside zeolite is nowadays possible with an atomistic-level resolution by advanced microscopic and spectroscopic techniques. Especially the tremendous progress in the development and application of in-situ and operando characterization tools enables real-time tracking of the whole process of active site formation, substrate conversion, and catalyst deactivation, providing comprehensive qualitative and/or quantitative data and deep understanding about the structural flexibility and dynamic evolution of the active metal species and the reaction intermediates of a specific reaction. New bimetallic and bi- and multi-functional metal-containing zeolite catalysts have been successfully synthesized and improved to to the levels outperforming catalytic performances for existed and new reactions. Furthermore, the combination of experiment and computational modeling has become a regular approach for structure-performance-mechanistic studies. These remarkable achievements are very thrilling and inspiring for the next stage of generalized rational design of new zeolite-based heterogeneous catalysts with excellent activity, selectivity, and stability.

New versatile and generalized synthesis approaches should be continually developed. In-situ and operando characterization tools with improved time and spatial resolutions are desired to deconvolute the structure-property relationships and inherent intracluster heterogeneity coupled with both structural and dynamic perturbations.[220–224] On the one hand, the gap between realistic system and theoretical model should be further narrowed by investigating the reaction thermodynamics and kinetics in the microenvironment of zeolite pores under relevant reaction conditions.[225] On the other hand, high throughput calculations together with newly emerging machine learning methodologies and data-centered tools will significantly improve the efficiency of new zeolite synthesis,[226] reaction network construction and catalyst screening.[227,228] Although large effort has been put in studies on the direct catalyst fabrication and optimization, fundamental research of the transient sintering process and catalyst deactivation mechanism should be strengthened to provide insight into the nature of the sintering mechanisms. This knowledge can stimulate from a different angle novel strategies for the development of cutting-edge anti-sintering catalysts or regeneration processes. This is a big challenge that can only be addressed by the effective combination of multiple advanced characterization techniques and advanced computational modeling approaches.[229,230]

Acknowledgment

The authors acknowledge help with editing of selected graphics from the TsyfroCatLab of the University of Tyumen supported by the Tyumen region (Russia) by a grant to non-profit organizations no. 89-don.

References

1. Grommet, A. B.; Feller, M.; Klajn, R. Chemical Reactivity Under Nanoconfinement. *Nat. Nanotechnol.* **2020,** *15* (4), 256–271.
2. Wang, J.; Liu, L.; Dong, X.; Alfilfil, L.; Hsiung, C.-E.; Liu, Z.; Han, Y. Converting Hierarchical to Bulk Structure: A Strategy for Encapsulating Metal Oxides and Noble Metals in Zeolites. *Chem. Mater.* **2018,** *30* (18), 6361–6369.
3. Wang, L.; Xu, S.; He, S.; Xiao, F.-S. Rational Construction of Metal Nanoparticles Fixed in Zeolite Crystals as Highly Efficient Heterogeneous Catalysts. *Nano Today* **2018,** *20,* 74–83.
4. Serrano, D. P.; Melero, J. A.; Morales, G.; Iglesias, J.; Pizarro, P. Progress in the Design of Zeolite Catalysts for Biomass Conversion into Biofuels and Bio-Based Chemicals. *Catal. Rev. Sci. Eng.* **2018,** *60* (1), 1–70.
5. Ennaert, T.; Van Aelst, J.; Dijkmans, J.; De Clercq, R.; Schutyser, W.; Dusselier, M.; Verboekend, D.; Sels, B. F. Potential and Challenges of Zeolite Chemistry in the Catalytic Conversion of Biomass. *Chem. Soc. Rev.* **2016,** *45* (3), 584–611.
6. Snyder, B. E. R.; Vanelderen, P.; Bols, M. L.; Hallaert, S. D.; Böttger, L. H.; Ungur, L.; Pierloot, K.; Schoonheydt, R. A.; Sels, B. F.; Solomon, E. I. The Active Site of Low-Temperature Methane Hydroxylation in Iron-Containing Zeolites. *Nature* **2016,** *536* (7616), 317–321.
7. Shan, J.; Li, M.; Allard, L. F.; Lee, S.; Flytzani-Stephanopoulos, M. Mild Oxidation of Methane to Methanol or Acetic Acid on Supported Isolated Rhodium Catalysts. *Nature* **2017,** *551* (7682), 605–608.

8. Morejudo, S. H.; Zanon, R.; Escolastico, S.; Yuste-Tirados, I.; Malerod-Fjeld, H.; Vestre, P. K.; Coors, W. G.; Martinez, A.; Norby, T.; Serra, J. M.; Kjolseth, C. Direct Conversion of Methane to Aromatics in a Catalytic Co-ionic Membrane Reactor. *Science* **2016,** *353* (6299), 563–566.
9. Gao, P.; Li, S.; Bu, X.; Dang, S.; Liu, Z.; Wang, H.; Zhong, L.; Qiu, M.; Yang, C.; Cai, J.; Wei, W.; Sun, Y. Direct Conversion of CO_2 into Liquid Fuels with High Selectivity over a Bifunctional Catalyst. *Nat. Chem.* **2017,** *9* (10), 1019–1024.
10. Vogt, E. T. C.; Weckhuysen, B. M. Fluid Catalytic Cracking: Recent Developments on the Grand Old Lady of Zeolite Catalysis. *Chem. Soc. Rev.* **2015,** *44* (20), 7342–7370.
11. Beale, A. M.; Gao, F.; Lezcano-Gonzalez, I.; Peden, C. H. F.; Szanyi, J. Recent Advances in Automotive Catalysis for NOx Emission Control by Small-Pore Microporous Materials. *Chem. Soc. Rev.* **2015,** *44* (20), 7371–7405.
12. Zhang, R.; Liu, N.; Lei, Z.; Chen, B. Selective Transformation of Various Nitrogen-Containing Exhaust Gases Toward N_2 over Zeolite Catalysts. *Chem. Rev.* **2016,** *116* (6), 3658–3721.
13. Zeolite-Encapsulated Catalysts: Challenges and Prospects. In *Encapsulated Catalysts;* Farrusseng, D., Tuel, A., Sadjadi, S., Eds., Academic Press, 2017; pp 335–386. Chapter 11.
14. Valden, M.; Lai, X.; Goodman, D. W. Onset of Catalytic Activity of Gold Clusters on Titania with the Appearance of Nonmetallic Properties. *Science* **1998,** *281* (5383), 1647–1650.
15. Haruta, M. When Gold Is Not Noble: Catalysis by Nanoparticles. *Chem. Rec.* **2003,** *3* (2), 75–87.
16. Chen, M. S.; Goodman, D. W. The Structure of Catalytically Active Gold on Titania. *Science* **2004,** *306* (5694), 252–255.
17. Lee, S.; Molina, L. M.; López, M. J.; Alonso, J. A.; Hammer, B.; Lee, B.; Seifert, S.; Winans, R. E.; Elam, J. W.; Pellin, M. J.; Vajda, S. Selective Propene Epoxidation on Immobilized Au6–10 Clusters: The Effect of Hydrogen and Water on Activity and Selectivity. *Angew. Chem. Int. Ed.* **2009,** *48* (8), 1467–1471.
18. Rivallan, M.; Seguin, E.; Thomas, S.; Lepage, M.; Takagi, N.; Hirata, H.; Thibault-Starzyk, F. Platinum Sintering on H-ZSM-5 Followed by Chemometrics of CO Adsorption and 2D Pressure-Jump IR Spectroscopy of Adsorbed Species. *Angew. Chem. Int. Ed.* **2010,** *49* (4), 785–789.
19. Zečević, J.; van der Eerden, A. M. J.; Friedrich, H.; de Jongh, P. E.; de Jong, K. P. Heterogeneities of the Nanostructure of Platinum/Zeolite Y Catalysts Revealed by Electron Tomography. *ACS Nano* **2013,** *7* (4), 3698–3705.
20. Chai, Y.; Shang, W.; Li, W.; Wu, G.; Dai, W.; Guan, N.; Li, L. Noble Metal Particles Confined in Zeolites: Synthesis, Characterization, and Applications. *Adv. Sci.* **2019,** *6* (16), 1900299.
21. Wang, N.; Sun, Q.; Yu, J. Ultrasmall Metal Nanoparticles Confined within Crystalline Nanoporous Materials: A Fascinating Class of Nanocatalysts. *Adv. Mater.* **2019,** *31* (1), 1803966.
22. Wang, H.; Wang, L.; Xiao, F.-S. Metal@Zeolite Hybrid Materials for Catalysis. *ACS Cent. Sci.* **2020,** *6* (10), 1685–1697.
23. Kosinov, N.; Liu, C.; Hensen, E. J. M.; Pidko, E. A. Engineering of Transition Metal Catalysts Confined in Zeolites. *Chem. Mater.* **2018,** *30* (10), 3177–3198.
24. Zhao, Z.; Li, Y.; Feyen, M.; McGuire, R.; Mueller, U.; Zhang, W. Pd Nanoparticles Encapsulated in FER Zeolite Through a Layer Reassembling Strategy as Shape-Selective Hydrogenation Catalyst. *ChemCatChem* **2018,** *10* (10), 2254–2259.
25. Iida, T.; Zanchet, D.; Ohara, K.; Wakihara, T.; Roman-Leshkov, Y. Concerted Bimetallic Nanocluster Synthesis and Encapsulation Via Induced Zeolite Framework Demetallation for Shape and Substrate Selective Heterogeneous Catalysis. *Angew. Chem. Int. Ed.* **2018,** *57* (22), 6454–6458.
26. Moliner, M.; Gabay, J.; Kliewer, C.; Serna, P.; Corma, A. Trapping of Metal Atoms and Metal Clusters by Chabazite under Severe Redox Stress. *ACS Catal.* **2018,** *8* (10), 9520–9528.
27. Choi, M.; Wu, Z.; Iglesia, E. Mercaptosilane-Assisted Synthesis of Metal Clusters within Zeolites and Catalytic Consequences of Encapsulation. *J. Am. Chem. Soc.* **2010,** *132* (26), 9129–9137.
28. Goel, S.; Wu, Z.; Zones, S. I.; Iglesia, E. Synthesis and Catalytic Properties of Metal Clusters Encapsulated within Small-Pore (SOD, GIS, ANA) Zeolites. *J. Am. Chem. Soc.* **2012,** *134* (42), 17688–17695.
29. Goel, S.; Zones, S. I.; Iglesia, E. Encapsulation of Metal Clusters within MFI Via Interzeolite Transformations and Direct Hydrothermal Syntheses and Catalytic Consequences of Their Confinement. *J. Am. Chem. Soc.* **2014,** *136* (43), 15280–15290.
30. Liu, L.; Diaz, U.; Arenal, R.; Agostini, G.; Concepcion, P.; Corma, A. Generation of Subnanometric Platinum with High Stability During Transformation of a 2D Zeolite into 3D. *Nat. Mater.* **2017,** *16* (1), 132–138.
31. Liu, L.; Lopez-Haro, M.; Lopes, C. W.; Li, C.; Concepcion, P.; Simonelli, L.; Calvino, J. J.; Corma, A. Regioselective Generation and Reactivity Control of Subnanometric Platinum Clusters in Zeolites for High-Temperature Catalysis. *Nat. Mater.* **2019,** *18* (8), 866–873.
32. Liu, L.; Lopez-Haro, M.; Meira, D. M.; Concepcion, P.; Calvino, J. J.; Corma, A. Regioselective Generation of Single-Site Iridium Atoms and Their Evolution into Stabilized Subnanometric Iridium Clusters in MWW Zeolite. *Angew. Chem. Int. Ed.* **2020,** *59* (36), 15695–15702.
33. Cho, H. J.; Kim, D.; Li, J.; Su, D.; Xu, B. Zeolite-Encapsulated Pt Nanoparticles for Tandem Catalysis. *J. Am. Chem. Soc.* **2018,** *140* (41), 13514–13520.
34. Wang, N.; Sun, Q.; Bai, R.; Li, X.; Guo, G.; Yu, J. In Situ Confinement of Ultrasmall Pd Clusters within Nanosized Silicalite-1 Zeolite for Highly Efficient Catalysis of Hydrogen Generation. *J. Am. Chem. Soc.* **2016,** *138* (24), 7484–7487.
35. Sun, Q.; Wang, N.; Bing, Q.; Si, R.; Liu, J.; Bai, R.; Zhang, P.; Jia, M.; Yu, J. Subnanometric Hybrid Pd-$M(OH)_2$, M = Ni, Co, Clusters in Zeolites as Highly Efficient Nanocatalysts for Hydrogen Generation. *Chem* **2017,** *3* (3), 477–493.
36. Sun, Q. M.; Wang, N.; Fan, Q. Y.; Zeng, L.; Mayoral, A.; Miao, S.; Yang, R. O.; Jiang, Z.; Zhou, W.; Zhang, J. C.; Zhang, T. J.; Xu, J.; Zhang, P.; Cheng, J.; Yang, D. C.; Jia, R.; Li, L.; Zhang, Q. H.; Wang, Y.; Terasaki, O.; Yu, J. H. Subnanometer Bimetallic Platinum-Zinc Clusters in Zeolites for Propane Dehydrogenation. *Angew. Chem. Int. Ed.* **2020,** *59,* 19450–19459.
37. Zhu, J.; Osuga, R.; Ishikawa, R.; Shibata, N.; Ikuhara, Y.; Kondo, J. N.; Ogura, M.; Yu, J. H.; Wakihara, T.; Liu, Z. D.; Okubo, T. Ultrafast Encapsulation of Metal Nanoclusters into MFI Zeolite in the Course of Its Crystallization: Catalytic Application for Propane Dehydrogenation. *Angew. Chem. Int. Ed.* **2020,** *59,* 19669–19674.
38. Wang, L. X.; Wang, L.; Meng, X. J.; Xiao, F. S. New Strategies for the Preparation of Sinter-Resistant Metal-Nanoparticle-Based Catalysts. *Adv. Mater.* **2019,** *31* (50), 18.
39. Ren, L.; Wu, Q.; Yang, C.; Zhu, L.; Li, C.; Zhang, P.; Zhang, H.; Meng, X.; Xiao, F.-S. Solvent-Free Synthesis of Zeolites from Solid Raw Materials. *J. Am. Chem. Soc.* **2012,** *134* (37), 15173–15176.
40. Wu, Q.; Wang, X.; Qi, G.; Guo, Q.; Pan, S.; Meng, X.; Xu, J.; Deng, F.; Fan, F.; Feng, Z.; Li, C.; Maurer, S.; Müller, U.; Xiao, F.-S. Sustainable Synthesis of Zeolites Without Addition of Both Organotemplates and Solvents. *J. Am. Chem. Soc.* **2014,** *136* (10), 4019–4025.
41. Meng, X.; Xiao, F.-S. Green Routes for Synthesis of Zeolites. *Chem. Rev.* **2014,** *114* (2), 1521–1543.
42. Jin, Y.; Sun, Q.; Qi, G.; Yang, C.; Xu, J.; Chen, F.; Meng, X.; Deng, F.; Xiao, F.-S. Solvent-Free Synthesis of Silicoaluminophosphate Zeolites. *Angew. Chem. Int. Ed.* **2013,** *52* (35), 9172–9175.
43. Zhang, J.; Wang, L.; Zhu, L.; Wu, Q.; Chen, C.; Wang, X.; Ji, Y.; Meng, X.; Xiao, F.-S. Solvent-Free Synthesis of Zeolite Crystals Encapsulating Gold-Palladium Nanoparticles for the Selective Oxidation of Bioethanol. *ChemSusChem* **2015,** *8* (17), 2867–2871.
44. Wang, C.; Wang, L.; Zhang, J.; Wang, H.; Lewis, J. P.; Xiao, F.-S. Product Selectivity Controlled by Zeolite Crystals in Biomass Hydrogenation over a Palladium Catalyst. *J. Am. Chem. Soc.* **2016,** *138* (25), 7880–7883.
45. Xie, B.; Zhang, H.; Yang, C.; Liu, S.; Ren, L.; Zhang, L.; Meng, X.; Yilmaz, B.; Müller, U.; Xiao, F.-S. Seed-Directed Synthesis of Zeolites with Enhanced Performance in the Absence of Organic Templates. *Chem. Commun.* **2011,** *47* (13), 3945–3947.
46. Zhang, J.; Wang, L.; Shao, Y.; Wang, Y.; Gates, B. C.; Xiao, F.-S. A Pd@Zeolite Catalyst for Nitroarene Hydrogenation with High Product Selectivity by Sterically Controlled Adsorption in the Zeolite Micropores. *Angew. Chem. Int. Ed. Engl.* **2017,** *56* (33), 9747–9751.
47. Zhang, J.; Wang, L.; Zhang, B. S.; Zhao, H. S.; Kolb, U.; Zhu, Y. H.; Liu, L. M.; Han, Y.; Wang, G. X.; Wang, C. T.; Su, D. S.; Gates, B. C.; Xiao, F. S. Sinter-Resistant Metal Nanoparticle Catalysts Achieved by Immobilization Within Zeolite Crystals Via Seed-Directed Growth. *Nat. Catal.* **2018,** *1* (7), 540–546.

48. Wang, L.; Dai, J. J.; Xu, Y.; Hong, Y. L.; Huang, J. L.; Sun, D. H.; Li, Q. B. Titanium Silicalite-1 Zeolite Encapsulating Au Particles as a Catalyst for Vapor Phase Propylene Epoxidation with H_2/O_2: A Matter of Au-Ti Synergic Interaction. *J. Mater. Chem. A* **2020,** *8* (8), 4428–4436.
49. Qiao, B.; Wang, A.; Yang, X.; Allard, L. F.; Jiang, Z.; Cui, Y.; Liu, J.; Li, J.; Zhang, T. Single-Atom Catalysis of CO Oxidation Using Pt1/FeOx. *Nat. Chem.* **2011,** *3* (8), 634–641.
50. Wang, A.; Li, J.; Zhang, T. Heterogeneous Single-Atom Catalysis. *Nat. Rev. Chem.* **2018,** *2* (6), 65–81.
51. Thomas, J. M. Tens of Thousands of Atoms Replaced by One. *Nature* **2015,** *525* (7569), 325–326.
52. Liu, P.; Qin, R.; Fu, G.; Zheng, N. Surface Coordination Chemistry of Metal Nanomaterials. *J. Am. Chem. Soc.* **2017,** *139* (6), 2122–2131.
53. Lin, L.; Zhou, W.; Gao, R.; Yao, S.; Zhang, X.; Xu, W.; Zheng, S.; Jiang, Z.; Yu, Q.; Li, Y.-W.; Shi, C.; Wen, X.-D.; Ma, D. Low-Temperature Hydrogen Production from Water and Methanol Using Pt/α-MoC Catalysts. *Nature* **2017,** *544* (7648), 80–83.
54. He, X.; He, Q.; Deng, Y.; Peng, M.; Chen, H.; Zhang, Y.; Yao, S.; Zhang, M.; Xiao, D.; Ma, D.; Ge, B.; Ji, H. A Versatile Route to Fabricate Single Atom Catalysts with High Chemoselectivity and Regioselectivity in Hydrogenation. *Nat. Commun.* **2019,** *10* (1), 3663.
55. Liu, J. Catalysis by Supported Single Metal Atoms. *ACS Catal.* **2017,** *7* (1), 34–59.
56. Zhang, T.; Chen, Z.; Walsh, A. G.; Li, Y.; Zhang, P. Single-Atom Catalysts Supported by Crystalline Porous Materials: Views from the Inside. *Adv. Mater.* **2020;**, 2002910.
57. Goellner, J. F.; Gates, B. C.; Vayssilov, G. N.; Rösch, N. Structure and Bonding of a Site-Isolated Transition Metal Complex: Rhodium Dicarbonyl in Highly Dealuminated Zeolite Y. *J. Am. Chem. Soc.* **2000,** *122* (33), 8056–8066.
58. Liang, A. J.; Bhirud, V. A.; Ehresmann, J. O.; Kletnieks, P. W.; Haw, J. F.; Gates, B. C. A Site-Isolated Rhodium–Diethylene Complex Supported on Highly Dealuminated Y Zeolite: Synthesis and Characterization. *J. Phys. Chem. B* **2005,** *109* (51), 24236–24243.
59. Ogino, I.; Gates, B. C. Molecular Chemistry in a Zeolite: Genesis of a Zeolite Y-Supported Ruthenium Complex Catalyst. *J. Am. Chem. Soc.* **2008,** *130* (40), 13338–13346.
60. Uzun, A.; Bhirud, V. A.; Kletnieks, P. W.; Haw, J. F.; Gates, B. C. A Site-Isolated Iridium Diethylene Complex Supported on Highly Dealuminated Y Zeolite: Synthesis and Characterization. *J. Phys. Chem. C* **2007,** *111* (41), 15064–15073.
61. Lu, J.; Serna, P.; Aydin, C.; Browning, N. D.; Gates, B. C. Supported Molecular Iridium Catalysts: Resolving Effects of Metal Nuclearity and Supports as Ligands. *J. Am. Chem. Soc.* **2011,** *133* (40), 16186–16195.
62. Lu, J.; Aydin, C.; Browning, N. D.; Gates, B. C. Imaging Isolated Gold Atom Catalytic Sites in Zeolite NaY. *Angew. Chem. Int. Ed.* **2012,** *51* (24), 5842–5846.
63. Paolucci, C.; Parekh, A. A.; Khurana, I.; Di Iorio, J. R.; Li, H.; Albarracin Caballero, J. D.; Shih, A. J.; Anggara, T.; Delgass, W. N.; Miller, J. T.; Ribeiro, F. H.; Gounder, R.; Schneider, W. F. Catalysis in a Cage: Condition-Dependent Speciation and Dynamics of Exchanged Cu Cations in SSZ-13 Zeolites. *J. Am. Chem. Soc.* **2016,** *138* (18), 6028–6048.
64. Oda, A.; Torigoe, H.; Itadani, A.; Ohkubo, T.; Yumura, T.; Kobayashi, H.; Kuroda, Y. Unprecedented Reversible Redox Process in the ZnMFI—H_2 System Involving Formation of Stable Atomic ZnO. *Angew. Chem. Int. Ed.* **2012,** *51* (31), 7719–7723.
65. Phadke, N. M.; Van der Mynsbrugge, J.; Mansoor, E.; Getsoian, A. B.; Head-Gordon, M.; Bell, A. T. Characterization of Isolated Ga^{3+} Cations in Ga/H-MFI Prepared by Vapor-Phase Exchange of H-MFI Zeolite with $GaCl_3$. *ACS Catal.* **2018,** *8* (7), 6106–6126.
66. Chai, Y.; Wu, G.; Liu, X.; Ren, Y.; Dai, W.; Wang, C.; Xie, Z.; Guan, N.; Li, L. Acetylene-Selective Hydrogenation Catalyzed by Cationic Nickel Confined in Zeolite. *J. Am. Chem. Soc.* **2019,** *141* (25), 9920–9927.
67. Kistler, J. D.; Chotigkrai, N.; Xu, P.; Enderle, B.; Praserthdam, P.; Chen, C.-Y.; Browning, N. D.; Gates, B. C. A Single-Site Platinum CO Oxidation Catalyst in Zeolite KLTL: Microscopic and Spectroscopic Determination of the Locations of the Platinum Atoms. *Angew. Chem. Int. Ed.* **2014,** *53* (34), 8904–8907.
68. Tang, Y.; Li, Y.; Fung, V.; Jiang, D.-E.; Huang, W.; Zhang, S.; Iwasawa, Y.; Sakata, T.; Nguyen, L.; Zhang, X.; Frenkel, A. I.; Tao, F. Single Rhodium Atoms Anchored in Micropores for Efficient Transformation of Methane under Mild Conditions. *Nat. Commun.* **2018,** *9* (1), 1231.
69. Maeno, Z.; Yasumura, S.; Wu, X.; Huang, M.; Liu, C.; Toyao, T.; Shimizu, K.-I. Isolated Indium Hydrides in CHA Zeolites: Speciation and Catalysis for Nonoxidative Dehydrogenation of Ethane. *J. Am. Chem. Soc.* **2020,** *142* (10), 4820–4832.
70. Zhao, P.; Ye, L.; Sun, Z.; Lo, B. T. W.; Woodcock, H.; Huang, C.; Tang, C.; Kirkland, A. I.; Mei, D.; Edman Tsang, S. C. Entrapped Single Tungstate Site in Zeolite for Cooperative Catalysis of Olefin Metathesis with Brønsted Acid Site. *J. Am. Chem. Soc.* **2018,** *140* (21), 6661–6667.
71. Yang, M.; Liu, J.; Lee, S.; Zugic, B.; Huang, J.; Allard, L. F.; Flytzani-Stephanopoulos, M. A Common Single-Site Pt(II)–O(OH)x–Species Stabilized by Sodium on "Active" and "Inert" Supports Catalyzes the Water-Gas Shift Reaction. *J. Am. Chem. Soc.* **2015,** *137* (10), 3470–3473.
72. Yang, M.; Li, S.; Wang, Y.; Herron, J. A.; Xu, Y.; Allard, L. F.; Lee, S.; Huang, J.; Mavrikakis, M.; Flytzani-Stephanopoulos, M. Catalytically Active Au-$O(OH)_x$-Species Stabilized by Alkali Ions on Zeolites and Mesoporous Oxides. *Science* **2014,** *346* (6216), 1498–1501.
73. Zhai, Y.; Pierre, D.; Si, R.; Deng, W.; Ferrin, P.; Nilekar, A. U.; Peng, G.; Herron, J. A.; Bell, D. C.; Saltsburg, H.; Mavrikakis, M.; Flytzani-Stephanopoulos, M. Alkali-Stabilized Pt-OH_x Species Catalyze Low-Temperature Water-Gas Shift Reactions. *Science* **2010,** *329* (5999), 1633–1636.
74. Zugic, B.; Zhang, S.; Bell, D. C.; Tao, F.; Flytzani-Stephanopoulos, M. Probing the Low-Temperature Water–Gas Shift Activity of Alkali-Promoted Platinum Catalysts Stabilized on Carbon Supports. *J. Am. Chem. Soc.* **2014,** *136* (8), 3238–3245.
75. Liu, Y.; Li, Z.; Yu, Q.; Chen, Y.; Chai, Z.; Zhao, G.; Liu, S.; Cheong, W.-C.; Pan, Y.; Zhang, Q.; Gu, L.; Zheng, L.; Wang, Y.; Lu, Y.; Wang, D.; Chen, C.; Peng, Q.; Liu, Y.; Liu, L.; Chen, J.; Li, Y. A General Strategy for Fabricating Isolated Single Metal Atomic Site Catalysts in Y Zeolite. *J. Am. Chem. Soc.* **2019,** *141* (23), 9305–9311.
76. Sun, Q.; Wang, N.; Zhang, T.; Bai, R.; Mayoral, A.; Zhang, P.; Zhang, Q.; Terasaki, O.; Yu, J. Zeolite-Encaged Single-Atom Rhodium Catalysts: Highly-Efficient Hydrogen Generation and Shape-Selective Tandem Hydrogenation of Nitroarenes. *Angew. Chem. Int. Ed.* **2019,** *58* (51), 18570–18576.
77. Qiu, J. Z.; Hu, J. B.; Lan, J. G.; Wang, L. F.; Fu, G. Y.; Xiao, R. J.; Ge, B. H.; Jiang, J. X. Pure Siliceous Zeolite-Supported Ru Single-Atom Active Sites for Ammonia Synthesis. *Chem. Mater.* **2019,** *31* (22), 9413–9421.
78. Juneau, M.; Liu, R.; Peng, Y.; Malge, A.; Ma, Z.; Porosoff, M. D. Characterization of Metal-Zeolite Composite Catalysts: Determining the Environment of the Active Phase. *ChemCatChem* **2020,** *12* (7), 1826–1852.
79. Ortalan, V.; Uzun, A.; Gates, B. C.; Browning, N. D. Direct Imaging of Single Metal Atoms and Clusters in the Pores of Dealuminated HY Zeolite. *Nat. Nanotechnol.* **2010,** *5* (7), 506–510.
80. Browning, N. D.; Aydin, C.; Lu, J.; Kulkarni, A.; Okamoto, N. L.; Ortalan, V.; Reed, B. W.; Uzun, A.; Gates, B. C. Quantitative Z-Contrast Imaging of Supported Metal Complexes and ClustersA Gateway to Understanding Catalysis on the Atomic Scale. *ChemCatChem* **2013,** *5* (9), 2673–2683.
81. Xu, P.; Lu, J.; Aydin, C.; Debefve, L. M.; Browning, N. D.; Chen, C.-Y.; Gates, B. C. Imaging Individual Lanthanum Atoms in Zeolite Y by Scanning Transmission Electron Microscopy: Evidence of Lanthanum Pair Sites. *Microporous Mesoporous Mater.* **2015,** *213,* 95–99.
82. Aydin, C.; Lu, J.; Shirai, M.; Browning, N. D.; Gates, B. C. Ir-6 Clusters Compartmentalized in the Supercages of Zeolite NaY: Direct Imaging of a Catalyst with Aberration-Corrected Scanning Transmission Electron Microscopy. *ACS Catal.* **2011,** *1* (11), 1613–1620.
83. Aydin, C.; Lu, J.; Liang, A. J.; Chen, C. Y.; Browning, N. D.; Gates, B. C. Tracking Iridium Atoms with Electron Microscopy: First Steps of Metal Nanocluster Formation in One-Dimensional Zeolite Channels. *Nano Lett.* **2011,** *11* (12), 5537–5541.
84. Schüßler, F.; Pidko, E. A.; Kolvenbach, R.; Sievers, C.; Hensen, E. J. M.; van Santen, R. A.; Lercher, J. A. Nature and Location of Cationic Lanthanum Species in High Alumina Containing Faujasite Type Zeolites. *J. Phys. Chem. C* **2011,** *115* (44), 21763–21776.
85. Mayoral, A.; Readman, J. E.; Anderson, P. A. Aberration-Corrected STEM Analysis of a Cubic Cd Array Encapsulated in Zeolite A. *J. Phys. Chem. C* **2013,** *117* (46), 24485–24489.
86. Mayoral, A.; Carey, T.; Anderson, P. A.; Diaz, I. Atomic Resolution Analysis of Porous Solids: A Detailed Study of Silver Ion-Exchanged Zeolite A. *Microporous Mesoporous Mater.* **2013,** *166,* 117–122.
87. Mayoral, A.; Carey, T.; Anderson, P. A.; Lubk, A.; Diaz, I. Atomic Resolution Analysis of Silver Ion-Exchanged Zeolite A. *Angew. Chem. Int. Ed.* **2011,** *50* (47), 11230–11233.

88. Filippousi, M.; Turner, S.; Katsikini, M.; Pinakidou, F.; Zamboulis, D.; Pavlidou, E.; Van Tendeloo, G. Direct Observation and Structural Characterization of Natural and Metal Ion-Exchanged HEU-Type Zeolites. *Microporous Mesoporous Mater.* **2015,** *210,* 185–193.
89. Altantzis, T.; Coutino-Gonzalez, E.; Baekelant, W.; Martinez, G. T.; Abakumov, A. M.; Van Tendeloo, G.; Roeffaers, M. B. J.; Bals, S.; Hofkens, J. Direct Observation of Luminescent Silver Clusters Confined in Faujasite Zeolites. *ACS Nano* **2016,** *10* (8), 7604–7611.
90. Mayoral, A.; Hall, R. M.; Jackowska, R.; Readman, J. E. Imaging the Atomic Position of Light Cations in a Porous Network and the Europium(III) Ion Exchange Capability by Aberration-Corrected Electron Microscopy. *Angew. Chem. Int. Ed.* **2016,** *55* (52), 16127–16131.
91. Mayoral, A.; Zhang, Q.; Zhou, Y.; Chen, P.; Ma, Y.; Monji, T.; Losch, P.; Schmidt, W.; Schüth, F.; Hirao, H.; Yu, J.; Terasaki, O. Direct Atomic-Level Imaging of Zeolites: Oxygen, Sodium in Na-LTA and Iron in Fe-MFI. *Angew. Chem. Int. Ed.* **2020,** *59* (44), 19510–19517.
92. Liu, L.; Lopez-Haro, M.; Calvino, J. J.; Corma, A. Tutorial: Structural Characterization of Isolated Metal Atoms and Subnanometric Metal Clusters in Zeolites. *Nat. Protoc.* **2020,** *16* (4), 1871–1906.
93. Liu, L. M.; Wang, N.; Zhu, C. Z.; Liu, X. N.; Zhu, Y. H.; Guo, P.; Alfilfil, L.; Dong, X. L.; Zhang, D. L.; Han, Y. Direct Imaging of Atomically Dispersed Molybdenum that Enables Location of Aluminum in the Framework of Zeolite ZSM-5. *Angew. Chem. Int. Ed.* **2020,** *59* (2), 819–825.
94. Shen, B. Y.; Chen, X.; Cai, D. L.; Xiong, H.; Liu, X.; Meng, C. G.; Han, Y.; Wei, F. Atomic Spatial and Temporal Imaging of Local Structures and Light Elements Inside Zeolite Frameworks. *Adv. Mater.* **2019,** *32* (4), 1906103.
95. Fodor, D.; Ishikawa, T.; Krumeich, F.; van Bokhoven, J. A. Synthesis of Single Crystal Nanoreactor Materials with Multiple Catalytic Functions by Incipient Wetness Impregnation and Ion Exchange. *Adv. Mater.* **2015,** *27* (11), 1919–1923.
96. Friedrich, H.; de Jongh, P. E.; Verkleij, A. J.; de Jong, K. P. Electron Tomography for Heterogeneous Catalysts and Related Nanostructured Materials. *Chem. Rev.* **2009,** *109* (5), 1613–1629.
97. Sushkevich, V. L.; Palagin, D.; Ranocchiari, M.; van Bokhoven, J. A. Selective Anaerobic Oxidation of Methane Enables Direct Synthesis of Methanol. *Science* **2017,** *356* (6337), 523–527.
98. Paolucci, C.; Khurana, I.; Parekh, A. A.; Li, S.; Shih, A. J.; Li, H.; Di Iorio, J. R.; Albarracin-Caballero, J. D.; Yezerets, A.; Miller, J. T.; Delgass, W. N.; Ribeiro, F. H.; Schneider, W. F.; Gounder, R. Dynamic Multinuclear Sites Formed by Mobilized Copper Ions in NO_x Selective Catalytic Reduction. *Science* **2017,** *357* (6354), 898–903.
99. Kerkeni, B.; Berthout, D.; Berthomieu, D.; Doronkin, D. E.; Casapu, M.; Grunwaldt, J. D.; Chizallet, C. Copper Coordination to Water and Ammonia in CuII-Exchanged SSZ-13: Atomistic Insights from DFT Calculations and In Situ XAS Experiments. *J. Phys. Chem. C* **2018,** *122* (29), 16741–16755.
100. Negri, C.; Selleri, T.; Borfecchia, E.; Martini, A.; Lomachenko, K. A.; Janssens, T. V. W.; Cutini, M.; Bordiga, S.; Berlier, G. Structure and Reactivity of Oxygen-Bridged Diamino Dicopper(II) Complexes in Cu-Ion-Exchanged Chabazite Catalyst for NH_3-Mediated Selective Catalytic Reduction. *J. Am. Chem. Soc.* **2020,** *142* (37), 15884–15896.
101. Becher, J.; Sanchez, D. F.; Doronkin, D. E.; Zengel, D.; Meira, D. M.; Pascarelli, S.; Grunwaldt, J.-D.; Sheppard, T. L. Chemical Gradients in Automotive Cu-SSZ-13 Catalysts for NOx Removal Revealed by Operando X-Ray Spectrotomography. *Nat. Catal.* **2021,** *4* (1), 46–53.
102. Borfecchia, E.; Beato, P.; Svelle, S.; Olsbye, U.; Lamberti, C.; Bordiga, S. Cu-CHA—A Model System for Applied Selective Redox Catalysis. *Chem. Soc. Rev.* **2018,** *47* (22), 8097–8133.
103. Shan, Y.; Du, J.; Zhang, Y.; Shan, W.; Shi, X.; Yu, Y.; Zhang, R.; Meng, X.; Xiao, F.-S.; He, H. Selective Catalytic Reduction of NOx with NH_3: Opportunities and Challenges of Cu-Based Small-Pore Zeolites. *Natl. Sci. Rev.* **2021;**, nwab010.
104. Paolucci, C.; Di Iorio, J. R.; Schneider, W. F.; Gounder, R. Solvation and Mobilization of Copper Active Sites in Zeolites by Ammonia: Consequences for the Catalytic Reduction of Nitrogen Oxides. *Acc. Chem. Res.* **2020,** *53* (9), 1881–1892.
105. Pidko, E. A.; Hensen, E. J. M.; van Santen, R. A. Self-Organization of Extraframework Cations in Zeolites. *Proc. R. Soc. A Math. Phys. Eng. Sci.* **2012,** *468* (2143), 2070–2086.
106. Dinh, K. T.; Sullivan, M. M.; Narsimhan, K.; Serna, P.; Meyer, R. J.; Dincă, M.; Román-Leshkov, Y. Continuous Partial Oxidation of Methane to Methanol Catalyzed by Diffusion-Paired Copper Dimers in Copper-Exchanged Zeolites. *J. Am. Chem. Soc.* **2019,** *141* (29), 11641–11650.
107. Song, J.; Wang, Y.; Walter, E. D.; Washton, N. M.; Mei, D.; Kovarik, L.; Engelhard, M. H.; Prodinger, S.; Wang, Y.; Peden, C. H. F.; Gao, F. Toward Rational Design of Cu/SSZ-13 Selective Catalytic Reduction Catalysts: Implications from Atomic-Level Understanding of Hydrothermal Stability. *ACS Catal.* **2017,** *7* (12), 8214–8227.
108. Kiani, D.; Sourav, S.; Tang, Y.; Baltrusaitis, J.; Wachs, I. E. Methane Activation by ZSM-5-Supported Transition Metal Centers. *Chem. Soc. Rev.* **2021,** *50* (2), 1251–1268.
109. Kosinov, N.; Hensen, E. J. M. Reactivity, Selectivity, and Stability of Zeolite-Based Catalysts for Methane Dehydroaromatization. *Adv. Mater.* **2020,** *32* (44), 2002565.
110. Lezcano-González, I.; Oord, R.; Rovezzi, M.; Glatzel, P.; Botchway, S. W.; Weckhuysen, B. M.; Beale, A. M. Molybdenum Speciation and Its Impact on Catalytic Activity During Methane Dehydroaromatization in Zeolite ZSM-5 as Revealed by Operando X-Ray Methods. *Angew. Chem. Int. Ed.* **2016,** *55* (17), 5215–5219.
111. Vollmer, I.; Yarulina, I.; Kapteijn, F.; Gascon, J. Progress in Developing a Structure-Activity Relationship for the Direct Aromatization of Methane. *ChemCatChem* **2019,** *11* (1), 39–52.
112. Agote-Arán, M.; Kroner, A. B.; Islam, H. U.; Sławiński, W. A.; Wragg, D. S.; Lezcano-González, I.; Beale, A. M. Determination of Molybdenum Species Evolution During Non-Oxidative Dehydroaromatization of Methane and Its Implications for Catalytic Performance. *ChemCatChem* **2019,** *11* (1), 473–480.
113. Kosinov, N.; Coumans, F.; Uslamin, E.; Kapteijn, F.; Hensen, E. J. M. Selective Coke Combustion by Oxygen Pulsing During Mo/ZSM-5-Catalyzed Methane Dehydroaromatization. *Angew. Chem. Int. Ed.* **2016,** *55* (48), 15086–15090.
114. Kosinov, N.; Coumans, F.; Li, G.; Uslamin, E.; Mezari, B.; Wijpkema, A. S. G.; Pidko, E. A.; Hensen, E. J. M. Stable Mo/HZSM-5 Methane Dehydroaromatization Catalysts Optimized for High-Temperature Calcination-Regeneration. *J. Catal.* **2017,** *346,* 125–133.
115. Kosinov, N.; Coumans, F. J. A. G.; Uslamin, E. A.; Wijpkema, A. S. G.; Mezari, B.; Hensen, E. J. M. Methane Dehydroaromatization by Mo/HZSM-5: Mono- or Bifunctional Catalysis? *ACS Catal.* **2017,** *7* (1), 520–529.
116. Kosinov, N.; Wijpkema, A. S. G.; Uslamin, E.; Rohling, R.; Coumans, F. J. A. G.; Mezari, B.; Parastaev, A.; Poryvaev, A. S.; Fedin, M. V.; Pidko, E. A.; Hensen, E. J. M. Confined Carbon Mediating Dehydroaromatization of Methane over Mo/ZSM-5. *Angew. Chem. Int. Ed.* **2018,** *57* (4), 1016–1020.
117. Kosinov, N.; Uslamin, E. A.; Meng, L.; Parastaev, A.; Liu, Y.; Hensen, E. J. M. Reversible Nature of Coke Formation on Mo/ZSM-5 Methane Dehydroaromatization Catalysts. *Angew. Chem. Int. Ed.* **2019,** *58* (21), 7068–7072.
118. Agote-Arán, M.; Kroner, A. B.; Wragg, D. S.; Sławiński, W. A.; Briceno, M.; Islam, H. U.; Sazanovich, I. V.; Rivas, M. E.; Smith, A. W. J.; Collier, P.; Lezcano-González, I.; Beale, A. M. Understanding the Deactivation Phenomena of Small-Pore Mo/H-SSZ-13 During Methane Dehydroaromatisation. *Molecules* **2020,** *25* (21), 5048.
119. Vollmer, I.; van der Linden, B.; Ould-Chikh, S.; Aguilar-Tapia, A.; Yarulina, I.; Abou-Hamad, E.; Sneider, Y. G.; Olivos Suarez, A. I.; Hazemann, J.-L.; Kapteijn, F.; Gascon, J. On the Dynamic Nature of Mo Sites for Methane Dehydroaromatization. *Chem. Sci.* **2018,** *9* (21), 4801–4807.
120. Moliner, M.; Gabay, J. E.; Kliewer, C. E.; Carr, R. T.; Guzman, J.; Casty, G. L.; Serna, P.; Corma, A. Reversible Transformation of Pt Nanoparticles into Single Atoms Inside High-Silica Chabazite Zeolite. *J. Am. Chem. Soc.* **2016,** *138* (48), 15743–15750.
121. Liu, L.; Zakharov, D. N.; Arenal, R.; Concepcion, P.; Stach, E. A.; Corma, A. Evolution and Stabilization of Subnanometric Metal Species in Confined Space by In Situ TEM. *Nat. Commun.* **2018,** *9,* 574.
122. Eremin, D. B.; Ananikov, V. P. Understanding Active Species in Catalytic Transformations: From Molecular Catalysis to Nanoparticles, Leaching, "Cocktails" of Catalysts and Dynamic Systems. *Coord. Chem. Rev.* **2017,** *346,* 2–19.
123. Bordiga, S.; Lamberti, C.; Bonino, F.; Travert, A.; Thibault-Starzyk, F. Probing Zeolites by Vibrational Spectroscopies. *Chem. Soc. Rev.* **2015,** *44* (20), 7262–7341.
124. Woertink, J. S.; Smeets, P. J.; Groothaert, M. H.; Vance, M. A.; Sels, B. F.; Schoonheydt, R. A.; Solomon, E. I. A $[Cu_2O]^{2+}$ Core in Cu-ZSM-5, the Active Site in the Oxidation of Methane to Methanol. *Proc. Natl. Acad. Sci. U. S. A.* **2009,** *106* (45), 18908–18913.
125. Groothaert, M. H.; Smeets, P. J.; Sels, B. F.; Jacobs, P. A.; Schoonheydt, R. A. Selective Oxidation of Methane by the Bis(mu-Oxo)Dicopper Core Stabilized on ZSM-5 and Mordenite Zeolites. *J. Am. Chem. Soc.* **2005,** *127* (5), 1394–1395.

126. Vanelderen, P.; Snyder, B. E. R.; Tsai, M.-L.; Hadt, R. G.; Vancauwenbergh, J.; Coussens, O.; Schoonheydt, R. A.; Sels, B. F.; Solomon, E. I. Spectroscopic Definition of the Copper Active Sites in Mordenite: Selective Methane Oxidation. *J. Am. Chem. Soc.* **2015,** *137* (19), 6383–6392.
127. Snyder, B. E. R.; Vanelderen, P.; Schoonheydt, R. A.; Sels, B. F.; Solomon, E. I. Second-Sphere Effects on Methane Hydroxylation in Cu-Zeolites. *J. Am. Chem. Soc.* **2018,** *140* (29), 9236–9243.
128. Smeets, P. J.; Hadt, R. G.; Woertink, J. S.; Vanelderen, P.; Schoonheydt, R. A.; Sels, B. F.; Solomon, E. I. Oxygen Precursor to the Reactive Intermediate in Methanol Synthesis by Cu-ZSM-5. *J. Am. Chem. Soc.* **2010,** *132* (42), 14736–14738.
129. Pappas, D. K.; Borfecchia, E.; Dyballa, M.; Pankin, I. A.; Lomachenko, K. A.; Martini, A.; Signorile, M.; Teketel, S.; Arstad, B.; Berlier, G.; Lamberti, C.; Bordiga, S.; Olsbye, U.; Lillerud, K. P.; Svelle, S.; Beato, P. Methane to Methanol: Structure Activity Relationships for Cu-CHA. *J. Am. Chem. Soc.* **2017,** *139* (42), 14961–14975.
130. Ipek, B.; Wulfers, M. J.; Kim, H.; Göltl, F.; Hermans, I.; Smith, J. P.; Booksh, K. S.; Brown, C. M.; Lobo, R. F. Formation of $[Cu_2O_2]^{2+}$ and $[Cu_2O]^{2+}$ toward C–H Bond Activation in Cu-SSZ-13 and Cu-SSZ-39. *ACS Catal.* **2017,** *7* (7), 4291–4303.
131. Gao, J.; Zheng, Y. T.; Tang, Y. D.; Jehng, J. M.; Grybos, R.; Handzlik, J.; Wachs, I. E.; Podkolzin, S. G. Spectroscopic and Computational Study of Cr Oxide Structures and Their Anchoring Sites on ZSM-5 Zeolites. *ACS Catal.* **2015,** *5* (5), 3078–3092.
132. Gao, J.; Zheng, Y. T.; Jehng, J. M.; Tang, Y. D.; Wachs, I. E.; Podkolzin, S. G. Identification of Molybdenum Oxide Nanostructures on Zeolites for Natural Gas Conversion. *Science* **2015,** *348* (6235), 686–690.
133. Göltl, F.; Conrad, S.; Wolf, P.; Müller, P.; Love, A. M.; Burt, S. P.; Wheeler, J. N.; Hamers, R. J.; Hummer, K.; Kresse, G.; Mavrikakis, M.; Hermans, I. UV–Vis and Photoluminescence Spectroscopy to Understand the Coordination of Cu Cations in the Zeolite SSZ-13. *Chem. Mater.* **2019,** *31* (23), 9582–9592.
134. Li, H.; Paolucci, C.; Khurana, I.; Wilcox, L. N.; Göltl, F.; Albarracin-Caballero, J. D.; Shih, A. J.; Ribeiro, F. H.; Gounder, R.; Schneider, W. F. Consequences of Exchange-Site Heterogeneity and Dynamics on the UV-Visible Spectrum of Cu-Exchanged SSZ-13. *Chem. Sci.* **2019,** *10* (8), 2373–2384.
135. Vimont, A.; Thibault-Starzyk, F.; Daturi, M. Analysing and Understanding the Active Site by IR Spectroscopy. *Chem. Soc. Rev.* **2010,** *39* (12), 4928–4950.
136. Khivantsev, K.; Jaegers, N. R.; Kovarik, L.; Hanson, J. C.; Tao, F.; Tang, Y.; Zhang, X.; Koleva, I. Z.; Aleksandrov, H. A.; Vayssilov, G. N.; Wang, Y.; Gao, F.; Szanyi, J. Achieving Atomic Dispersion of Highly Loaded Transition Metals in Small-Pore Zeolite SSZ-13: High-Capacity and High-Efficiency Low-Temperature CO and Passive NOx Adsorbers. *Angew. Chem. Int. Ed.* **2018,** *57* (51), 16672–16677.
137. Kwak, J. H.; Varga, T.; Peden, C. H. F.; Gao, F.; Hanson, J. C.; Szanyi, J. Following the Movement of Cu Ions in a SSZ-13 Zeolite during Dehydration, Reduction and Adsorption: A Combined In Situ TP-XRD, XANES/DRIFTS Study. *J. Catal.* **2014,** *314,* 83–93.
138. Zaera, F. New Advances in the Use of Infrared Absorption Spectroscopy for the Characterization of Heterogeneous Catalytic Reactions. *Chem. Soc. Rev.* **2014,** *43* (22), 7624–7663.
139. Xu, J.; Wang, Q.; Deng, F. Metal Active Sites and Their Catalytic Functions in Zeolites: Insights from Solid-State NMR Spectroscopy. *Acc. Chem. Res.* **2019,** *52* (8), 2179–2189.
140. Li, S.; Lafon, O.; Wang, W.; Wang, Q.; Wang, X.; Li, Y.; Xu, J.; Deng, F. Recent Advances of Solid-State NMR Spectroscopy for Microporous Materials. *Adv. Mater.* **2020,** *32* (44), 2002879.
141. Yu, Z.; Zheng, A.; Wang, Q.; Chen, L.; Xu, J.; Amoureux, J.-P.; Deng, F. Insights into the Dealumination of Zeolite HY Revealed by Sensitivity-Enhanced 27Al DQ-MAS NMR Spectroscopy at High Field. *Angew. Chem. Int. Ed.* **2010,** *49* (46), 8657–8661.
142. Wang, X.; Qi, G.; Xu, J.; Li, B.; Wang, C.; Deng, F. NMR-Spectroscopic Evidence of Intermediate-Dependent Pathways for Acetic Acid Formation from Methane and Carbon Monoxide over a ZnZSM-5 Zeolite Catalyst. *Angew. Chem. Int. Ed.* **2012,** *51* (16), 3850–3853.
143. Wu, J.-F.; Yu, S.-M.; Wang, W. D.; Fan, Y.-X.; Bai, S.; Zhang, C.-W.; Gao, Q.; Huang, J.; Wang, W. Mechanistic Insight into the Formation of Acetic Acid from the Direct Conversion of Methane and Carbon Dioxide on Zinc-Modified H–ZSM-5 Zeolite. *J. Am. Chem. Soc.* **2013,** *135* (36), 13567–13573.
144. Wu, X.; Xu, S.; Zhang, W.; Huang, J.; Li, J.; Yu, B.; Wei, Y.; Liu, Z. Direct Mechanism of the First Carbon–Carbon Bond Formation in the Methanol-to-Hydrocarbons Process. *Angew. Chem. Int. Ed.* **2017,** *56* (31), 9039–9043.
145. Zhao, Z.; Shi, H.; Wan, C.; Hu, M. Y.; Liu, Y.; Mei, D.; Camaioni, D. M.; Hu, J. Z.; Lercher, J. A. Mechanism of Phenol Alkylation in Zeolite H-BEA Using In Situ Solid-State NMR Spectroscopy. *J. Am. Chem. Soc.* **2017,** *139* (27), 9178–9185.
146. Jaegers, N. R.; Mueller, K. T.; Wang, Y.; Hu, J. Z. Variable Temperature and Pressure Operando MAS NMR for Catalysis Science and Related Materials. *Acc. Chem. Res.* **2020,** *53* (3), 611–619.
147. Zheng, H.; Ma, D.; Bao, X.; Hu, J. Z.; Kwak, J. H.; Wang, Y.; Peden, C. H. F. Direct Observation of the Active Center for Methane Dehydroaromatization Using an Ultrahigh Field 95Mo NMR Spectroscopy. *J. Am. Chem. Soc.* **2008,** *130* (12), 3722–3723.
148. Hu, J. Z.; Kwak, J. H.; Wang, Y.; Peden, C. H. F.; Zheng, H.; Ma, D.; Bao, X. Studies of the Active Sites for Methane Dehydroaromatization Using Ultrahigh-Field Solid-State ^{95}Mo NMR Spectroscopy. *J. Phys. Chem. C* **2009,** *113* (7), 2936–2942.
149. Qi, G.; Wang, Q.; Xu, J.; Trébosc, J.; Lafon, O.; Wang, C.; Amoureux, J.-P.; Deng, F. Synergic Effect of Active Sites in Zinc-Modified ZSM-5 Zeolites as Revealed by High-Field Solid-State NMR Spectroscopy. *Angew. Chem. Int. Ed.* **2016,** *55* (51), 15826–15830.
150. Gao, P.; Wang, Q.; Xu, J.; Qi, G.; Wang, C.; Zhou, X.; Zhao, X.; Feng, N.; Liu, X.; Deng, F. Brønsted/Lewis Acid Synergy in Methanol-to-Aromatics Conversion on Ga-Modified ZSM-5 Zeolites, as Studied by Solid-State NMR Spectroscopy. *ACS Catal.* **2018,** *8* (1), 69–74.
151. Zhao, X.; Chu, Y.; Qi, G.; Wang, Q.; Gao, W.; Wang, X.; Li, S.; Xu, J.; Deng, F. Probing the Active Sites for Methane Activation on Ga/ZSM-5 Zeolites with Solid-State NMR Spectroscopy. *Chem. Commun.* **2020,** *56* (80), 12029–12032.
152. Cai, Y.; Kumar, R.; Huang, W.; Trewyn, B. G.; Wiench, J. W.; Pruski, M.; Lin, V. S. Y. Mesoporous Aluminum Silicate Catalyst with Single-Type Active Sites: Characterization by Solid-State NMR and Studies of Reactivity for Claisen Rearrangement Reactions. *J. Phys. Chem. C* **2007,** *111* (3), 1480–1486.
153. Sklenak, S.; Dědeček, J.; Li, C.; Wichterlová, B.; Gábová, V.; Sierka, M.; Sauer, J. Aluminum Siting in Silicon-Rich Zeolite Frameworks: A Combined High-Resolution ^{27}Al NMR Spectroscopy and Quantum Mechanics/Molecular Mechanics Study of ZSM-5. *Angew. Chem. Int. Ed.* **2007,** *46* (38), 7286–7289.
154. Brown, S. P.; Spiess, H. W. Advanced Solid-State NMR Methods for the Elucidation of Structure and Dynamics of Molecular, Macromolecular, and Supramolecular Systems. *Chem. Rev.* **2001,** *101* (12), 4125–4156.
155. Yi, X.; Liu, K.; Chen, W.; Li, J.; Xu, S.; Li, C.; Xiao, Y.; Liu, H.; Guo, X.; Liu, S.-B.; Zheng, A. Origin and Structural Characteristics of Tri-coordinated Extra-framework Aluminum Species in Dealuminated Zeolites. *J. Am. Chem. Soc.* **2018,** *140* (34), 10764–10774.
156. Wang, Z.; O'Dell, L. A.; Zeng, X.; Liu, C.; Zhao, S.; Zhang, W.; Gaborieau, M.; Jiang, Y.; Huang, J. Insight into Three-Coordinate Aluminum Species on Ethanol-to-Olefin Conversion over ZSM-5 Zeolites. *Angew. Chem. Int. Ed.* **2019,** *58* (50), 18061–18068.
157. Malicki, N.; Mali, G.; Quoineaud, A.-A.; Bourges, P.; Simon, L. J.; Thibault-Starzyk, F.; Fernandez, C. Aluminium Triplets in Dealuminated Zeolites Detected by ^{27}Al NMR Correlation Spectroscopy. *Microporous Mesoporous Mater.* **2010,** *129* (1), 100–105.
158. Popovych, N.; Kyriienko, P.; Soloviev, S.; Baran, R.; Millot, Y.; Dzwigaj, S. Identification of the Silver State in the Framework of Ag-Containing Zeolite by XRD, FTIR, Photoluminescence, ^{109}Ag NMR, EPR, DR UV-Vis, TEM and XPS Investigations. *Phys. Chem. Chem. Phys.* **2016,** *18* (42), 29458–29465.
159. Cruz, P.; Fajardo, M.; del Hierro, I.; Pérez, Y. Selective Oxidation of Thioanisole by Titanium Complexes Immobilized on Mesoporous Silica Nanoparticles: Elucidating the Environment of Titanium(iv) Species. *Cat. Sci. Technol.* **2019,** *9* (3), 620–633.
160. Gordon, C. P.; Engler, H.; Tragl, A. S.; Plodinec, M.; Lunkenbein, T.; Berkessel, A.; Teles, J. H.; Parvulescu, A.-N.; Copéret, C. Efficient Epoxidation over Dinuclear Sites in Titanium Silicalite-1. *Nature* **2020,** *586* (7831), 708–713.
161. Pei, S.; Zajac, G. W.; Kaduk, J. A.; Faber, J.; Boyanov, B. I.; Duck, D.; Fazzini, D.; Morrison, T. I.; Yang, D. S. Re-investigation of Titanium Silicalite by X-Ray Absorption Spectroscopy: Are the Novel Titanium Sites Real? *Catal. Lett.* **1993,** *21* (3), 333–344.
162. Weckhuysen, B. M. Fresh Evidence Challenges the Consensus View of Active Sites in an Industrial Catalyst. *Nature* **2020,** *586* (7831), 678–679.

163. Peng, B.; Yao, Y.; Zhao, C.; Lercher, J. A. Towards Quantitative Conversion of Microalgae Oil to Diesel-Range Alkanes with Bifunctional Catalysts. *Angew. Chem. Int. Ed.* **2012,** *51* (9), 2072–2075.
164. Kim, J.; Kim, W.; Seo, Y.; Kim, J.-C.; Ryoo, R. n-Heptane Hydroisomerization over Pt/MFI Zeolite Nanosheets: Effects of Zeolite Crystal Thickness and Platinum Location. *J. Catal.* **2013,** *301,* 187–197.
165. Zhang, Q.; Yu, J.; Corma, A. Applications of Zeolites to C1 Chemistry: Recent Advances, Challenges, and Opportunities. *Adv. Mater.* **2020,** *32* (44), 2002927.
166. Jovanovic, Z. R.; Lange, J.-P.; Ravi, M.; Knorpp, A. J.; Sushkevich, V. L.; Newton, M. A.; Palagin, D.; van Bokhoven, J. A. Oxidation of Methane to Methanol over Cu-Exchanged Zeolites: Scientia Gratia Scientiae or Paradigm Shift in Natural Gas Valorization? *J. Catal.* **2020,** *385,* 238–245.
167. Burnett, L.; Rysakova, M.; Wang, K.; González-Carballo, J.; Tooze, R. P.; García-García, F. R. Isothermal Cyclic Conversion of Methane to Methanol Using Copper-Exchanged ZSM-5 Zeolite Materials under Mild Conditions. *Appl. Catal. A* **2019,** *587,* 117272.
168. Zhao, G.; Benhelal, E.; Adesina, A.; Kennedy, E.; Stockenhuber, M. Comparison of Direct, Selective Oxidation of Methane by N_2O over Fe-ZSM-5, Fe-Beta, and Fe-FER Catalysts. *J. Phys. Chem. C* **2019,** *123* (45), 27436–27447.
169. Newton, M. A.; Knorpp, A. J.; Sushkevich, V. L.; Palagin, D.; van Bokhoven, J. A. Active Sites and Mechanisms in the Direct Conversion of Methane to Methanol Using Cu in Zeolitic Hosts: A Critical Examination. *Chem. Soc. Rev.* **2020,** *49* (5), 1449–1486.
170. Grundner, S.; Markovits, M. A. C.; Li, G.; Tromp, M.; Pidko, E. A.; Hensen, E. J. M.; Jentys, A.; Sanchez-Sanchez, M.; Lercher, J. A. Single-Site Trinuclear Copper Oxygen Clusters in Mordenite for Selective Conversion of Methane to Methanol. *Nat. Commun.* **2015,** *6,* 7546.
171. Sushkevich, V. L.; van Bokhoven, J. A. Kinetic Study and Effect of Water on Methane Oxidation to Methanol Over Copper-Exchanged Mordenite. *Cat. Sci. Technol.* **2020,** *10* (2), 382–390.
172. Tomkins, P.; Mansouri, A.; Bozbag, S. E.; Krumeich, F.; Park, M. B.; Alayon, E. M. C.; Ranocchiari, M.; van Bokhoven, J. A. Isothermal Cyclic Conversion of Methane into Methanol over Copper-Exchanged Zeolite at Low Temperature. *Angew. Chem. Int. Ed.* **2016,** *55,* 5467–5471.
173. Koishybay, A.; Shantz, D. F. Water Is the Oxygen Source for Methanol Produced in Partial Oxidation of Methane in a Flow Reactor over Cu-SSZ-13. *J. Am. Chem. Soc.* **2020,** *142* (28), 11962–11966.
174. Jin, Z.; Wang, L.; Zuidema, E.; Mondal, K.; Zhang, M.; Zhang, J.; Wang, C.; Meng, X.; Yang, H.; Mesters, C.; Xiao, F.-S. Hydrophobic Zeolite Modification for In Situ Peroxide Formation in Methane Oxidation to Methanol. *Science* **2020,** *367* (6474), 193–197.
175. Martinez Galeano, Y.; Negri, F.; Sergio Moreno, M.; Munera, J.; Cornaglia, L.; Tarditi, A. M. Pt Encapsulated into NaA Zeolite as Catalyst for the WGS Reaction. *Appl. Catal. A* **2019,** *572,* 176–184.
176. Wang, C. T.; Guan, E.; Wang, L.; Chu, X. F.; Wu, Z. Y.; Zhang, J.; Yang, Z. Y.; Jiang, Y. W.; Zhang, L.; Meng, X. J.; Gates, B. C.; Xiao, F. S. Product Selectivity Controlled by Nanoporous Environments in Zeolite Crystals Enveloping Rhodium Nanoparticle Catalysts for CO_2 Hydrogenation. *J. Am. Chem. Soc.* **2019,** *141* (21), 8482–8488.
177. Wang, C.; Zhang, J.; Qin, G.; Wang, L.; Zuidema, E.; Yang, Q.; Dang, S.; Yang, C.; Xiao, J.; Meng, X.; Mesters, C.; Xiao, F.-S. Direct Conversion of Syngas to Ethanol within Zeolite Crystals. *Chem* **2020,** *6* (3), 646–657.
178. Wang, Z.; Kim, K.-D.; Zhou, C.; Chen, M.; Maeda, N.; Liu, Z.; Shi, J.; Baiker, A.; Hunger, M.; Huang, J. Influence of Support Acidity on the Performance of Size-Confined Pt Nanoparticles in the Chemoselective Hydrogenation of Acetophenone. *Cat. Sci. Technol.* **2015,** *5* (5), 2788–2797.
179. Sun, Q.; Wang, N.; Bai, R.; Hui, Y.; Zhang, T.; Do, D. A.; Zhang, P.; Song, L.; Miao, S.; Yu, J. Synergetic Effect of Ultrasmall Metal Clusters and Zeolites Promoting Hydrogen Generation. *Adv. Sci.* **2019,** *6* (10), 1802350.
180. Cho, H. J.; Kim, D.; Li, S.; Su, D.; Ma, D.; Xu, B. Molecular-Level Proximity of Metal and Acid Sites in Zeolite-Encapsulated Pt Nanoparticles for Selective Multistep Tandem Catalysis. *ACS Catal.* **2020,** *10* (5), 3340–3348.
181. Zhang, B.; Tian, Y.; Chen, D.; Li, L.; Li, G.; Wang, L.; Zhang, X.; Liu, G. Selective Steam Reforming of n-Dodecane over Stable Subnanometric NiPt Clusters Encapsulated in Silicalite-1 Zeolite. *AIChE J.* **2020,** *66* (5), e16917.
182. Wang, Y.; Hu, Z.-P.; Lv, X.; Chen, L.; Yuan, Z.-Y. Ultrasmall PtZn Bimetallic Nanoclusters Encapsulated in Silicalite-1 Zeolite with Superior Performance for Propane Dehydrogenation. *J. Catal.* **2020,** *385,* 61–69.
183. Chen, Q.; Wang, M.; Zhang, C.; Ren, K.; Xin, Y.; Zhao, M.; Xing, E. Selectivity Control on Hydrogenation of Substituted Nitroarenes through End-on Adsorption of Reactants in Zeolite-Encapsulated Platinum Nanoparticles. *Chem. Asian J.* **2018,** *13* (16), 2077–2084.
184. Chen, Q.; Kang, H. Z.; Liu, X.; Jiang, K.; Bi, Y. F.; Zhou, Y. M.; Wang, M. Y.; Zhang, M.; Liu, L.; Xing, E. H. Selective Hydrogenation of Aromatic Ketone over Pt@Y Zeolite Through Restricted Adsorption Conformation of Reactants by Zeolitic Micropores. *ChemCatChem* **2020,** *12* (7), 1948–1952.
185. Vercammen, J.; Bocus, M.; Neale, S.; Bugaev, A.; Tomkins, P.; Hajek, J.; Van Minnebruggen, S.; Soldatov, A.; Krajnc, A.; Mali, G.; Van Speybroeck, V.; De Vos, D. Shape-Selective C–H Activation of Aromatics to Biarylic Compounds Using Molecular Palladium in Zeolites. *Nat. Catal.* **2020,** *3* (12), 1002–1009.
186. Chai, Y.; Liu, S.; Zhao, Z.-J.; Gong, J.; Dai, W.; Wu, G.; Guan, N.; Li, L. Selectivity Modulation of Encapsulated Palladium Nanoparticles by Zeolite Microenvironment for Biomass Catalytic Upgrading. *ACS Catal.* **2018,** *8* (9), 8578–8589.
187. Jin, Z.; Wang, L.; Hu, Q.; Zhang, L.; Xu, S.; Dong, X.; Gao, X.; Ma, R.; Meng, X.; Xiao, F.-S. Hydrophobic Zeolite Containing Titania Particles as Wettability-Selective Catalyst for Formaldehyde Removal. *ACS Catal.* **2018,** *8* (6), 5250–5254.
188. Wang, C.; Liu, Z.; Wang, L.; Dong, X.; Zhang, J.; Wang, G.; Han, S.; Meng, X.; Zheng, A.; Xiao, F.-S. Importance of Zeolite Wettability for Selective Hydrogenation of Furfural over Pd@Zeolite Catalysts. *ACS Catal.* **2018,** *8* (1), 474–481.
189. Grajciar, L.; Heard, C. J.; Bondarenko, A. A.; Polynski, M. V.; Meeprasert, J.; Pidko, E. A.; Nachtigall, P. Towards Operando Computational Modeling in Heterogeneous Catalysis. *Chem. Soc. Rev.* **2018,** *47,* 8307–8348.
190. Reuter, K.; Scheffler, M. First-Principles Atomistic Thermodynamics for Oxidation Catalysis: Surface Phase Diagrams and Catalytically Interesting Regions. *Phys. Rev. Lett.* **2003,** *90* (4), 046103.
191. McEwen, J. S.; Anggara, T.; Schneider, W. F.; Kispersky, V. F.; Miller, J. T.; Delgass, W. N.; Ribeiro, F. H. Integrated Operando X-Ray Absorption and DFT Characterization of Cu–SSZ-13 Exchange Sites during the Selective Catalytic Reduction of NOx with NH_3. *Catal. Today* **2012,** *184* (1), 129–144.
192. Li, G.; Pidko, E. A.; van Santen, R. A.; Li, C.; Hensen, E. J. M. Stability of Extraframework Iron-Containing Complexes in ZSM-5 Zeolite. *J. Phys. Chem. C* **2013,** *117* (1), 413–426.
193. Zheng, J.; Lee, I.; Khramenkova, E.; Wang, M.; Peng, B.; Gutiérrez, O. Y.; Fulton, J. L.; Camaioni, D. M.; Khare, R.; Jentys, A.; Haller, G. L.; Pidko, E. A.; Sanchez-Sanchez, M.; Lercher, J. A. Importance of Methane Chemical Potential for Its Conversion to Methanol on Cu-Exchanged Mordenite. *Chem. A Eur. J.* **2020,** *26* (34), 7563–7567.
194. Liu, C.; Li, G.; Hensen, E. J. M.; Pidko, E. A. Nature and Catalytic Role of Extraframework Aluminum in Faujasite Zeolite: A Theoretical Perspective. *ACS Catal.* **2015,** *5* (11), 7024–7033.
195. Li, G.; Vollmer, I.; Liu, C.; Gascon, J.; Pidko, E. A. Structure and Reactivity of the Mo/ZSM-5 Dehydroaromatization Catalyst: An Operando Computational Study. *ACS Catal.* **2019,** *9* (9), 8731–8737.
196. Heiles, S.; Johnston, R. L. Global Optimization of Clusters Using Electronic Structure Methods. *Int. J. Quantum Chem.* **2013,** *113* (18), 2091–2109.
197. Jørgensen, M. S.; Groves, M. N.; Hammer, B. Combining Evolutionary Algorithms with Clustering toward Rational Global Structure Optimization at the Atomic Scale. *J. Chem. Theory Comput.* **2017,** *13* (3), 1486–1493.
198. Zhao, Z.-J.; Liu, S.; Zha, S.; Cheng, D.; Studt, F.; Henkelman, G.; Gong, J. Theory-Guided Design of Catalytic Materials Using Scaling Relationships and Reactivity Descriptors. *Nat. Rev. Mater.* **2019,** *4* (12), 792–804.
199. Brogaard, R. Y.; Wang, C.-M.; Studt, F. Methanol–Alkene Reactions in Zeotype Acid Catalysts: Insights from a Descriptor-Based Approach and Microkinetic Modeling. *ACS Catal.* **2014,** *4* (12), 4504–4509.

200. Wang, C.-M.; Brogaard, R. Y.; Weckhuysen, B. M.; Nørskov, J. K.; Studt, F. Reactivity Descriptor in Solid Acid Catalysis: Predicting Turnover Frequencies for Propene Methylation in Zeotypes. *J. Phys. Chem. Lett.* **2014,** *5* (9), 1516–1521.
201. Wang, C.-M.; Brogaard, R. Y.; Xie, Z.-K.; Studt, F. Transition-State Scaling Relations in Zeolite Catalysis: Influence of Framework Topology and Acid-Site Reactivity. *Cat. Sci. Technol.* **2015,** *5* (5), 2814–2820.
202. Siahrostami, S.; Falsig, H.; Beato, P.; Moses, P. G.; Nørskov, J. K.; Studt, F. Exploring Scaling Relations for Chemisorption Energies on Transition-Metal-Exchanged Zeolites ZSM-22 and ZSM-5. *ChemCatChem* **2016,** *8* (4), 767–772.
203. Bukowski, B. C.; Greeley, J. Scaling Relationships for Molecular Adsorption and Dissociation in Lewis Acid Zeolites. *J. Phys. Chem. C* **2016,** *120* (12), 6714–6722.
204. Latimer, A. A.; Kulkarni, A. R.; Aljama, H.; Montoya, J. H.; Yoo, J. S.; Tsai, C.; Abild-Pedersen, F.; Studt, F.; Nørskov, J. K. Understanding Trends in C–H Bond Activation in Heterogeneous Catalysis. *Nat. Mater.* **2016,** *16,* 225.
205. Xie, P.; Pu, T.; Aranovich, G.; Guo, J.; Donohue, M.; Kulkarni, A.; Wang, C. Bridging Adsorption Analytics and Catalytic Kinetics for Metal-Exchanged Zeolites. *Nat. Catal.* **2021,** *4* (2), 144–156.
206. Göltl, F.; Müller, P.; Uchupalanun, P.; Sautet, P.; Hermans, I. Developing a Descriptor-Based Approach for CO and NO Adsorption Strength to Transition Metal Sites in Zeolites. *Chem. Mater.* **2017,** *29* (15), 6434–6444.
207. Szécsényi, Á.; Khramenkova, E.; Chernyshov, I. Y.; Li, G.; Gascon, J.; Pidko, E. A. Breaking Linear Scaling Relationships with Secondary Interactions in Confined Space: A Case Study of Methane Oxidation by Fe/ZSM-5 Zeolite. *ACS Catal.* **2019,** *9* (10), 9276–9284.
208. Liu, C.; Tranca, I.; van Santen, R. A.; Hensen, E. J. M.; Pidko, E. A. Scaling Relations for Acidity and Reactivity of Zeolites. *J. Phys. Chem. C* **2017,** *121* (42), 23520–23530.
209. Gani, T. Z. H.; Kulik, H. J. Understanding and Breaking Scaling Relations in Single-Site Catalysis: Methane to Methanol Conversion by FeIV═O. *ACS Catal.* **2018,** *8* (2), 975–986.
210. Pérez-Ramírez, J.; López, N. Strategies to Break Linear Scaling Relationships. *Nat. Catal.* **2019,** *2* (11), 971–976.
211. Liu, C.; van Santen, R. A.; Poursaeidesfahani, A.; Vlugt, T. J. H.; Pidko, E. A.; Hensen, E. J. M. Hydride Transfer Versus Deprotonation Kinetics in the Isobutane–Propene Alkylation Reaction: A Computational Study. *ACS Catal.* **2017,** *7* (12), 8613–8627.
212. Sengar, A.; van Santen, R. A.; Kuipers, J. A. M. Deactivation Kinetics of the Catalytic Alkylation Reaction. *ACS Catal.* **2020,** *10* (13), 6988–7006.
213. Martini, A.; Borfecchia, E.; Lomachenko, K. A.; Pankin, I. A.; Negri, C.; Berlier, G.; Beato, P.; Falsig, H.; Bordiga, S.; Lamberti, C. Composition-Driven Cu-Speciation and Reducibility in Cu-CHA Zeolite Catalysts: A Multivariate XAS/FTIR Approach to Complexity. *Chem. Sci.* **2017,** *8* (10), 6836–6851.
214. Mandal, K.; Gu, Y.; Westendorff, K. S.; Li, S.; Pihl, J. A.; Grabow, L. C.; Epling, W. S.; Paolucci, C. Condition-Dependent Pd Speciation and NO Adsorption in Pd/Zeolites. *ACS Catal.* **2020,** *10* (21), 12801–12818.
215. Gounder, R.; Iglesia, E. The Roles of Entropy and Enthalpy in Stabilizing Ion-Pairs at Transition States in Zeolite Acid Catalysis. *Acc. Chem. Res.* **2012,** *45* (2), 229–238.
216. Van der Mynsbrugge, J.; Janda, A.; Mallikarjun Sharada, S.; Lin, L.-C.; Van Speybroeck, V.; Head-Gordon, M.; Bell, A. T. Theoretical Analysis of the Influence of Pore Geometry on Monomolecular Cracking and Dehydrogenation of n-Butane in Brønsted Acidic Zeolites. *ACS Catal.* **2017,** *7* (4), 2685–2697.
217. Jones, A. J.; Iglesia, E. Kinetic, Spectroscopic, and Theoretical Assessment of Associative and Dissociative Methanol Dehydration Routes in Zeolites. *Angew. Chem. Int. Ed.* **2014,** *53* (45), 12177–12181.
218. Janda, A.; Vlaisavljevich, B.; Lin, L.-C.; Smit, B.; Bell, A. T. Effects of Zeolite Structural Confinement on Adsorption Thermodynamics and Reaction Kinetics for Monomolecular Cracking and Dehydrogenation of n-Butane. *J. Am. Chem. Soc.* **2016,** *138* (14), 4739–4756.
219. Shetty, M.; Wang, H.; Chen, F.; Jaegers, N.; Liu, Y.; Camaioni, D. M.; Gutiérrez, O. Y.; Lercher, J. A. Directing the Rate-Enhancement for Hydronium Ion Catalyzed Dehydration Via Organization of Alkanols in Nanoscopic Confinements. *Angew. Chem. Int. Ed.* **2021,** *60* (5), 2304–2311.
220. Kalz, K. F.; Kraehnert, R.; Dvoyashkin, M.; Dittmeyer, R.; Gläser, R.; Krewer, U.; Reuter, K.; Grunwaldt, J.-D. Future Challenges in Heterogeneous Catalysis: Understanding Catalysts under Dynamic Reaction Conditions. *ChemCatChem* **2017,** *9* (1), 17–29.
221. Liu, A.; Liu, L.; Cao, Y.; Wang, J.; Si, R.; Gao, F.; Dong, L. Controlling Dynamic Structural Transformation of Atomically Dispersed CuOx Species and Influence on Their Catalytic Performances. *ACS Catal.* **2019,** *9* (11), 9840–9851.
222. Shamzhy, M.; Opanasenko, M.; Concepcion, P.; Martinez, A. New Trends in Tailoring Active Sites in Zeolite-Based Catalysts. *Chem. Soc. Rev.* **2019,** *48* (4), 1095–1149.
223. Tan, S. F.; Chee, S. W.; Baraissov, Z.; Jin, H.; Tan, T. L.; Mirsaidov, U. Real-Time Imaging of Nanoscale Redox Reactions over Bimetallic Nanoparticles. *Adv. Funct. Mater.* **2019,** *29* (37), 1903242.
224. Kang, J.; Carnis, J.; Kim, D.; Chung, M.; Kim, J.; Yun, K.; An, G.; Cha, W.; Harder, R.; Song, S.; Sikorski, M.; Robert, A.; Thanh, N. H.; Lee, H.; Choi, Y. N.; Huang, X.; Chu, Y. S.; Clark, J. N.; Song, M. K.; Yoon, K. B.; Robinson, I. K.; Kim, H. Time-Resolved In Situ Visualization of the Structural Response of Zeolites During Catalysis. *Nat. Commun.* **2020,** *11* (1), 5901.
225. Collinge, G.; Yuk, S. F.; Nguyen, M.-T.; Lee, M.-S.; Glezakou, V.-A.; Rousseau, R. Effect of Collective Dynamics and Anharmonicity on Entropy in Heterogenous Catalysis: Building the Case for Advanced Molecular Simulations. *ACS Catal.* **2020,** *10* (16), 9236–9260.
226. Moliner, M.; Roman-Leshkov, Y.; Corma, A. Machine Learning Applied to Zeolite Synthesis: The Missing Link for Realizing High-Throughput Discovery. *Acc. Chem. Res.* **2019,** *52* (10), 2971–2980.
227. Ulissi, Z. W.; Medford, A. J.; Bligaard, T.; Nørskov, J. K. To Address Surface Reaction Network Complexity Using Scaling Relations Machine Learning and DFT Calculations. *Nat. Commun.* **2017,** *8* (1), 14621.
228. Back, S.; Yoon, J.; Tian, N.; Zhong, W.; Tran, K.; Ulissi, Z. W. Convolutional Neural Network of Atomic Surface Structures to Predict Binding Energies for High-Throughput Screening of Catalysts. *J. Phys. Chem. Lett.* **2019,** *10* (15), 4401–4408.
229. Goodman, E. D.; Schwalbe, J. A.; Cargnello, M. Mechanistic Understanding and the Rational Design of Sinter-Resistant Heterogeneous Catalysts. *ACS Catal.* **2017,** *7* (10), 7156–7173.
230. Gao, M.; Li, H.; Liu, W.; Xu, Z.; Peng, S.; Yang, M.; Ye, M.; Liu, Z. Imaging Spatiotemporal Evolution of Molecules and Active Sites in Zeolite Catalyst During Methanol-to-Olefins Reaction. *Nat. Commun.* **2020,** *11* (1), 3641.